The Pennsylvania State University
The Graduate School

DEVELOPMENT OF ULTRA LOW FIELD MAGNETIC RESONANCE IMAGING FOR DIAGNOSIS OF HYDROCEPHALUS IN DEVELOPING COUNTRIES

A Dissertation in
Biomedical Engineering
by
Johnes Obungoloch

© 2017 Johnes Obungoloch

Submitted in Partial Fulfillment
of the Requirements
for the Degree of

Doctor of Philosophy

May 2017

The dissertation of Johnes Obungoloch was reviewed and approved* by the following:

Steven J Schiff
Director, Center for Neural Engineering
Brush Chair Professor of Engineering
Professor of Engineering Science and Mechanics, Neurosurgery, Physics and Biomedical Engineering
Dissertation Advisor, Chair of Committee

Igor M Savukov
Scientist, Los Alamos National Laboratory
Special Member

Peter J Buttler
Professor of Biomedical Engineering

Thomas Neuberger
Assistant Professor of Biomedical Engineering

Nanyin Zhang
Associate Professor of Biomedical Engineering

Michael Lanagan
Professor of Engineering Science and Mechanics

Srinivas Tadigadapa
Professor of Electrical Engineering

William Hancock
Professor of Biomedical Engineering
Graduate Program Chair

*Signatures are on file in the Graduate School.

Abstract

Access to Medical imaging technologies and services still remain a challenge in low and middle income countries (LMICs). The most common imaging modalities available are X-ray technologies and ultrasound, none of which is appropriate for imaging the brain. Diagnosis and monitoring of mental and brain illnesses such as epilepsy, hydrocephalus, and trauma rely mainly on computed tomography (CT) even though they are known to have adverse effects [1] especially with repeated exposures as is required in neuro-surgical interventions.

Conventional magnetic resonance imaging (MRI), a relatively safer technology than CT is very expensive for LMICs to afford. The capital costs of installing a 3 T MRI system can be as high as $3 million [2]. On top of the high procurement and installation costs, other requirements such as cryogens and technical expertise have prevented the proliferation of MRI in developing countries. Premised on this background, this thesis explains the development of an ultra-low field MRI suitable for the diagnosis of hydrocephalus in the developing world. Parameters considered for the suitability of this MRI include low cost, low power and technical requirements, portability and flexibility in siting.

To meet the aims of this project, an ultra-low field MRI system capable of admitting an adult head was constructed at a cost of $30,000. This MRI system requires no cryogens, has maximum power requirement of 1.5 kW, weighs 125 kg and can operate in an un-shielded room. Images of vegetables were acquired with the system operated at 113 kHz.

Table of Contents

List of Figures **vii**

List of Symbols **ix**

Acknowledgments **x**

Chapter 1
BACKGROUND AND SIGNIFICANCE **1**
1.1 Introduction 1
1.2 General background to Magnetic resonance imaging 2
1.3 The need for low field MRI 6
1.4 Theory of Magnetic Resonance 8
1.5 Generation of magnetic fields 8
1.6 Basic concepts of magnetic resonance (MR) 10
1.7 Magnetic resonance imaging (MRI) 12
1.8 Gradient Magnetic fields 13
1.9 Slice selection 13
1.10 Phase encoding 14
1.11 Frequency encoding 15
1.12 MRI relaxation 16
1.13 Repetition Time (TR) and Echo Time (TE) 18
1.14 Tissue contrast as a function of T1 and T2 19
1.15 MRI pulse sequences 23
1.15.1 Spin echo pulse sequence 23
1.15.2 Gradient echo pulse sequence 24
1.16 From signal to image 25
1.17 MRI hardware 26

1.17.1 The main magnet (B_o) coils 26
1.17.2 Gradient Coils 28
1.17.3 Radio frequency (RF) coils 30

Chapter 2
LITERATURE REVIEW OF THE LOW FIELD MRI SYSTEMS FOR POTENTIAL BRAIN IMAGING 32
2.1 PRE-PULSE MRI 32
2.1.1 Possible PRI detection technology 35
2.1.2 PMRI Switching circuits 39
2.2 Static electromagnet MRI systems 40

Chapter 3
DESCRIPTION OF THE PMRI SYSTEM 44
3.1 Basic electronic components of PMRI 44
3.2 The Bp switch 45
3.3 Gradient amplifiers 46
3.4 The Power supplies 47
3.5 The resonant circuits 47
3.6 Frequency filters 48
3.7 The frequency mixer 50
3.8 Signal acquisition and processing 51

Chapter 4
DESIGN CONSIDERATIONS AND FABRICATION OF THE PMRI SYSTEM 53
4.1 Design of the B_m coil 55
4.1.1 COMSOL simulation of the Bm coil system 62
4.1.2 Simulation results and discussion 64
4.2 Construction of gradient coils 66
4.2.1 Design of the Golay four saddle gradient coils 67
4.2.2 COMSOL set-up and simulation 68
4.3 Construction of the B_p coil 69
4.3.1 COMSOL simulation of B_p coil 70
4.4 Construction of RF coils 71
4.4.1 COMSOL simulation of the RF coil 73
4.5 Cost considerations 78
4.6 Other figures of the PMRI system 78

Chapter 5
CHARACTERIZATION OF THE PMRI SYSTEM **80**
5.1 Mapping the magnetic field homogeneity 80
5.1.1 Materials and methods 81
5.1.2 Results and discussion 83
5.2 Linearity of gradient magnetic fields 85
5.2.1 Materials and methods 85
5.2.2 Results and discussion 86
5.3 Power requirement and coil heating of the Bp coil 88
5.3.1 Methodology 90
5.3.2 Results and discussion 90
5.4 Construction and testing of electromagnetic radio frequency shield . 92
5.4.1 Theory 92
5.4.2 Theoretical illustration of absorption and reflection losses of aluminum and brass material used for EM shielding 95
5.4.3 Fabrication of shields of the RF shields 97
5.4.4 Experimental set-up to test the shielding effectiveness of the shields 97
5.4.5 Results and Discussion 97
5.5 Imaging experiments 101

Chapter 6
CONCLUSIONS AND RECOMMENDATIONS **107**
6.1 The Biomedical Engineering program at Mbarara University of Science and Technology-Uganda 108
6.2 Continuation of the project in Uganda 109
6.3 Increasing B_p and B_m magnetic field strengths 110
6.4 Radio frequency shielding 111
6.5 Clinical trial phase 113

Appendix A
The biomedical engineering curriculum for MUST **115**
A.1 Introduction and Justification 115
A.2 Course content 118

Bibliography **123**

List of Figures

1.1 Historical time-line of MRI technology. 6
1.2 Magnetic field profile of solenoid 10
1.3 Slice selection in MRI 14
1.4 Illustration of frequency encoding 16
1.5 Longitudinal relaxation 18
1.6 T1 and T2 relaxation times of common tissue types 20
1.7 Maximizing T1 contrast 21
1.8 Maximising T2 contrast 22
1.9 Spin Echo pulse sequence diagram 24
1.10 Gradient echo sequence diagram 25
1.11 Hardware components of MRI. 27
1.12 Helmholtz pair 28
1.13 The Golay coil configuration 29
1.14 Resonant Circuit. 31

2.1 Pre-polarized MRI 34
2.2 PMRI images of the human wrist 35
2.3 PMRI with SQUID sensing 36
2.4 Atomic magnetometer 37
2.5 Helmholtz design for low field MRI 41
2.6 Pineapple image using low field MRI 42

3.1 Block diagram of the PMRI system 45
3.2 Operational Amplifier 47
3.3 RLC resonant circuit 48
3.4 Band-pass filter 50
3.5 Frequency mixer 51

4.1 Geometry explaining Biot-Savart law 56
4.2 Leewhiting coil system 57
4.3 Design parameters of the Bm coils 60

4.4 Variation of the Bm magnetic field with coil crossection area 61
4.5 Comsol geometry set-up of the Bm coil system 62
4.6 Magnetic field uniformity variation with coil cross section area . . . 64
4.7 Maxwell coil pair 66
4.8 Saddle coils 67
4.9 Linearity of the x,y gradient magnetic fields 69
4.10 COMSOL model of Bp coil 71
4.11 RF saddle coil 72
4.12 3D model of the saddle coil 75
4.13 Field lines of saddle coil 76
4.14 Y-component of the magnetic field of a saddle coil 76
4.15 X-component of the magnetic field of a saddle coil 77
4.16 Z-component of the magnetic field of a saddle coil 77
4.17 Item costs 78
4.18 PMRI Drawings 79
4.19 Coil winding 79

5.1 The 3-axis positioner 82
5.2 Magnetic field map of the Bm magnet 84
5.3 Y-Gradient magnetic field map 87
5.4 X and Z gradient magnetic fields 87
5.5 Coil Heating and temeprature rise in imaging volume 91
5.6 Absorption and reflection loss 96
5.7 Steps in fabrication of shield 98
5.8 Experimental set-up 99
5.9 Photograph showing attenuated signal 100
5.10 Experimental results of shield effectiveness 101
5.11 Screen shot showing RF pulses and echo 102
5.12 Image of green pepper 104
5.13 Water tubes 105
5.14 Water melon 106

6.1 Magnetic field boosted by steel shielding 112
6.2 standing gradient generated by the shield 113

A.1 Course for content Year 1 119
A.2 Course content for Year 2 120
A.3 Course content for Year 3 121
A.4 Course content for Year 4 122

List of Symbols

MRI	Magnetic resoancnce imaging
PMRI	Pre-pulse magnetic resonance imaging
LMICs	Low and Middle Income Countries
MUST	Mbarara Universsity of Science and Technology
CSF	Cerebrospinal Fluid
WHO	WorldHealth Organization
SAR	Specific Absorption Rate
FDA	Food and Drug Administration
SSA	Sub-Saharan Africa

Acknowledgments

I would like first and foremost to express my gratitude to my advisor, Dr. Steven J Schiff first for getting me into Penn State and for his constant guidance and support throughout this project. Dr. Schiff continues to be my mentor and I am greatly indebted to him. Special thanks also go to Dr. Igor M Savukov for his technical expertise and for lending us some of his equipment to use in this research. I would also like to thank the rest of my thesis committee members for their valuable input and insight in this research project. My thanks also go to the members of the Schiff lab for their support in various aspects of this project. I would like to specifically thank Mr. Joshua Harper who joined me in this project about a year a go and has been very valuable in solid works design and Matlab coding.

Very special thanks go to my wife, Mrs. Phoebe Obungoloch who played the role of a single mother, taking care of our three children in Uganda while I was a way in the United States doing this research. Your support has been invaluable. And to the rest of my family, thank you.

Dedication

To my wife Phoebe Obungoloch and to our children: Vonah Apio, Vanessa Adongo, and Victor Obungoloch

Chapter 1

BACKGROUND AND SIGNIFICANCE

1.1 Introduction

Developing countries generally rely on medical technologies from the developed world. Most of these modern technologies are not designed to meet the specific challenges that plague developing countries. For example electricity coverage in Sub-Saharan Africa stands at about 33% [3]. This means that medical technologies that rely on electricity can only be used to serve a small proportion of the population. Even in medical facilities that have access to electricity, utilization of medical technologies is limited due to the limited technical expertise available to maintain these devices. Trained biomedical/clinical engineers and technicians that are necessary for the success of medical technologies are lacking in sub-Saharan Africa. As a result, some estimates show that up to "70% of laboratory and other medical equipment are either partially or completely out of service" [4].

There are currently two approaches being pursued to mitigate the problem

of limited medical technologies in sub-Saharan Africa; 1) Training of biomedical/clinical engineers and technicians to repair and maintain medical devices [5], [6] and 2) Developing appropriate medical technologies for such environments [7], [8]. The ultra-low field magnetic resonance imaging (MRI) project is therefore in line with the broad aim of innovating appropriate medical technologies for developing countries. The general experience of a PhD project at The Pennsylvania State University was also aimed at gaining the relevant expertise necessary for developing biomedical engineering training programs especially for Uganda where biomedical engineering is just emerging. While a low field MRI system has been developed, a biomedical engineering curriculum on which the undergraduate biomedical engineering program at Mbarara University of Science and Technology (MUST) is based was also partially developed in collaboration with the my thesis advisor.

1.2 General background to Magnetic resonance imaging

Theoretical discoveries of the principles of MRI date back to the late 1800s when Nikola Tesla discovered the rotating magnetic field in 1882 during his work on alternating currents. Although this was not directly related to magnetic resonance imaging (MRI), discovery was significant in starting to understand the directionality of magnetic fields and in 1956, the Tesla (T) was proclaimed by the International Electro-technical Commission-Committee of Action as one of the units for measuring magnetic field strength in honor of Nikola Tesla [9]. More important to MRI however was the the Stern-Gerlarch experiment of 1922 which established the concept of nuclei spin and magnetic moment [10]. It showed that certain atomic

nuclei posses an intrinsic spin and can be separated or influenced by a magnetic field depending on the orientation of the spin. This work, together with an earlier work developed by Joseph Larmor led to the realization that the intrinsic spin of atoms is influenced in a way that is proportional to the strength of the externally applied magnetic field [11]. The Larmor precession frequency, ω_o, was therefore established as

$$\omega_o = \gamma B_o \tag{1.1}$$

where γ is the gyromagnetic ratio, and B_o is the magnetic flux density of the applied magnetic field [12].

A more direct relationship between magnetic fields and MRI was discovered by Isidor I. Rabi in 1937 when he observed what he called Nuclear Magnetic Resonance (NMR). This is a condition where atomic nucleus is able to flip its principal axis of rotation by absorbing magnetic energy resulting into resonant peaks when exposed to a strong magnetic field. While Rabi demonstrated NMR by passing a molecular beam of particles through a vacuum, Felix Bloch and Edward Mills Purcell separately demonstrated the same phenomena with water and paraffin molecules [13], [14].

By the $1950s$, principles of NMR were fully explained and commercial instruments to observe resonant peaks of nuclei became available [15]. The field of NMR spectroscopy was one of the first fields to be developed around this period. Chemists at this time were able to verify the structure of different molecules contained in a particular compound. Having understood the interaction of magnetic signals with atomic nuclei and its ability to separate resonant peaks as it was being done in Chemistry, Raymond Vahan Damadian proposed the idea of whole body

NMR in 1969 ($http://www.fonar.com/pdf/doc_30.pdf$) and in the early 1970s, Damadian discovered relaxation time differences between cancerous and normal tissues, and suggested using these relaxation deferences for tumor detection using NMR [16]. Shortly after that, in 1973, Paul Lauterbur came up with another idea of using the principles of NMR to form images [17]. By this time it was now known that the atomic nucleus absorbs magnetic energy and releases that energy in form of radio frequency waves once the magnetic field was switched off and the magnitude of energy released was proportional to the number of nuclei. Using this principle, it was possible to tell tissue abnormalities for instance, since different tissues would have different number of nuclei.

Lauterbur later came up with the idea of localizing the position where the signal is being released from. He demonstrated that one magnetic field can be used to induce interaction with the nuclei and another magnetic field could be used to limit that interaction to a specific spatial dimension, essentially introducing the concept of magnetic field gradients [17].

However, the first clinical application of magnetic resonance imaging (MRI) can be attributed to Sir Peter Mansfield in which he imaged an in-vivo cross section of a human finger reported in his 1977 publication [18]. This was quickly followed by imaging the wrist by Hindshaw et at in 1977 [19], and another image of a cross section of the human chest by Damadian et al later that same year [20]. While these were still experimental and research images, Damadian and FORNA cooperation introduced the first commercial MRI scanner in 1980 (http://fonar.com/history.htm).

Other companies such as Brucker joined in the manufacturing of MRI systems and the first machines were built using permanent magnets. They weighed up to 100 tons, and had magnetic field strengths of up to 0.1 T. With the permanent mag-

net systems being overwhelmed by weight, resistive electromagnet systems were developed and could achieve fields as high as 0.35 T before they were limited by coil heating [21]. With the permanent and resistive electromagnet systems pushed to the limits, increase in magnetic fields could only come from another type of technology, the superconducting technology. Electric and Musical Industries (EMI), a company that was already making Computed Tomography (CT) scanners led the way in developing super conducting magnets by cooling using liquid helium and nitrogen. The introduction of superconductors made it possible possible to archive magnetic field strengths greater than 1.0 T [22]. The advent of superconductors ideally eliminated the technological hurdles of generating high magnetic fields but introduced yet another problem of cost.

With the technological limitations now surmounted and understanding the costs involved, debate arose about the optimal field strength for MR imaging. Higher field strengths means higher signal to noise ratio (SNR) and therefore better image quality, faster imaging times and ability to perform other diagnostic and research procedures such as functional magnetic resonance imaging (fMRI) and NMR spectroscopy - all these at very high costs. Choosing to lower the magnetic field strength for MRI on the other hand would minimize costs, reduce energy requirements, minimize technical complexities, and lower maintenance costs among other advantages but at the expense of image quality. In this "field strength war", the high field strength proponents took the day and the market for MRI systems was essentially defined. Low income countries, and by far the largest population of the world were essentially excluded from accessing MRI services.

Figure 1.1 shows a historical time-line of the development of MRI technology.

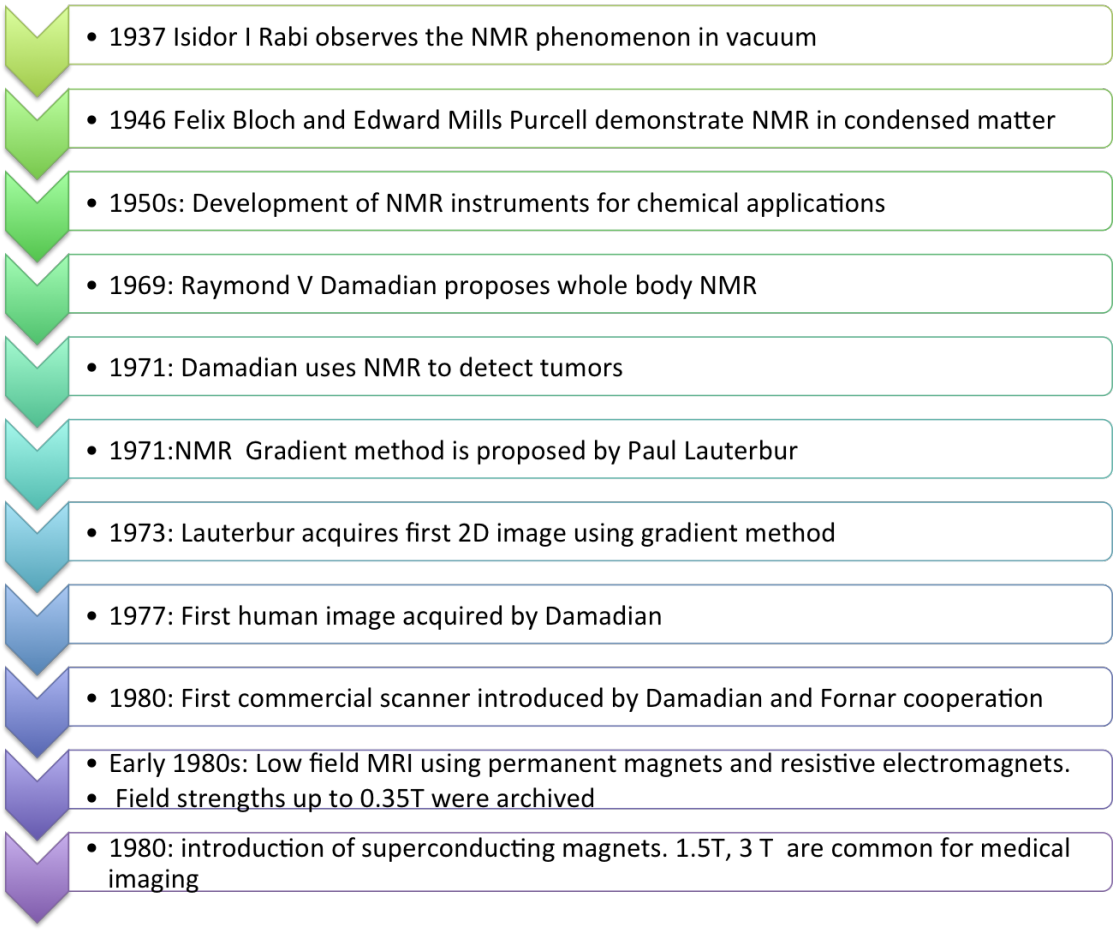


Figure 1.1. Historical time-line of MRI technology.

1.3 The need for low field MRI

While clinical use for low field MRI may be limited because of its low image quality and inability to perform other diagnostic scans, there is increased need for such low cost imaging systems. For instance the increased use of CT, X-ray and ultrasound imaging systems over the years can be attributed to the low cost and infrastructure requirements for such systems as opposed to MRI. Of these technologies, x-rays and ultrasound are inadequate for brain imaging leaving CT as the dominant brain imaging modality. Portable CT units have been developed making its access much easier [23], [24]. In developed countries however, where MRI is accessible, the use

of CT is limited to regions outside of the brain. This is not possible in developing countries where the best brain imaging modality available is CT. Increasing use of CT therefore means increasing radiation which comes with associated risks(6).

The risks of cancer attributed to radiation doses as a result of using CT is significantly high (7). There is further evidence showing that radiation dose and risk of death from cancer attributable to radiation is much higher in children than adults [1] . These risks underscores the need for safe and inexpensive imaging modalities.

Furthermore, there has never been a compelling disease requiring low resolution images to diagnose and treat. Hydrocephalus is a condition where there is excessive accumulation of cerebrospinal fluid in the brain leading to distention of the ventricular system of the brain [25]. More than 60% of hydrocephalus in Africa is caused by infections usually during childbirth or in the early stages of life - a condition known as post infectious hydrocephalus (PIH). Other causes of hydrocephalus include trauma, intra-cranial hemorrhage and congenital abnormalities [26].

The CURE international (https://cure.org/) estimates that 79% of infants born with hydrocephalus are in the developing world. There are over 100,000 new cases of PIH in Sub-Saharan Africa (SSA) each year and globally, PIH is the most common neurological disease in children requiring brain imaging for neurosurgical intervention [27]. The economic burden of PIH has been estimated at between $26 million-$48 million per year in SSA based on the World Health Organizations disability adjusted life year statistics (DALY) [28].

The CURE children's hospital in Uganda specializes in treatment of hydrocephalus. Because of the absence of MRI, CURE hospital uses CT exclusively to repeatedly image and monitor hydocephalic children, and therefore putting them

at high risks of radiation induced cancers. In hydrocephalic children, the critical issue is to distinguish between brain matter and cerebrospinal fluid (CSF) so as to be able to make treatment decisions. This distinction does not require very high resolution images to make [26] and therefore an appropriate low field MRI system would be able to provide images that make the distinction possible.

1.4 Theory of Magnetic Resonance

1.5 Generation of magnetic fields

MRI technology exploits the interaction between atomic nucleus (mostly the hydrogen proton) with magnetic fields. The MRI therefore consists of systems that generate and control magnetic fields as well as measure and encode the resulting signals from their interactions with the spinning nuclei.

The discovery of the relationship between current and magnetic fields can be attributed to Hans Christian Oersted who found that the compass needle deflected in the presence of a current carrying wire in the 1820s [29]. This discovery, which is considered accidental by some historical accounts, was closely followed by Amperes theory that relates magnetic fields to the electric currents that produce them [30]. Ampere showed that a current carrying wire generates a magnetic field around itself-given by

$$\oint B\, dL = \mu_o I \tag{1.2}$$

where B is the magnetic field generated, I is the current flowing in the wire and μ_o is the permeability of free space. From equation 1.2, the magnetic field at any

distance r from the current carrying wire can therefore be written as

$$B = \frac{\mu_o I}{2\pi r} \tag{1.3}$$

Equation 1.3 is a fundamental equation upon which generation of magnetic fields for MRI applications are based. It shows that magnetic fields can be generated by passing currents around loops of wires (coils). A solenoid is one such coil, which is easy to design and construct. The magnetic field generated at the center of the solenoid is given by

$$B = \mu_o n I \tag{1.4}$$

where n is the number of turns per unit length. While solenoids are one of the easiest designs of electromagnetic coils, they are not very ideal for MRI applications because they do not generate very homogeneous magnetic fields. The magnetic field of a solenoid is much higher at the center and tapers down to the edges (Figure 1.2) [12].

To obtain higher magnetic field homogeneity over a larger volume, most MRI designs use sets of coils with precise positioning along the z-axis instead of the conventional solenoid coils. For instance the magnetic field at a point r generated by a coil loop of radius a is given by

$$B = \frac{N I \mu_o a^2}{2(a^2 + r^2)^{\frac{3}{2}}} \tag{1.5}$$

where N is the number of turns of the wire loop. By arranging coil loops in various configurations, one can get uniform or varying magnetic fields.

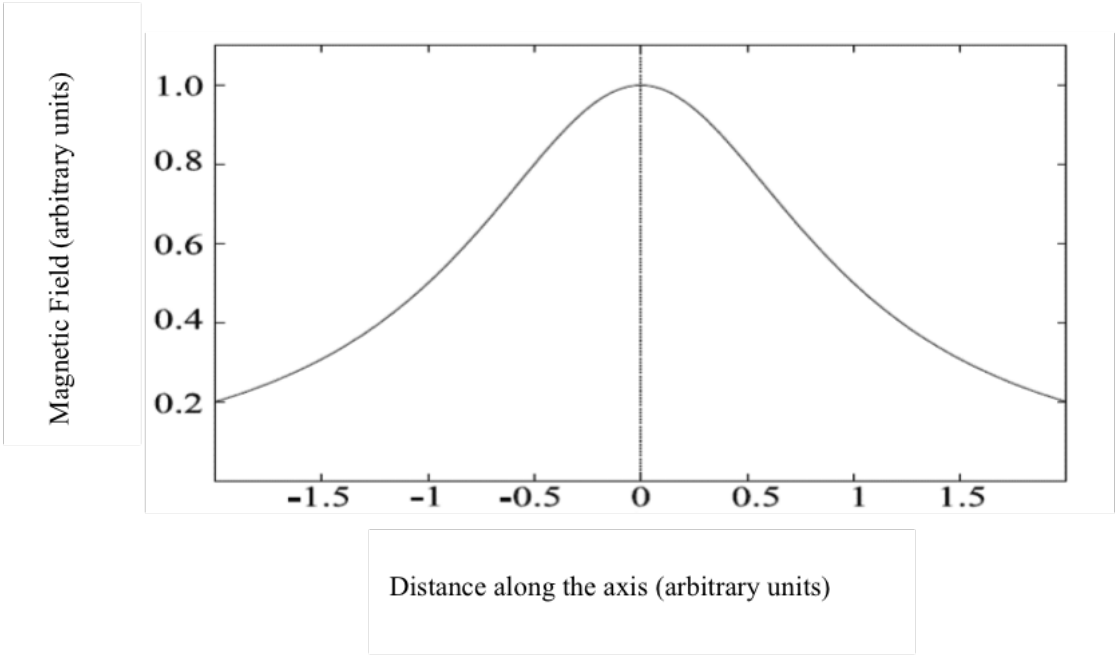


Figure 1.2. Magnetic field along the axis of a solenoid coil (From [12]).

1.6 Basic concepts of magnetic resonance (MR)

MR imaging gained wide acceptance immediately after its introduction in the 1970s because of its use of non-ionizing radiation, high resolution and good contrast especially between soft tissues. The non-invasiveness and ability to acquire images in any two or three-dimensional planes are some of the additional advantages of MRI. MRI takes advantage of the fact that a hydrogen nucleus within the body spins on its own axis and since the nucleus is charged, it generates a magnetic moment and behaves more or less like a small magnet. Because of the enormous number of charged nuclei and their random orientation, their fields cancel out and the body experiences no net magnetization. However, in the presence of a strong external magnetic field B_o produced by the MRI, the individual spins tend to align with the external magnetic field giving rise to a net magnetization M_o [31] given

by

$$M_o = \frac{\gamma^2 h^2 B_o N_s}{16\pi^2 kT} \tag{1.6}$$

where γ is the gyromagnetic ratio, h is Planks constant, B_o is the external magnetic flux density, N_s is the number of spinning nuclei, k is the Boltzmanns constant and T is the temperature. This magnetization precesses around the direction of the applied magnetic field B_o with a Larmor frequency ω_o given in equation 1.2. The net magnetization M_o is in the direction of the externally applied magnetic field B_o, and since it is much smaller in magnitude compared to B_o, its detection requires that it is tipped away from the direction of B_o. This is made possible by the application of a radio frequency (RF) magnetic field B_1 orthogonal to B_o. The frequency of the RF field has to match the Larmor frequency ω_o of the net magnetization. Once this is done, the precessing protons will tip away from the direction of B_o by an angle α, which is proportional to the strength of the B_1 magnetic field and the time duration τ over which the RF field is applied (Equation 1.7).

$$\alpha = \gamma B_1 \tau \tag{1.7}$$

For spin echo pulse sequences, α of $\frac{\pi}{2}$ is preferred since it provides maximum signal for long repetition times [12]. If we assume B_o to be a long the z- direction, the application of the RF pulse therefore tips the magnetization onto the x-y plane. The precession of the magnetization about the x-y plane can induce an electrical voltage onto a receiver coil placed in that plane. From Faradays law, the induced emf is given by

$$emf = \oint \frac{d}{ds}(M.B_r c)d^3r \tag{1.8}$$

where $B_r c$ is the magnetic field produced by the RF coil per unit current, M is the magnetization vector whose magnitude is proportional to M_o given in equation 1.6, d^3 is an infinitesimal volume and r is the position of the coil from the magnetization source. The signal detected by the receiver coil is therefore proportional to the emf generated in the coils.

1.7 Magnetic resonance imaging (MRI)

So far we have explained MR signal generation and detection; however, the process of obtaining an image from these signals is more complex than this. The previous section can be summarized in the following steps: 1) application of an external static magnetic field B_o to generate a net magnetization in the z-direction, 2) application of RF magnetic pulse to tip the magnetization onto the x-y plane, 3) Precession of the magnetization vector in the the x-y plane induces an electrical signal in the receiver coil, 4) Detection of the induced electrical signal.

The signal detected by the receiver coil is from the whole object or part of the object being imaged and has no spatial information which is a key component in image reconstruction. For imaging to be possible, we must be able to correlate the signal detected with its spatial source within the object being imaged. This is done by the use of gradient magnetic fields.

1.8 Gradient Magnetic fields

From equation 1.2, the Larmor frequency of the protons is proportional to the local magnetic field experienced by the protons. Gradient magnetic fields work to vary the local field according to the spatial location of the proton thereby varying the Larmor frequency according to location of the spins. Gradients are applied in the x, y and z directions to give a full 3D spatial mapping of the signal location. By varying the local magnetic field experienced by protons according to location, we are able to get slightly different signals in terms of frequency and amplitude from these locations. Differentiation of signal amplitude and frequency according to position provide the contrast necessary to form an image. Gradients in MRI are therefore used for slice selection, phase encoding and frequency encoding.

1.9 Slice selection

As the name suggests, the slice selection gradient is used to select a 2D plane through the object being imaged. We explained earlier that the application of the RF pulse of the right frequency tips the magnetization onto the x-y plane or the transverse plane as is more appropriately called. By spatially varying the precession frequency along the z-axis for example, applying an RF pulse of a certain frequency range will only tip the magnetization corresponding to the frequency within a certain region of the object being imaged (figure 1.3) [32]. To cover the required field of view (FOV), the bandwidth of the RF field is selected accordingly. Changing the bandwidth of the RF pulse or varying the strength of the gradient magnetic field, G_{sl}, can change the slice thickness. Slice thickness d_{sl} is thus given

by

$$d_{sl} = \frac{\Delta\omega}{\gamma G_{sl}} = \frac{2\pi\Delta f}{\gamma G_{sl}} \tag{1.9}$$

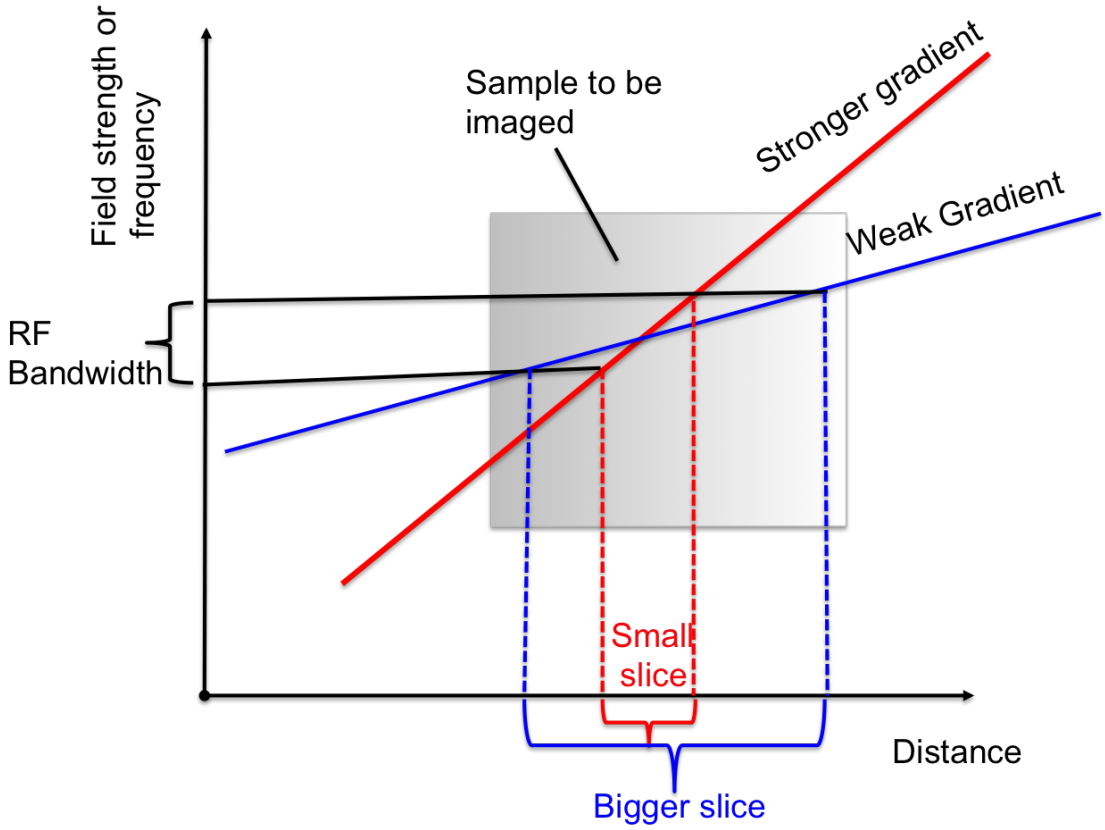


Figure 1.3. Slice selection in MRI

1.10 Phase encoding

After slice selection, a re-phasing gradient is applied to bring back spins within the slice to the same precession frequency and phase. Once they are precessing with the same frequency and phase, application of an additional gradient along one of the axes in the transverse plane for example will change the precession frequency of protons according to their location. This will allow some protons to precess faster than others thus altering their phase relative to each other. When the phase

encoding gradient is turned off, the protons will go back to precess at the Lamor frequency but will retain the phase differences introduced earlier by the gradient. The phase change accumulated by the spins $\phi_{pe}(G_y, \Delta t)$, is directly proportional to the strength of the phase encoding gradient (G_y) and the duration over which the gradient is applied (Δt), and can be given by

$$\phi_{pe}(G_y, \Delta t) = \omega_y \Delta t = (\gamma G_y \Delta t) \tag{1.10}$$

1.11 Frequency encoding

While phase encoding alters the phase of the precessing proton nuclei, it does not change the frequency of precession. By applying another gradient field in the third direction, we can vary the precession frequency of the spins according to their location (Figure 1.4). After altering the frequency and phase of the precessing protons using the frequency and phase encoding gradients respectively, it now becomes possible to use Fourier transforms to form an image from these signals.

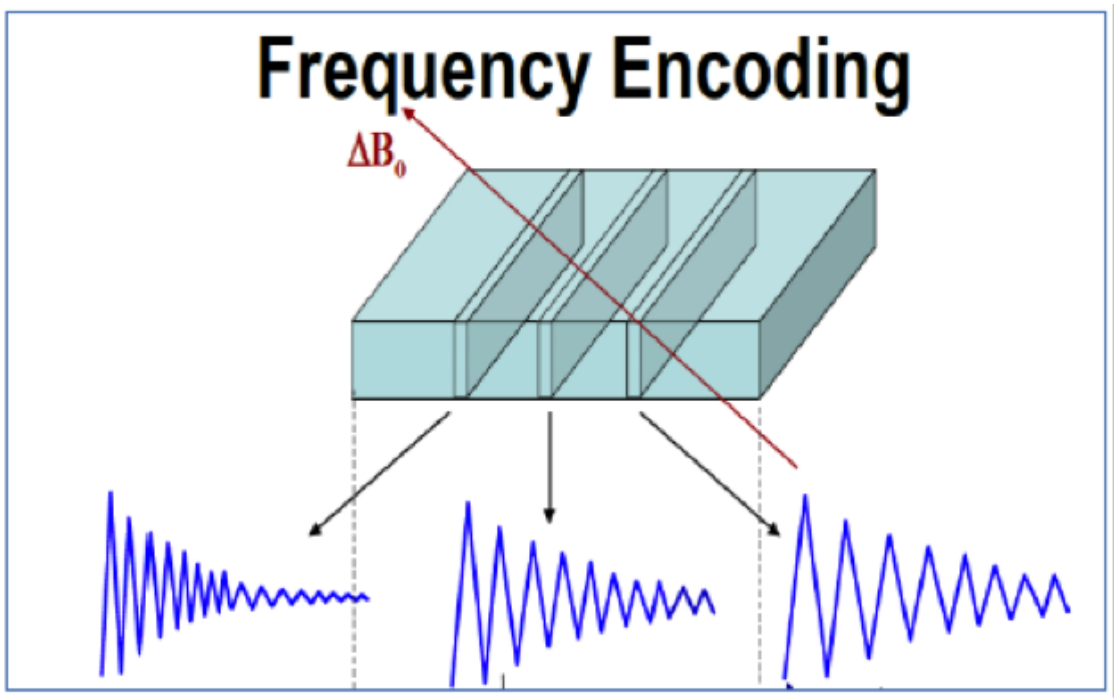


Figure 1.4. Illustration of frequency encoding [33]

.

1.12 MRI relaxation

Recall that before the application of an RF pulse to tip the magnetization onto the transverse plane, there existed an equilibrium magnetization M_o in the z-direction as a result of the static B_o magnetic field. When the RF magnetic field is applied momentarily, a component of M_o, which we will call M is flipped onto the transverse plane. The precession of M in the transverse plane is described by the Bloch equation [12] as

$$\frac{d\vec{M}}{dt} = \gamma \vec{M} X \vec{B} \tag{1.11}$$

where B is the applied magnetic field. Because of energy exchange between the magnetization M and the surrounding lattice, there will be components of the

magnetization vector both in the transverse and longitudinal directions. Therefore the rotational motion of magnetization vector can be decomposed in two directions as $\frac{dM_z}{dt}$ and $\frac{dM_{xy}}{dt}$. At the instant of application of the RF pulse (assuming a $\pi/2$ pulse), M_z is zero but it grows back to its equilibrium value M_o according to the equation

$$\frac{dM_z}{dt} = \frac{1}{T_1}(M_o - M_z) \tag{1.12}$$

where T_1 is the longitudinal relaxation time. It is empirically determined and represents the time taken by the longitudinal magnetization to recover to 63% of its original value. Equation 1.12 can be evaluated to give;

$$M_z(t) = M_z(0)e^{\frac{-t}{T_1}} + M_0(1 - e^{\frac{-t}{T_1}}) \tag{1.13}$$

T_1 is also known as the spin-lattice relaxation because the longitudinal magnetization relaxes back to equilibrium as a result of energy exchange with the surrounding lattice. The other component of the magnetization as mentioned earlier is the transverse or xy component. This is maximum immediately after application of the RF pulse and can be described by the equation

$$\frac{dM_{xy}}{dt} = -\frac{1}{T_2}(M_o) \tag{1.14}$$

Solving equation 1.14 gives

$$M_{xy} = M_o e^{-\frac{t}{T_2}} \tag{1.15}$$

It can be seen that the transverse magnetization decays exponentially with

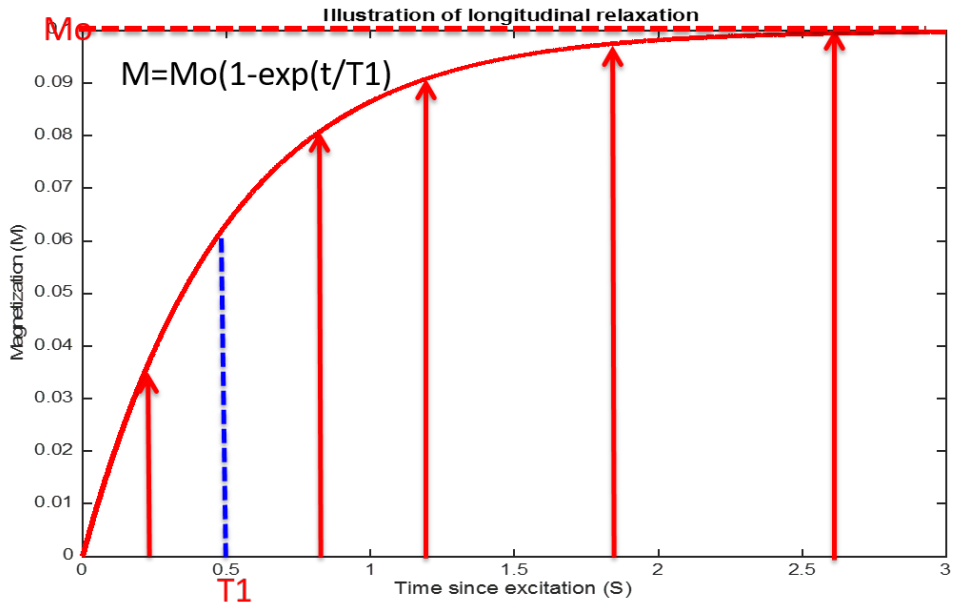


Figure 1.5. Longitudinal relaxation. Adapted from http://mri-q.com/what-is-t1.html

time. T2 is the time taken for the transverse magnetization to decay to 37% of its original value. T2 is also referred to as the spin-spin relaxation time because the interaction between spins causes the protons to go out of phase with each other causing decay of the resultant signal. These relaxation times are very important in determining the timing sequence of the RF pulse and signal acquisition.

1.13 Repetition Time (TR) and Echo Time (TE)

MRI signal that is detected is the component of the magnetization in the xy plane since it is orthogonal to Bo. This transverse magnetization is realized as a result of the application of the RF pulse. Repetition time TR is the time between two successive RF pulses. The value of TR determines how much longitudinal magnetization M_z has recovered before another spin excitation pulse is applied. From Equation1.13, assuming that $M_z(0)$ is equal to zero, M_z becomes

$$M_z(t) = M_o(1 - e^{-\frac{t}{T_1}}) \tag{1.16}$$

When $t = TR$

$$M_z(t) = M_o(1 - e^{-\frac{TR}{T_1}}) \tag{1.17}$$

From equation 1.17, it can be seen that as TR increases, the signal M_z approaches M_o. This means that the longer you wait to apply another excitation pulse, the more signal you will have to flip onto the transverse plane.

On the other hand, when the magnetization is flipped onto the xy plane, some time period is normally required between the application of the excitation pulse and the acquisition of the resulting signal. This time delay is called echo time, TE. Caution must be taken in selecting the value of TE because the signal being acquired decays according to equation 1.15.

$$M_{xy}(t) = M_o e^{-\frac{TE}{T_2}} \tag{1.18}$$

Delays in acquiring the signal are penalized by decay of the signal.

1.14 Tissue contrast as a function of T1 and T2

Different tissues have different relaxation time constants $T1$ and $T2$. Figure 1.6 shows the differences in relaxation times of different tissue types at 1.5T [12]. This implies that at a given value of TR, each tissue type will have a different value of longitudinal magnetization or signal. To maximize contrast between tissue types, the repetition time TR of the RF pulse is chosen such that the difference in signal between the tissue types of interest is at maximum value (Figure 1.7). For example, white matter with a short $T1$ relaxation time will have a higher signal compared

to cerebrospinal fluid (CSF) at a TR of 500 ms (Figure 1.7).

Tissue type	T1 (ms)	T2 (ms)
Gray matter	950	100
White Matter	600	80
Muscle	900	50
Cerebrospinal fluid	4500	2200
Fat	250	60
Blood	1200	100-200

Figure 1.6. T1 and T2 relaxation times of common tissue types [12]

Similarly, at a given value of TE, different tissue types will have different signals remaining in the transverse plane because of the differences in T2 relaxation. Figure 1.8 shows that T2 contrast increases with TE up to a point where additional increase in TE will result into reduced T2 contrast. TR and TE can be manipulated to generate images which are either T1 weighted or T2 weighted. If for example a long TR and a short TE are chosen, there will be no T1 contrast between tissues but relatively good T2 contrast. The resulting image is said to be T2 weighted. The other way of getting contrast between tissues is by using the actual number or density of protons within a specified voxel or pixel of tissues. Depending on the TR and TE, tissues with different proton densities can be manipulated to give different signal strengths from which image contrast can be achieved. These types of images are referred to as proton density weighted images.

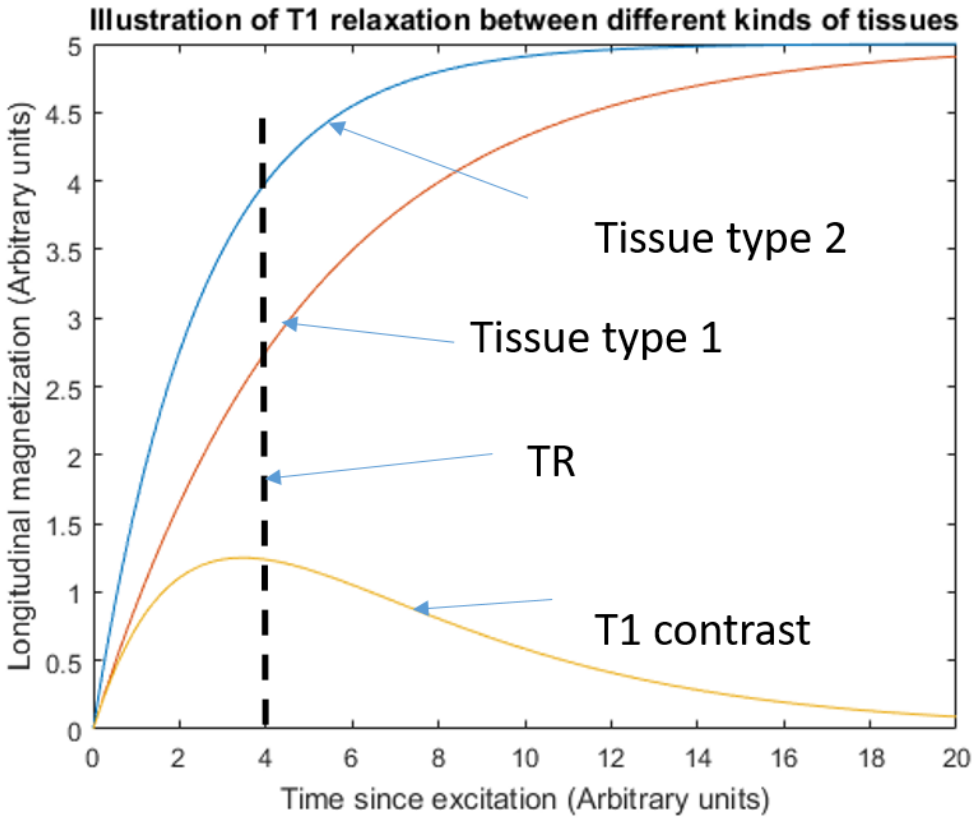


Figure 1.7. The red and blue curves show different tissue signals at different times. The yellow curve shows the contrast between the two tissues. The TR that maximizes contrast between the tissues is shown (Adapted from [33])

.

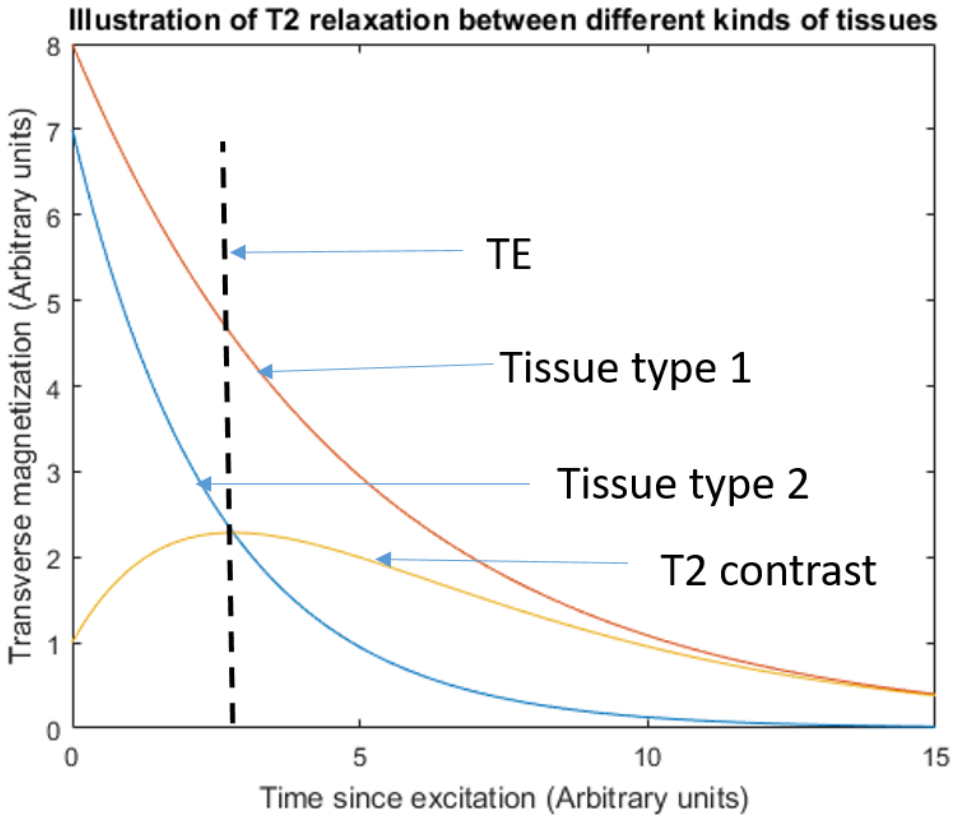


Figure 1.8. T2 Contrast: The blue and red curves show signal decay of different tissue types over time. The yellow curve shows the T2 contrast between the two tissues. T2 contrast is maximized by choosing appropriate echo time, TE as shown (Adapted from [33])

1.15 MRI pulse sequences

The basic MRI pulse sequence is a series of excitation RF and gradient pulses aimed at generating data that can be transformed into an image. The MRI pulse sequence can be illustrated with a timing diagram showing intervals at which RF and gradient pulses are turned ON and OFF. In its general terms, it consists of selecting a slice made possible by simultaneous application of the RF pulse and slice select gradient G_{ss}, followed by phase encoding step in which the phase encoding gradient, G_{pe} is turned ON. The last step is acquisition of data in the presence of frequency encoding gradient, G_{fe}. This process is repeated several times until the whole object is scanned. Several pulse sequences are derived by changing the order in which the gradient and RF fields are applied. The most common pulse sequences are the spin echo and gradient echo pulse sequences.

1.15.1 Spin echo pulse sequence

The spin echo pulse sequence [34] consists of a 90^o excitation RF pulse applied at the same time when the slice selection gradient is turned on. This ensures that only spins from a thin slice are excited and tipped onto the transverse plane. After the 90^o pulse, the phase encoding gradient is turned on. After a time $\frac{TE}{2}$, a refocusing 180^o RF pulse is then applied to recover the spin-spin relaxation loss that will have occurred. This is again done while the slice select gradient is on. The signal echo appears after a time TE and is recorded while the frequency-encoding gradient (also clled the read-out gradient) is on (Figure 1.9).This process is repeated untill the whole k-space is filled up.

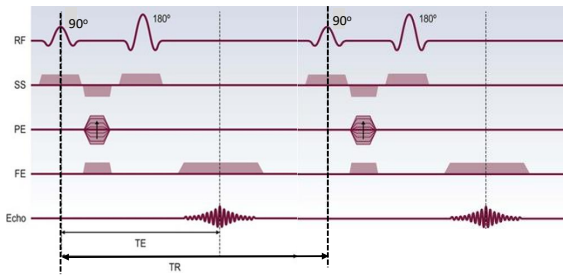


Figure 1.9. Spin Echo pulse sequence diagram ([35])

1.15.2 Gradient echo pulse sequence

Unlike spin echo, the gradient echo pulse sequence [34] does not use the 180^o and the initial RF pulse tips the spins to an angle α, usually less than 90^o. A phase encoding gradient is applied to the signal before a read out gradient is finally applied during signal acquisition. The read out gradient is first applied in the reverse direction to mitigate the effects of signal decay due to spin-spin relaxation (Figure 1.10).

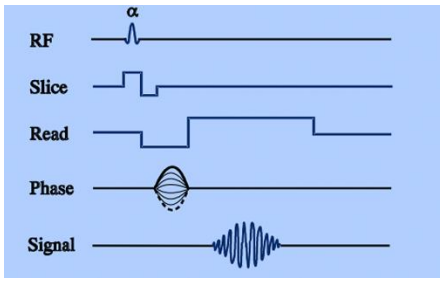


Figure 1.10. Gradient echo sequence diagram ((http://mri-q.com))

1.16 From signal to image

MRI signal is acquired in what is called the k-space. This is a temporary coordinate system in which complex image data is stored during MRI data acquisition. The signal from each data point in k-space corresponds to the sum of all signals from the whole object being imaged and can be written as

$$S(G_x, \tau_{pe}, G_y, t) \approx \iint \rho(x,y) e^{-j\gamma G_y y \tau_{pe}} e^{-j\gamma G_x x t} dxdy \tag{1.19}$$

where $\rho(x,y)$ is the proton density in that voxel, G_y and G_x are the phase and frequency encoding gradients respectively, and τ_{pe} and t are durations over which the gradients are applied.

By defining K_x and K_y as $k_x = \frac{1}{2\pi} G_x t$ and $k_y = \frac{1}{2\pi} G_y \tau_{pe}$, Equation 1.19 becomes

$$S(G_y, \tau_{pe}, G_x, t) \approx \iint \rho(x,y) e^{-j2\pi k_y y} e^{-j2\pi k_x x} dxdy \tag{1.20}$$

From equation 1.20, it can be deduced that the acquired signal in k-space is a Fourier transform of the imaged object in the x-y coordinate system. Thus using inverse Fourier transforms,

$$\rho(x,y) \approx \iint S(k_x,k_y)e^{j2\pi(k_x x+k_y y)}dk_x dk_y \tag{1.21}$$

$k-$space data can be digitized according to signal density from each voxel. The digitized data can now be transformed into an image of the object [32].

1.17 MRI hardware

The hardware of an MRI constitutes the highest percentage of the capital cost of the MRI system. The whole system consists of a number of magnetic fields generated by coils arranged in different configurations using the principles of magnetic field generation described earlier. These coils include the super conducting or main magnet coil, the gradient coils and the radio frequency (RF) coils (Figure 1.11).

1.17.1 The main magnet (B_o) coils

The main idea behind the Bo coils is to generate a strong homogeneous magnetic field normally along the z-direction which is responsible for polarizing proton spins. To achieve the required magnetic field strength and homogeneity, coil configurations such as the Helmholtz pair [12] can be adopted. This uses two loops of wires carrying current in the same direction (Figure 1.12), giving a magnetic field governed by the equation

$$B_z = \frac{\mu_o N I a^2}{2(a^2+(z+s)^2)^{\frac{3}{2}}} + \frac{\mu_o N I a^2}{2(a^2+(z-s)^2)^{\frac{3}{2}}} \tag{1.22}$$

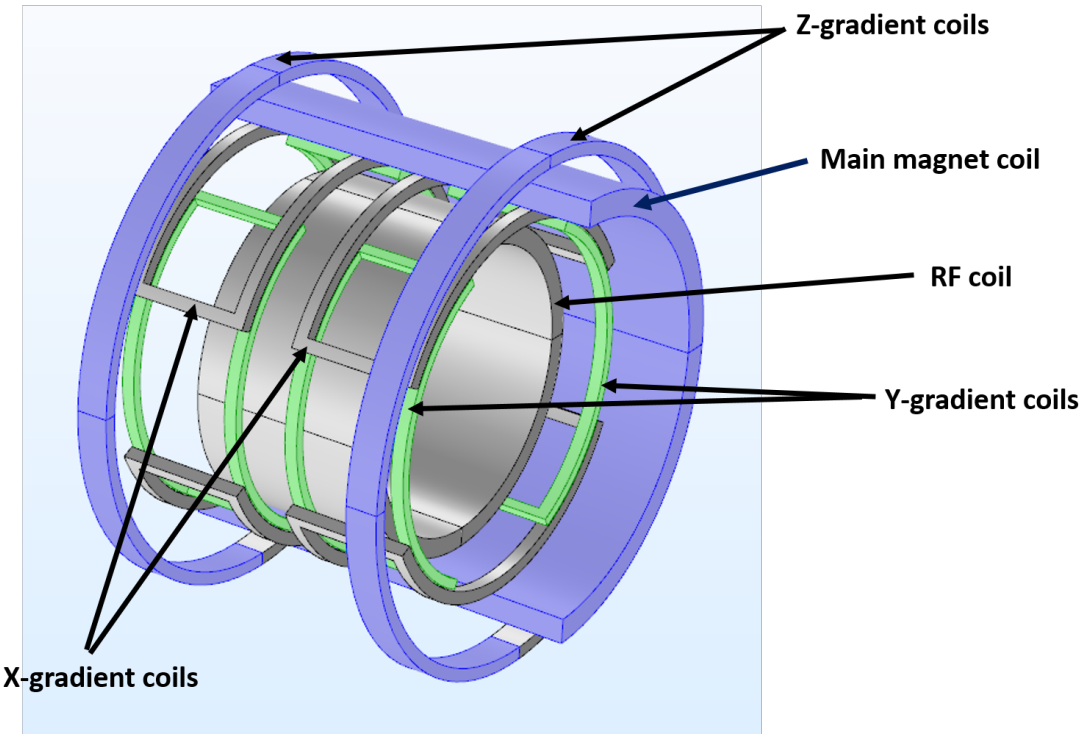


Figure 1.11. Hardware components of MRI.

where a is the radius of the loops, s is their position along the z-axis and N is the number of turns. To get a relatively homogeneous magnetic field, the recommended coil separation for a Helmholtz coil pair is $2s = a$. However, a single Helmholtz pair may not give the homogeneity required of the B_o field. As a result, a number of Helmholtz coil pairs at different locations along the z-axis may be used.

Magnetic field homogeneity is not the only requirement for the B_o field. The strength of such a magnetic field is one major factor to be considered. The magnetic field strength is directly proportional to the number of turns and the current passing through the loops. Achieving high field strength requires thousands of turns and hundreds of Amperes of currents. While increasing the number of turns will greatly impact on the weight and resistance of the system, passing high currents through a conductor generates results in considerable heating because of

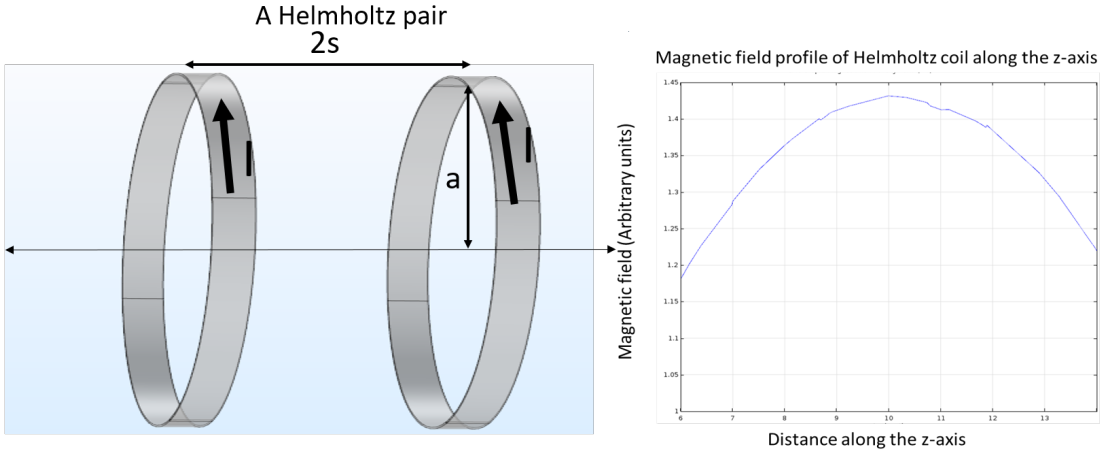


Figure 1.12. The Helmholtz coil pair. The left shows the positioning of the coils along the Z-axis and the figure on the right shows a one dimensional magnetic field generated by the Helmholtz coils

conductor resistive losses. For conventional MRI therefore, super conductors with negligible resistances are used. These super conductors are further cooled using liquid helium and nitrogen to maintain a stable temperature of about 4K. The conductors are directly immersed in liquid helium. To reduce the rate of evaporation of helium, a layer of liquid nitrogen is added [36]. Current clinical scanners using super conductor technology have field strength between 1.5T to 3T with animal and experimental scanners having field strengths of up to 20T. These magnetic field strengths are not possible to achieve without enormously increasing the cost of the MRI system.

1.17.2 Gradient Coils

While the B_o coils generate a static homogeneous magnetic field, gradient coils are designed to generate linearly varying magnetic fields in the x-,y-, and z-directions. Unlike the Bo magnetic field, these gradient magnetic fields are turned on and off depending on the need. For most MRI configurations, the z-gradient is designed

using Maxwell pair of coils. Like the Helmholtz pair, they consist of two loops of wire but carrying current in opposite directions. The magnetic field generated in this coil pair is governed by the equation

$$B_z = \frac{\mu_o N I a^2}{2(a^2 + (z-s)^2)^{\frac{3}{2}}} - \frac{\mu_o N I a^2}{2(a^2 + (z+s)^2)^{\frac{3}{2}}}, \tag{1.23}$$

Where again $2s$ is the separation of the coils just like in the Helmholtz pair (Figure 1.12).

Gradient magnetic fields in the plane transverse to the z-axis are generated by an arrangement of saddle coils first described by Marcel Golay in 1958 [37] (Figure 1.13). The direction of currents and angles of curvatures are chosen to generate the most uniform linear field in the region of interest.

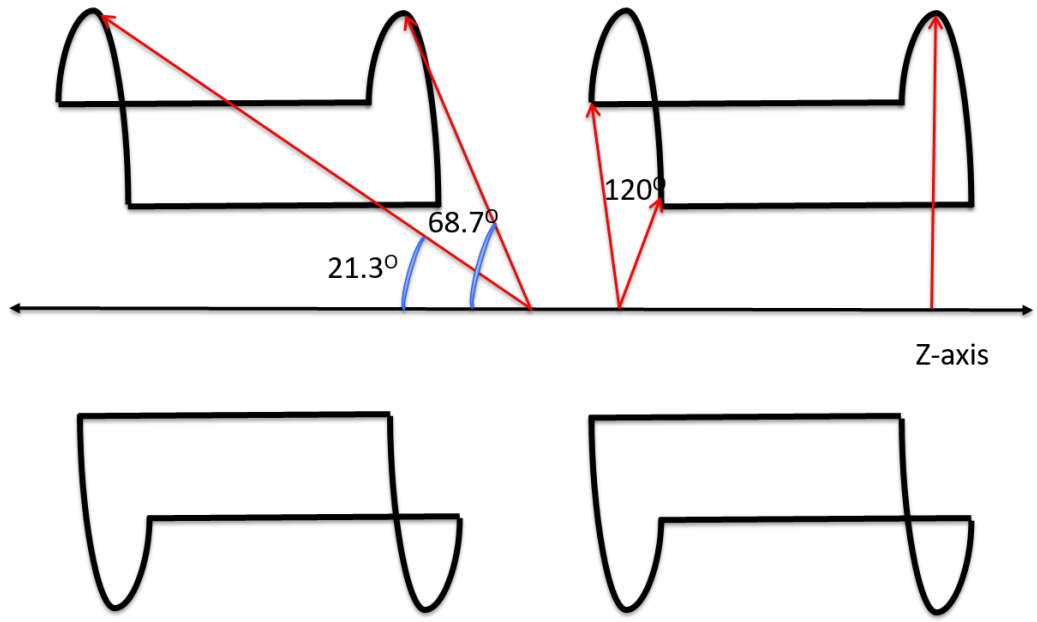


Figure 1.13. Configuration of the Golay pair commonly used to generate gradient magnetic fields in the x-and y-directions.

1.17.3 Radio frequency (RF) coils

The next set of MRI coils are the RF coils. The RF coils are designed to generate magnetic fields at frequencies matching the precession frequency of the spinning nuclei magnetization. Unlike other MRI coils, RF coils are made from resonant circuits containing resistance R, inductance L and capacitance C, normally referred to as an RLC circuit. Consider an RLC circuit in 1.14, the current I flowing in such a circuit is given by

$$I_rms = \frac{V_{rms}}{\sqrt{R^2 + (\omega L - \frac{1}{\omega C})^2}} \tag{1.24}$$

Where ω is the angular frequency. When the frequency of the circuit is varied, there will reach a point where $(\omega L - \frac{1}{\omega C})^2 = 0$ giving $\omega = \frac{1}{\sqrt{LC}}$ or $f = \frac{1}{2\pi\sqrt{LC}}$ At this condition, the circuit will have the least resistance to current flow and therefore maximum response.

RF coils are therefore designed with capacitance and inductance specifically chosen to match the resonant frequency of precession, - the Lamor frequency. Apart from the resonant frequency matching the Lamor frequency, RF coils are also required to produce magnetic fields that are orthogonal to the B_o field [38].

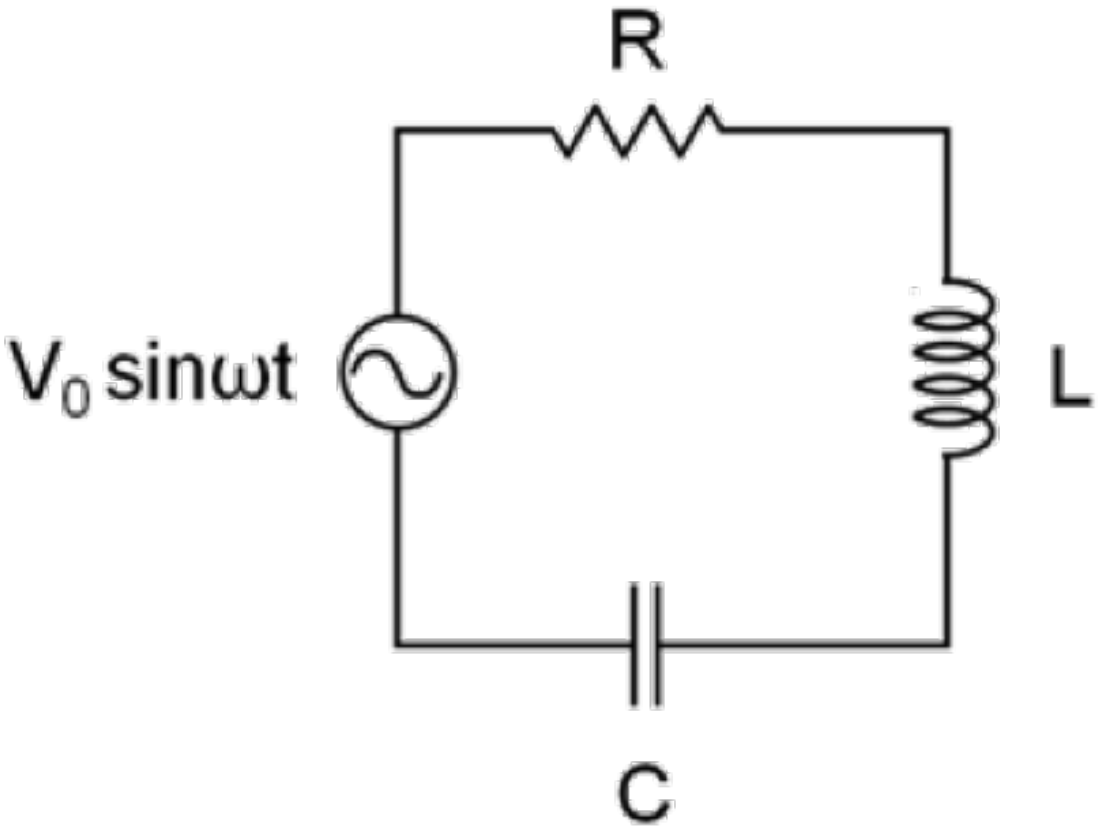


Figure 1.14. Resonant Circuit.

Chapter 2

LITERATURE REVIEW OF THE LOW FIELD MRI SYSTEMS FOR POTENTIAL BRAIN IMAGING

2.1 PRE-PULSE MRI

Generating strong magnetic fields require high electric currents and thousands of turns of superconducting wire immersed in cryogens. To minimize system costs, the pre-pulse MRI system uses resistive conductors without the need for cryogenics. However, generating magnetic fields using ordinary resistive conductors creates considerable heat as a result of resistive losses. While the strength of the magnetic field generated depends on current flowing in the coils, the amount of heat generated depends on the square of the current. This therefore limits the magnetic field that can be generated before the conductors burn out.

Pre-pulse MRI (PMRI) tries to limit this excessive heat dissipation by separating the B_o magnetic field into two components - the static, relatively weak

magnetic field strength component called the Bm and the relatively strong pulsating component called the Bp. The stronger magnetic field, (Bp) is switched on to polarize the spins and then switched off before the signal is acquired. The weaker magnetic strength Bo is used to set the Lamor frequency of the spins. This way, signal can be maximized while minimizing heat generated by resistive losses in the copper coils. While the Bm magnetic field is required to be highly homogeneous within a few parts per million (ppm), the Bp field can have inhomogeneities of up to 30% [39]. The magnetic field strengths proposed for these systems were in tens of millitesla for Bm and hundreds of millitesla for Bp, however rapid acquisition sequences may allow fields of up to one Tesla to be used. This approach was first proposed by Conolly et al in 1993 [40].

Connolly and group then set out to demonstrate the feasibility of their proposed device and in 1996, they constructed a prototype readout pre-pulse MRI magnet with field uniformity of less than 40 ppm within a 10 cm x 10 cmm x 10 cm region of interest [41]. This was a six-coil magnet system with the Bm field strength reaching 54 mT, Bp field of up to 0.4 T and weighing approximately 110 kg [42]. Development of the PMRI system continued in the subsequent years with construction of the other components including the gradient and radio frequency coils. By 2001, Connolly and group had constructed a fully-fledged PMRI scanner with a pre-polarizing field of 0.4 T and read out field of 25 mT. With this, they were able to acquire images of a human wrist [42]. As can be seen from the acquired images in figure 2.1, PMRI at this point in time could not reveal much detail on which clinical decisions could be based. However, it was able to demonstrate feasibility of the PMRI system and its potential contribution to medical imaging.

To improve this system, there was need to optimize the pulse sequences and increase the magnetic field strength. Using spin echo pulse sequence and a rela-

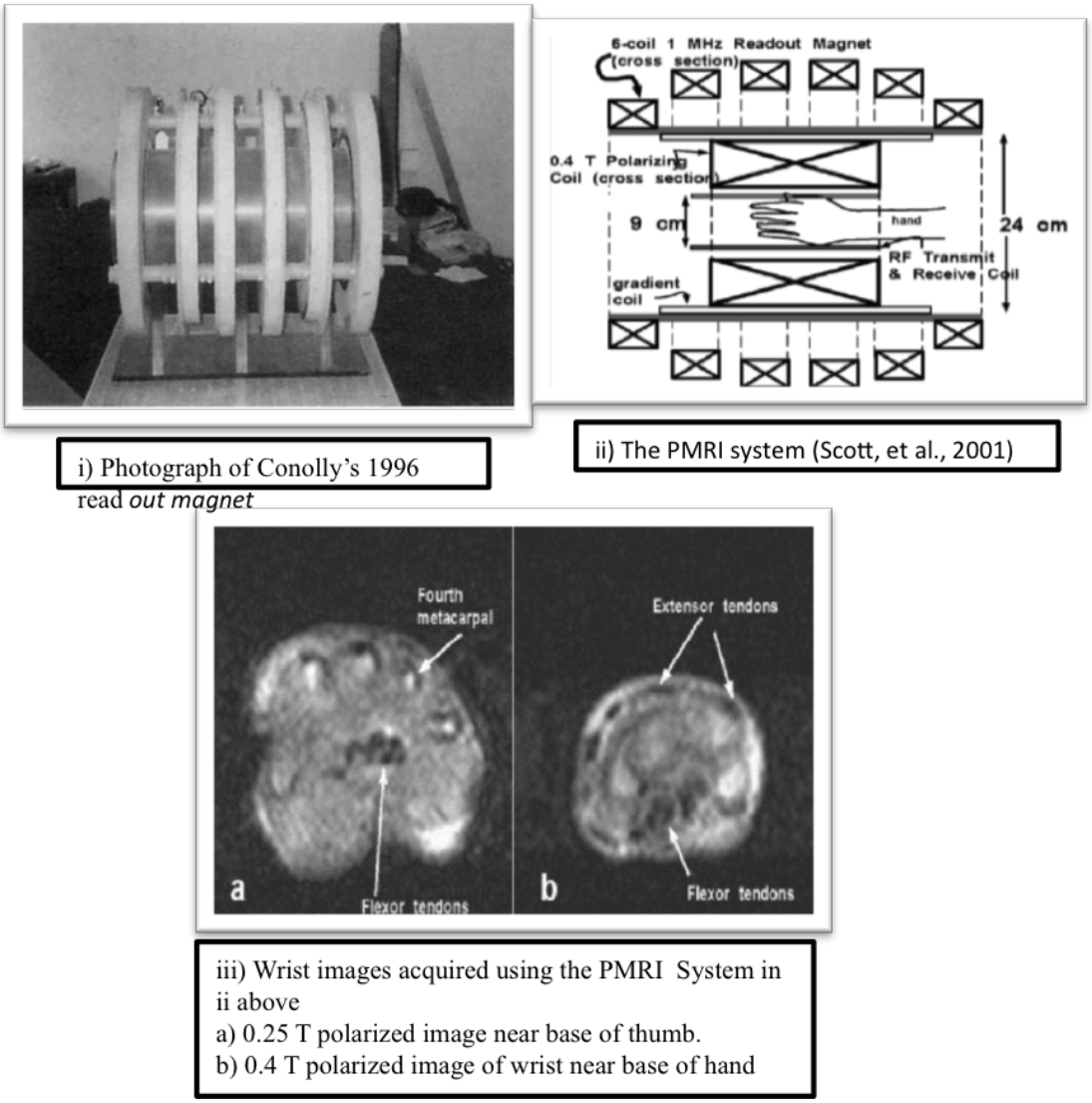


Figure 2.1. Pre-polarized MRI [41]

tively stronger magnetic field of 27 mT, this group was later able to acquire better images of the wrist (2.2) [43]. The remarkable improvement in the PMRI systems was focused mostly at imaging of extremities. Clinical application would require that this system is improved to a level where brain imaging is possible.

The niche for low field MRI relies on being able to provide diagnostic imaging of brain diseases at costs which are much lower than those of conventional MRI.

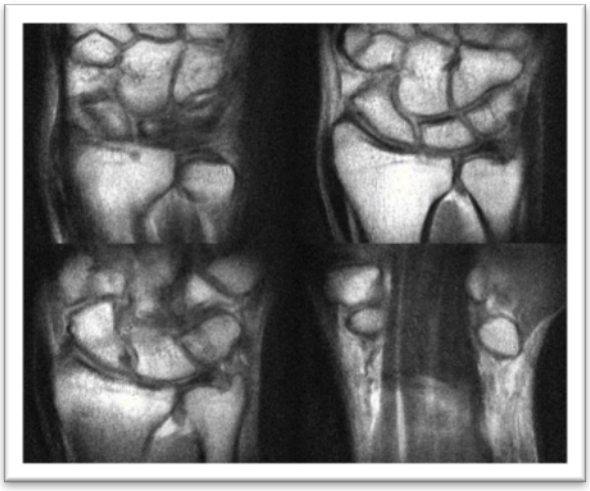


Figure 2.2. PMRI images of the human wrist [43]

No protracted attempts have been made to integrate such a system into clinical practice. This is partly because the resolutions needed to diagnose tumors of the brain are still much higher than could be achieved with this resistive coil based technology. The other huddle is the need for very sensitive room temperature sensors that could be used to detect the small signals generated by PMRI systems. Even though materials for PMRI systems may seem inexpensive, the engineering expertise needed to get these systems running is formidable.

Motivated by Conolly's group, some research centers have attempted to refine PMRI systems for possible medical application. One such research unit is at Los Alamos National Laboratory that has for some time been working on different aspects of PMRI system. [44].

2.1.1 Possible PRI detection technology

PMRI technology has evolved over the years and there is hope that once engineering aspects of the technology are optimized to enable clinical applications, industrial manufacturing of such systems could considerably drive the total cost down to

tens of thousands of dollars. One of the major hurdles of PMRI is that the main magnetic field may not be increased beyond 0.1 T without considerable increase in the weight and current injected into the coils. Cooling the system under such circumstances may considerably increase costs and obscure the intended benefits of PMRI technology. Keeping the magnetic field strengths to practical limits implies working with small signals and this calls for very sensitive magnetic sensors to detect and resolve such signals. Exploring possibilities of more sensitive magnetic sensors continues to be an active field of research. Realization of such sensitive detection technologies is pivotal in driving PMRI technology towards its intended application.

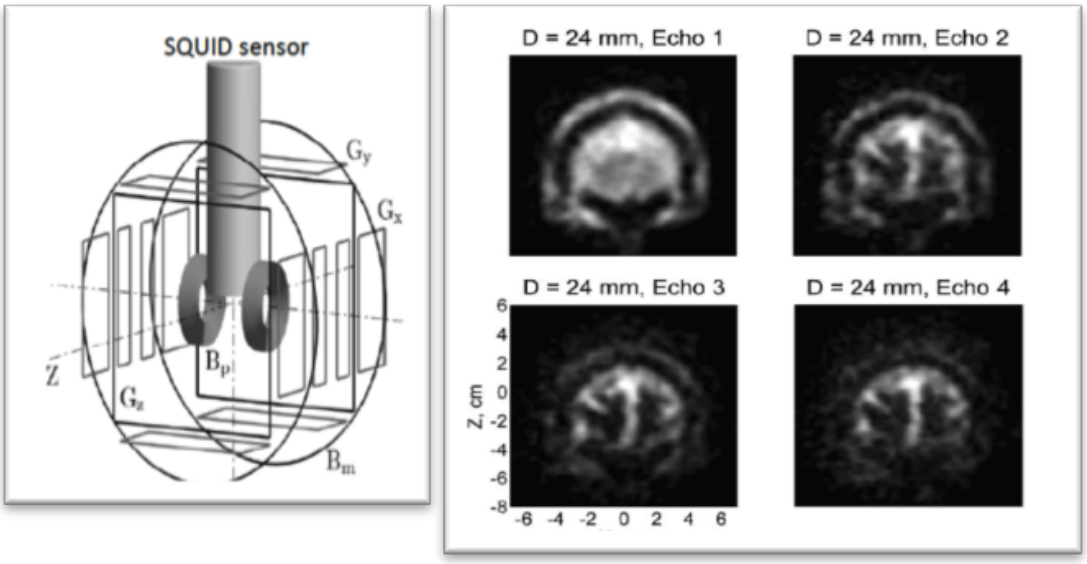


Figure 2.3. Sketch of PRI system showing SQUID sensor (left), and images of the brain acquired at 46uT using SQUID sensors (right) [45]

To investigate such applications, in 2008 Zetov et al. employed superconducting quantum interference device (SQUID) as sensors in PMRI systems to demonstrate the feasibility of brain imaging [45]. This resulted in a remarkable demonstration of brain imaging using PMRI as the acquired images showed considerable contrast

between brain matter and fluids within the brain (Figure 2.3). Their research showed that even at very low magnetic fields of 46 μT, there is enough signal to reconstruct brain image if sensitive detectors are used to pick up and resolve the signal (Figure 2.3).

Although SQUIDS are sensitive magnetic sensors which can pick up signals as low as $10^{-14}T$, they are a cryogenic technology and use superconductors that are very expensive to procure, operate and maintain. The goal of PMRI is to have a clinically diagnostic system at low capital and operational costs, which is the main purpose of this project. Using low cost PMRI systems together with expensive SQUIDs technology defeats the purpose of this project. More suitable inexpensive sensors would therefore be ideal for PMRI applications.

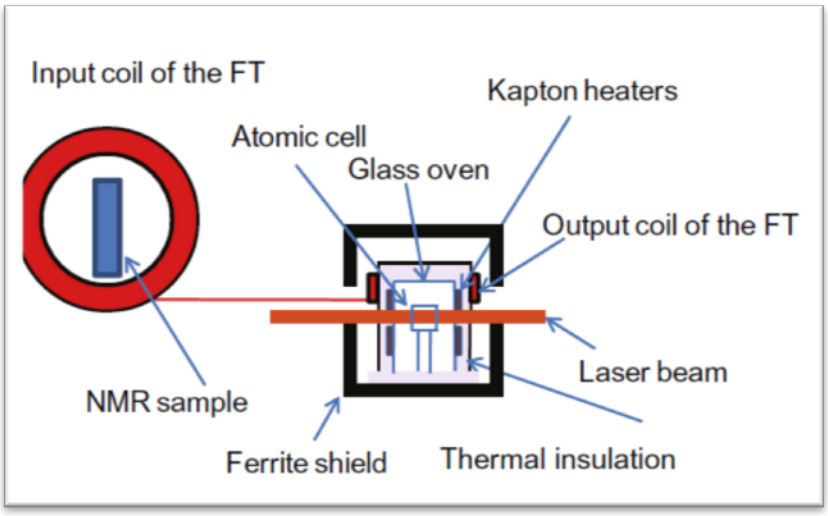


Figure 2.4. The detection system based on the flux transformer and the atomic magnetometer [46].

Atomic magnetometer (AM) is one type of sensor that is relatively inexpensive compared to SQUIDs, but with sensitivity comparable to that of SQUIDS. Development of AM sensors has progressed over the years with their main biological application being measurements of magneto encephalographic (MEG) signals [47]

[48]. The feasibility of NMR detection using AM was first demonstrated in 2005 by Savukov et al [49]. One of the downsides of AM is that it is sensitive to both the static magnetic field Bo, and gradient magnetic fields. During signal detection in MRI, there are at least two magnetic fields present and using AM would distort the resulting signal. Separation of magnetic fields is therefore key if AM are to be used for PMRI signal detection. This problem was investigated and partly addressed by a group at Los Alamos National Laboratory led by Savukov who developed PMRI based on atomic magnetometry [46].

The problem of sensitivity of atomic magnetometer (AM) to unwanted magnetic fields was solved by combining the AM with a flux transformer (FT). This combination of AM+FT works on the principle that the sample to be imaged is placed inside the input coil of the FT, both of which are inserted into the PMRI system. The output coil of the PMRI is then placed on a ferrite surface shielding the AM cell (Figure 2.4). Time varying magnetic fields generated by the sample induce a voltage in the input coil of the FT, which in turn drives a current through the output coil of the FT. The current through the output coil generates a magnetic field which is picked up by the AM. This kind of arrangement therefore enables the AM to be placed relatively far from the PMRI system thus eliminating the problem of susceptibility to various magnetic fields. To validate the practicality of the AM arrangement, images were acquired using both AM and SQUIDS for comparison.

Image quality of the AM+FT combination was found to be comparable to that of SQUIDs. Knowing that the sensitivity of AM sensors at this point depended on the noise generated by the FT coils, the field enhancement coefficient and the bandwidth of the AM, improvements in these parameters will greatly increase the applicability of AMs in the near future. One other downside of AM is that the

atomic cell operates at high temperatures of up to 200^o C and it needs a shielded environment which may turn out to be very expensive. This hurdle is however being overcome as Liu et al. has recently detected NMR signals with AM operating at 40^o C [50]. With their modified AM, they were able to detect NMR from a 125 μL water sample at field strength of 47 nT.

Alternatively, PMRI could also benefit from the development of chip-based magnetic sensors based on micro-electromechanical systems (MEMS). There are different types of MEMS sensors but some of the common ones rely on the arrangement of micro-arrays of permanent magnets overlaid on complementary metal oxide semiconductors (CMOS). When interacting with external magnetic fields, these magnet arrays can generate magnetic flux capable of moving cantilevers using the Lorentz force principle. The moving cantilevers are then able to generate electrical signals that can be detected. Efforts are geared towards increasing the sensitivity of these systems through better fabrication methods [51]. Although not yet in the femto-Tesla range, sensitivity of MEMS devices is rapidly improving, with some reporting pico-Tesla detection [52]. With such improvements in sensor technology, transformation of MEMS technology into PMRI applications is possible.

2.1.2 PMRI Switching circuits

Apart from small realizable signals from PMRI requiring sensitive detection technologies, the other problem plaguing PMRI is the interaction between the pulsating magnetic field B_p and the rest of the system such as the B_m and gradient coils. As a reminder, B_p is used to pre-polarize nuclei spins but is switched off before the image is acquired. However, due to mutual inductance created by B_p, image acquisition cannot be done immediately as there are residual magnetic fields because

of this switching. The excitation RF pulse has therefore to be applied after some delay time has passed. Waiting for the effects of mutual inductance to disappear means that the advantage of the pre-polarizing B_p is greatly eroded as the spins will quickly loose spin coherence previously achieved.

Using switching technologies that will improve on the ramp-up and ramp-down times of the Bp magnetic field can mitigate this problem. In one of their papers, Matter et al. [39] designed a Bp switch based on energy exchange between the electromagnet coils and capacitors. To be able to rapidly switch between magnetization levels, the magnet coils need very rapid supply of boost currents and these can be provided by capacitors which rapidly store and discharge energy to provide such current sources and sinks [39]. In their model, they showed that by adding a capacitor in series with the magnet coil, the ramp-up and ramp-down times, t_{ru} and t_{rd} respectively, can be determined as

$$t_{ru} \approx t_{rd} = \frac{1}{2\pi}\sqrt{LC} \tag{2.1}$$

where L is the inductance of the coil and C is the value of the capacitor to be included in the circuit. However as coils become large to accommodate adult heads and the number of turns become many, the value of L dramatically increases making it hard to get suitably smaller capacitors capable of storing high energies. The ramp-up and ramp-down times will considerably increase.

2.2 Static electromagnet MRI systems

Because of all the technical and geometry difficulties associated with the PMRI system, another thought in the ultra-low field MRI technology research is to remove

the pre-polarizing field and have systems which operate on only static uniform fields. This would have an advantage of eliminating the effects of mutual inductance associated with the pulsating magnetic field. Such systems were used in the discovery phase of MRI technology before the advent of super conductors [53]. Lother et al. recently designed an ultra low field MRI system that uses only the static magnetic field [54]. The system consisted of a pair of Helmholtz coils to provide the static B_o magnetic field. Field homogeneity was enhanced by addition of shimming coils at same locations as the Helmholtz coils but with varying diameters and number of turns (Figure 2.5).

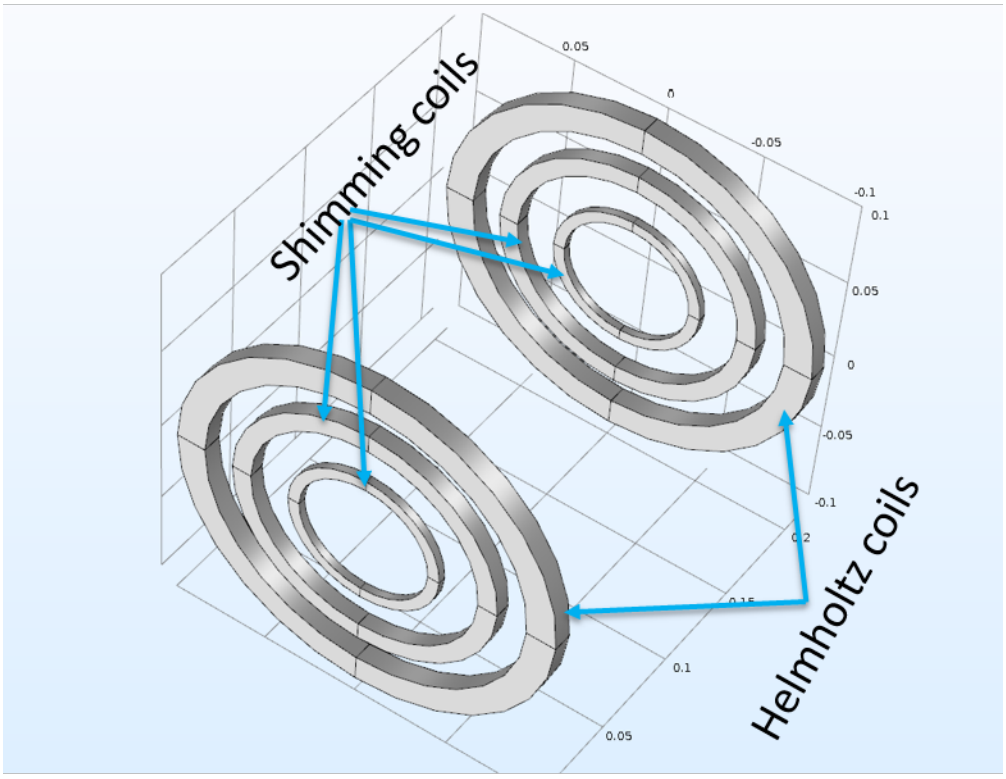


Figure 2.5. Illustration showing the Helmholtz design of the low field MRI system. Adapted from [54]

This system was designed for a bore size of 10 cm and a magnetic field strength of 23 mT. Since there is no pulsating magnetic field, it is possible to use iron and

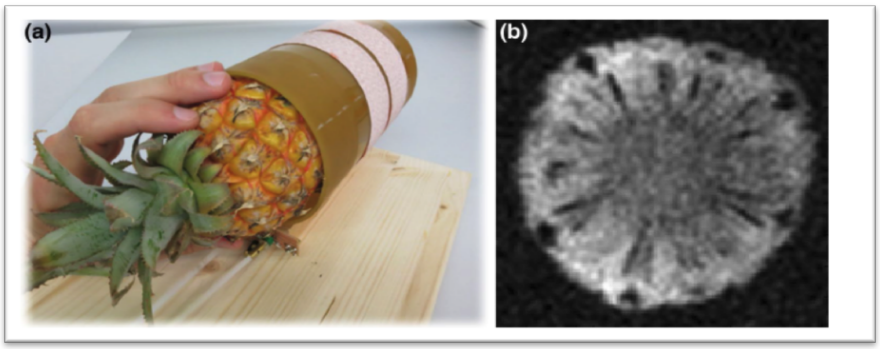


Figure 2.6. a) Shows the insertion of of the pineapple into the RF solenoid coil used as both transmitter and receiver in preparation for imaging. The coil is 10 cm in diameter. b) 2D spin-echo image of the pineapple with 5 mm slice thickness [54].

other high permeability materials to shield the system from stray magnetic fields. Imaging times can also be markedly reduced since there is no need to wait for the mutual inductance to fade out. An image of a pineapple was acquired using this system and had very good contrast and in-plane resolution of 1.6 mm x 1.6 mm (Figure 2.6). This type of design also makes it possible to use solenoid coils as RF coils which is not possible in PMRI systems because of the orientation of the pre-pulse magnet coil.

A similar ultra-low field MRI system without the pulsating magnetic field was constructed by a group at the Martinos center for medical imaging in Massachusetts USA [55]. They too used Helmholtz coil pair to generate a uniform static magnetic field. The volume of homogeneous magnetic fields in Helmholtz coils is relatively small compared to the Lee-Whiting four coil system. To have a large volume of magnetic field homogeneity, the diameter of the Helmholtz design has to be considerably large. Therefore to accommodate a human head, the system at the Martinos Center consisted of a pair of Helmholtz coils, 2 m in diameter, generating a uniform magnetic field of 6.5 mT. Again, with such a system imaging times can

be relatively faster as this group was able to acquire brain images in 6 minutes with maximum SNR of 21 and resolution of up to 2.5 mm x 3.5 mm x 8.5 mm [55].

In summary, the contrast provided by low field MRI systems is still low but the resolution has clearly reached a level where clinical application can be possible. Most of the systems designed thus far have small bores. Increasing the bore size of these low field systems to accommodate an adult head would constitute a brilliant step in the ultra-low field MRI technology.

Chapter 3

DESCRIPTION OF THE PMRI SYSTEM

3.1 Basic electronic components of PMRI

The description of PMRI hardware in chapter two considered mainly coils. In this chapter we describe the supporting hardware and electronic components that are necessary for the construction of the pre-pulse ultra-low field MRI. Our design is adapted from the PMRI system constructed by Savukov et al [56] with the overall aim of enlarging the bore size to accommodate an infant hydrocephalic head. The block diagram of the system is shown in figure 3.1 below.

A simple PMRI system consists of the read-out field (B_o - also referred to as Bm) coil, the pre-pulse field (B_p) coil, gradient coils, radio frequency transmitter coil and radio frequency receiver coil. The electronic components comprise filters, amplifiers, switches, power supplies, rectifiers and frequency mixers. The block diagram in figure 3.1 shows the flow of signal and power between different components. It provides an understanding of a fully functional PMRI system and

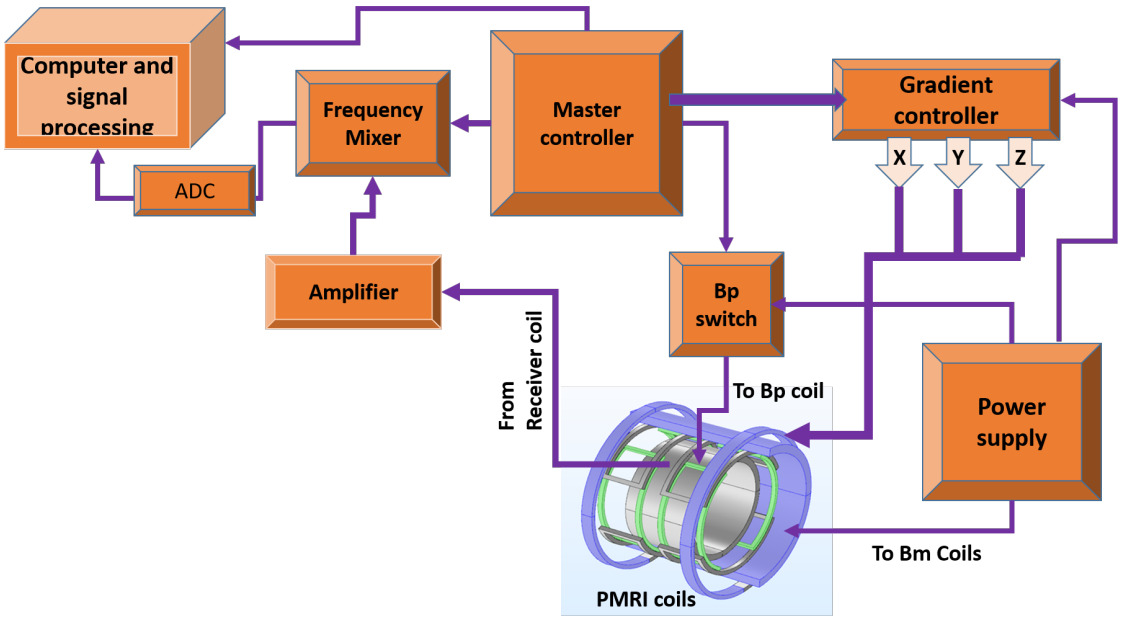


Figure 3.1. Block diagram of the PMRI system

how its modular architecture could be replicated and/or modified to suit specific applications in developing countries. Most of the components shown were built by hand and the accompanying analysis is aimed at showing that commercial systems could be sought to replace these modular systems with the potential of making the PMRI system inexpensive, safe and easy to assemble and maintain. The components include:

3.2 The Bp switch

The Bp magnetic field is pulsed at frequencies normally less than one Hertz. The ideal waveform for the Bp magnetic field would be a square wave, where the ramp-up and ramp-down times are negligible. High speed switches are used for this purpose. In this case we used the 100 VDC/100 A solid state switch by VSholdings [57].

This high speed solid state switch has a rise time delay of 320 nS and a turn-off delay time of 820 nS to switch between zero and 100 A. The frequency of the B_P switch is part of the pulse sequence of the PMRI system and impacts on the imaging time. Longer pulses result in longer acquisition times but improves the signal to noise ratio.

3.3 Gradient amplifiers

MRI gradient coils are designed to generate linearly varying, position dependent magnetic fields. However, power to the gradient coils is supplied by the control system (master controller in figure 3.1) which typically generates very small voltages and currents. These currents need to be amplified in order to generate gradient magnetic fields required to spatially resolve the MR signal.

The amplification is provided by gradient amplifiers. Conventional MRI gradient amplifiers can be expensive. Our system uses amplifiers constructed using operational amplifiers (OP-Amps). OP-Amps are high gain amplifiers that use a ratio of input and output resistances, and feedback control to boost the input voltage, current or power supplied to them in order to give high outputs. For a simple amplifier, the gain is a ratio of the output or reference resistor to the input resistor as shown in figure 3.2.

It should be noted that the stability of amplifier gain depends of the frequency of input and output signals. The amplifier will respond linearly within a range of frequencies beyond which the amplifier gain will significantly reduce and its response no longer deterministic. Therefore other circuit components such as extra resistors and filter capacitors are normally added onto the design to get the desired amplifier response.

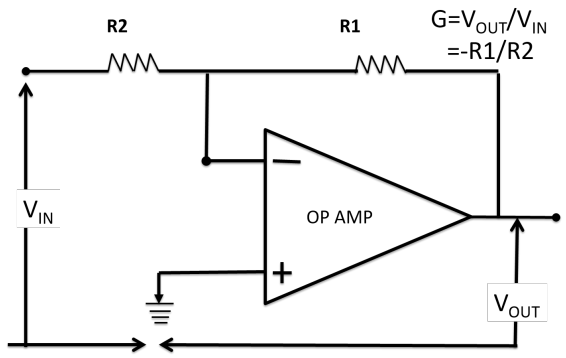


Figure 3.2. Inverting operational amplifier.

3.4 The Power supplies

Generation of specific strength of magnetic fields require precisely controlled currents to be injected into electromagnet coils. The B_P coil, B_m and gradient coils are therefore supplied by different dedicated power supplies to achieve the level of control and specificity required of each magnetic field. Our Bm coil in particular is supplied by Xantrex XDL 35-5T DC power supply now supplied by AMETEK programmable power supplies (www.ametek.com). It has capacity to supply 6 A at 30 V and can automatically adjust its voltage level to keep a steady output current output to within 1 mA. The Bp coil is supplied by magna power supply model SL100-15/UI (www.magna-power.com) capable of delivering 15 A at 100 V. Power to the gradient amplifiers comes form the Keithley 2231A-30-3 power DC power supply provided by Tektronik (www.tek.com).

3.5 The resonant circuits

Resonant circuits are needed in MRI to generate and detect radio frequency fields. For the PMRI system, the main resonant circuit is the one involving the signal transmitter and receiver coils. The coil is connected in parallel with a tuning

capacitor (Figure 3.3). The coil has an intrinsic inductance, L and resistance, R. The total impedance of the circuit is the sum of the resistance, inductive reactance, X_L given by $X_L = j\omega L$ and capacitive reactance, X_C given by $X_C = -j/\omega C$. At resonance, $X_L = X_C$ giving a resonant frequency of $f = \frac{1}{2\pi\sqrt{LC}}$.

However, in signal transmission, the impedance of the signal source should be matched with the signal load to avoid signal loss due to reflections as a result of impedance miss match [58]. The resonant coils made using copper wires usually have very low resistances and they are connected through an amplifier with an output resistance of 50 Ω. An additional matching resister is therefore added to match the impedance of the amplifier.

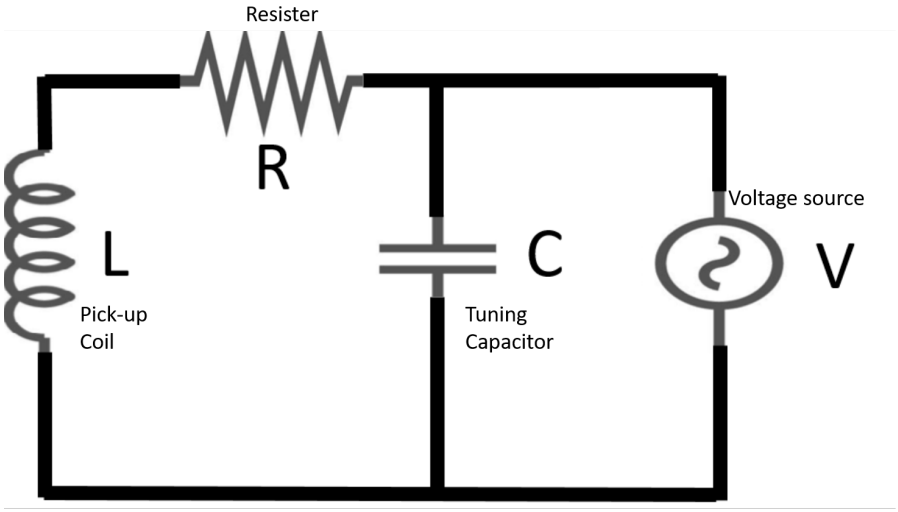


Figure 3.3. RLC Resonant circuit.

3.6 Frequency filters

As the name suggests, filters are responsible for allowing only signals within a certain range of frequencies, normally referred to as the bandwidth. Passive filters which are a combination of resistors, capacitors and inductors are used to reduce

dependency on external power supplies as is the case with active filters. Filters work by altering the amplitude and/or phase of the output signal in relation to the input signal. The amplitude and phase of signals outside the allowable frequency range is distorted or attenuated to the extent that those frequencies are not detectable at the output of the filter [59]. Filters have gain which is dependent on signal frequency such that the output of a filter, also called the transfer function, and is given by

$$|H| = \frac{|V_{OUT}(j\omega)|}{|V_{IN}(j\omega)|}. \tag{3.1}$$

There are several types of filters including low pass filter, high pass filter, notch filter and band pass filter. A band pass filter is more commonly used in our system and it is a combination of low pass and high pass filters (Figure 3.4).

The cut off frequency of a filter is taken to be the point where the signal amplitude falls below 3 dB and for a simple low pass filter, that point is given as

$$f_{CL} = \frac{1}{2\pi R1C1}. \tag{3.2}$$

Similarly for high pass filter, the cut-off frequency is given as

$$f_{CH} = \frac{1}{2\pi R2C2}. \tag{3.3}$$

The band pass frequency range as a result of cascading the low and high pass filters is therefore given as $f_{CH} - f_{CL}$ Circuit elements are chosen as to satisfy the required frequency range. Filters used in our systems are designed with low cut-off frequency of 80 kHz and high cut-off frequency of 300 kHz.

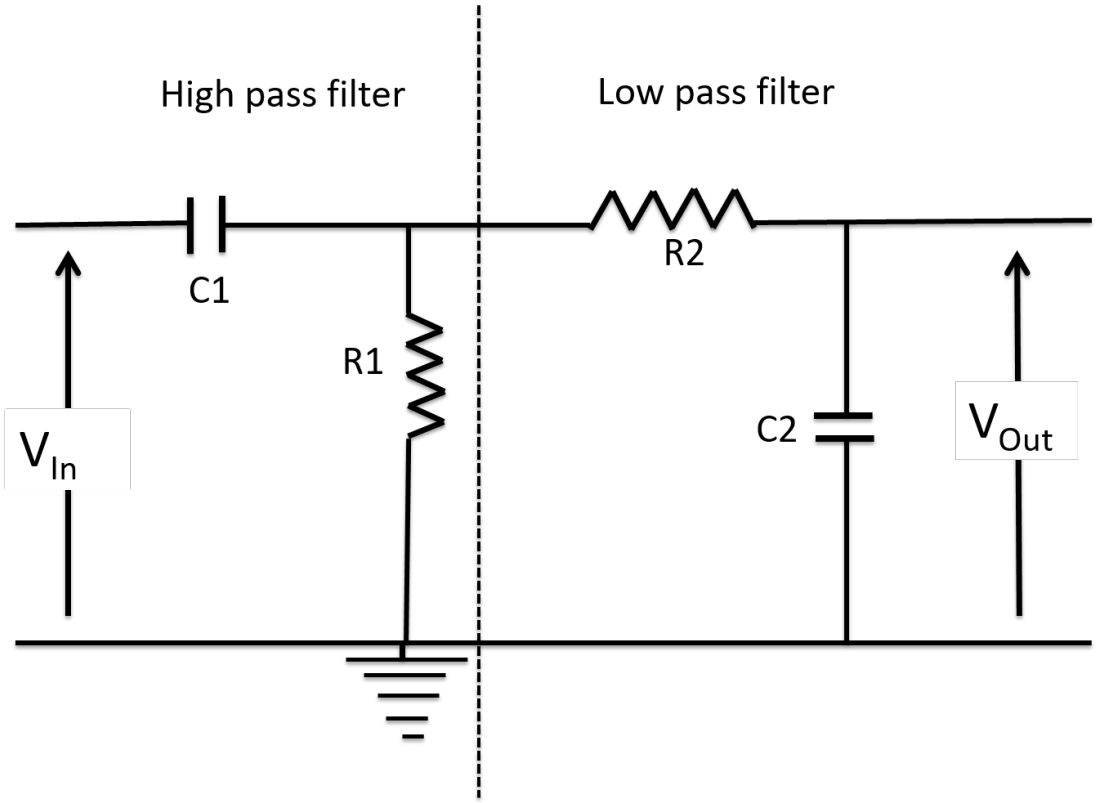


Figure 3.4. Band-pass filter.

3.7 The frequency mixer

RF signals from the MRI are at high frequencies which are relatively difficult to sample. The theory of heterodyne receivers, invented by Reginald Fessenden in 1901 [60] is used to generate new frequencies which can easily be sampled. The heterodyne principle allows two or more frequencies to be mixed to generate new frequencies. A simple frequency mixer is designed with two input terminals, one for the high frequency MRI signal and the other for a locally generated signal from the data acquisition and processing system (master controller). The output of the frequency mixer is the difference between the two input frequencies (Figure 3.5 [61])

The PMRI system that we developed can operate at frequencies ranging from

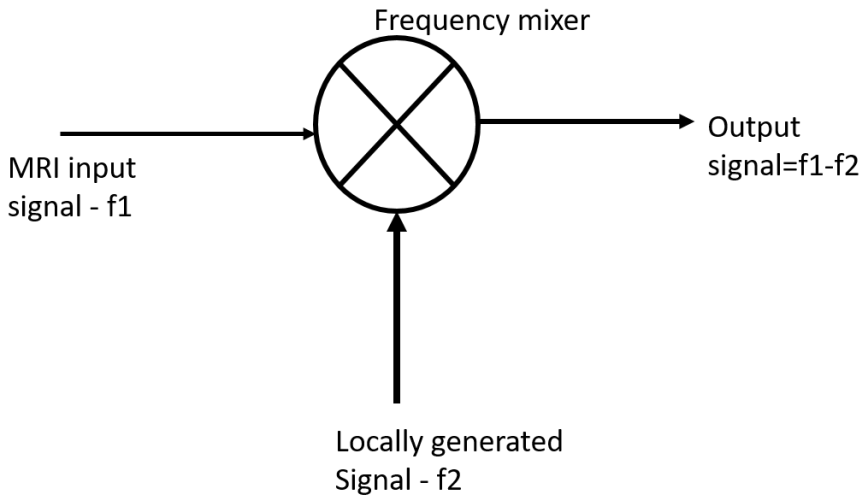


Figure 3.5. An illustration of frequency mixer showing input and output signals. Signal amplitude is not a matter of concern here

80 kHz to 500 kHz. These are relatively high frequencies to sample. To avoid aliasing, signal sampling should be done at frequencies which are at least twice the signal frequencies [62]. However, by using a frequency mixer, a local signal is generated with a frequency that is close to the signal frequency such that the difference between the two frequencies is small enough to allow for sampling at frequencies much lower than the actual signal frequency.

3.8 Signal acquisition and processing

Signal acquisition and processing is done by a LabView program adapted from Igor I Savukov from Los Alamos National Laboratory. The control program uses the NI BNC2110 connector block provided by national instruments (www.ni.com). This is connected to the data acquisition and control boards using a general purpose interface bus (GPIB) cable. The control signals generated from the board include the timing signals for the Bp power supply, gradient amplifiers, and RF magnetic

field. The signal to be processed is detected by the receiver coil, amplified by the signal pre-amplifier provided by Stanford Research Systems model SR 560 (www.thinksrs.com), mixed through a frequency mixer before it is converted into a digital signal using the analog to digital converter (ADC). Processing of the signal is done by digital sampling and using Fourier transforms to form an image.

Chapter 4

DESIGN CONSIDERATIONS AND FABRICATION OF THE PMRI SYSTEM

The aim of this project is to build an MRI system which is inexpensive, portable, non-cryogenic, easy to use and maintain, and has low power requirements yet big enough to accommodate an adult human head. These requirements are not easy to achieve.

The portability of an MRI system is determined mostly by the strength of the B_o magnetic field, the bore geometry and size. The magnetic field of circularly shaped coils scales up with the number of turns and the amount of current flowing through the coil. The magnetic field is also inversely proportional to the radius of the coil as can be deduced from equation 1.5 [21].

The design of MRI has to consider first the purpose of the device. If the purpose is to be able to image an infant hydro-cephalic head, as is in this case, dimensions that would meet this purpose should then be determined before anything else. The

first parameter to be determined here therefore is the bore size of the magnet. The World Health Organization charts show that average head diameter of a five year old infant is approximately 17.2 cm [63]. However, we are designing this PMRI system for hydrocephalic children whose heads are bigger than a normal child's head. Our system is therefore designed with a usable bore of 22 cm, which is big enough to accommodate an adult human head [64]. The Bm coil was designed with a diameter of 45 cm to also allow for insertion of Bp and RF coils.

After determination of the bore size, the tendency is to have as high a magnetic field as possible since higher magnetic fields translate into better SNR and subsequently better image quality [65]. But like we said earlier, this is limited by the number of turns we are willing to have, and consequently the power requirement. The power P dissipated by a coil of resistance R, carrying current I is given by

$$P = I^2 R \tag{4.1}$$

For example if one has a power limitation of 500 W at 10 A, from equation 4.1, the resistance of the coil is limited to 5 Ω. This essentially limits the coil length and the number of turns, as resistance increases with length.

Another important factor that we considered is the ease with which the system could be maintained in a developing country. The technical expertise required to maintain, service and repair an MRI system is enormous and in most cases, lacking in developing countries [66]. Constructing an overly complex system would therefore not meet the purpose of the project. To keep the device technically simple, most of the components of our PMRI system were hand made using discrete electronic components. By constructing the system by hand, we demonstrate feasibility and scalability of the PMRI system in the developing world.

The cost of the system is not to be forgotten. Cost is arguably the most important factor driving the move towards lower field strength MRI systems [2]. High field MRI systems can cost millions of dollars. Apart from the capital costs, operational costs of conventional MRI systems include power requirements, service and maintenance costs, all of which are in hundreds of thousands of dollars per year [2]. These costs and other restrictions make MRI unsustainable in the developing world. As a result there is increased use of computed tomography for brain imaging [67], whose costs is between $200,000 to $300,000. For low field MRI technology to be attractive for low income countries, it should be less expensive than the CT units currently in use. Our aim is to construct a system that is less than $100000.

4.1 Design of the B_m coil

In MRI, homogeneity of the main magnetic field is an important factor that has to be taken into consideration while designing coils. Inhomogeneities in the magnetic field introduce artifacts that degrade the quality of the resulting imaging. A number of coil designs including the Merrit three, four and five coil systems [68], the Rubens five coil system [69], Helmholtz and Lee-Whiting coil systems [70] among others have been proposed to improve field homogeneity. Of these coil systems, the Lee-Whiting four coil system produces an acceptable field uniformity and is easy to construct [71] thus our choice.

From Biot-Savart law, the magnetic field generated by a circular loop of coil can be approximated by an integral of the elemental current over the entire loop through which the current flows. This is given as

$$B\vec{(r)} = \frac{\mu_o}{4\pi} \oint \frac{I\vec{dl}X\vec{r}}{\vec{r^3}}. \tag{4.2}$$

where I is the current flowing through the conductor, dl is the elemental length of the conductor and r is the radius of the loop formed by the conductor.

Integrating equation 4.2 from 0 to 2π for a field along the Z axis of a cylindrical system of radius a, as shown in figure 4.1 gives

$$B_z = \frac{\mu_o n I a^2}{2r^3}. \tag{4.3}$$

where $r^2 = a^2 + z^2$ and n is the number of turns.

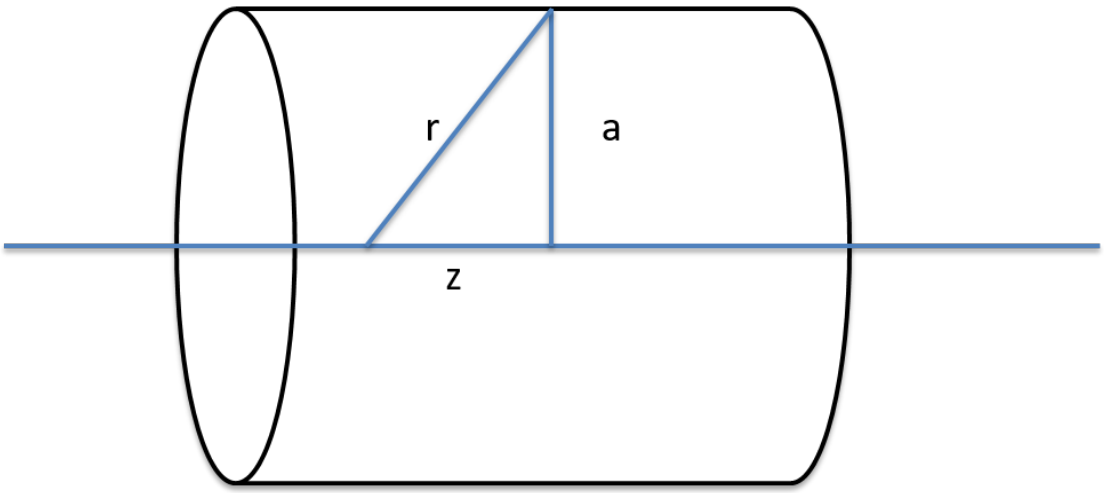


Figure 4.1. Geometry explaining relationship between radius a and distance along the z-axis in the Biot Savart integration

The Lee-Whiting MRI magnet coil system is composed of two sets of circular coils (two outer coils and two inner coils) located $\pm 0.1216D1$ and $\pm 0.4704D1$ respectively from the center of the system (figure 4.2), where $D1$ is the effective diameter of the cylindrical core on which the circular coils are wound.

To obtain a uniform magnetic field, the ratio of the number of turns on the outer coils to inner coils should be 9 : 4. This means that for every 9 turns on each of the the outer coils, there should be 4 turns on each of the inner coils. For simplicity, we will refer to one turns ratio as 9 : 4 : 4 : 9.

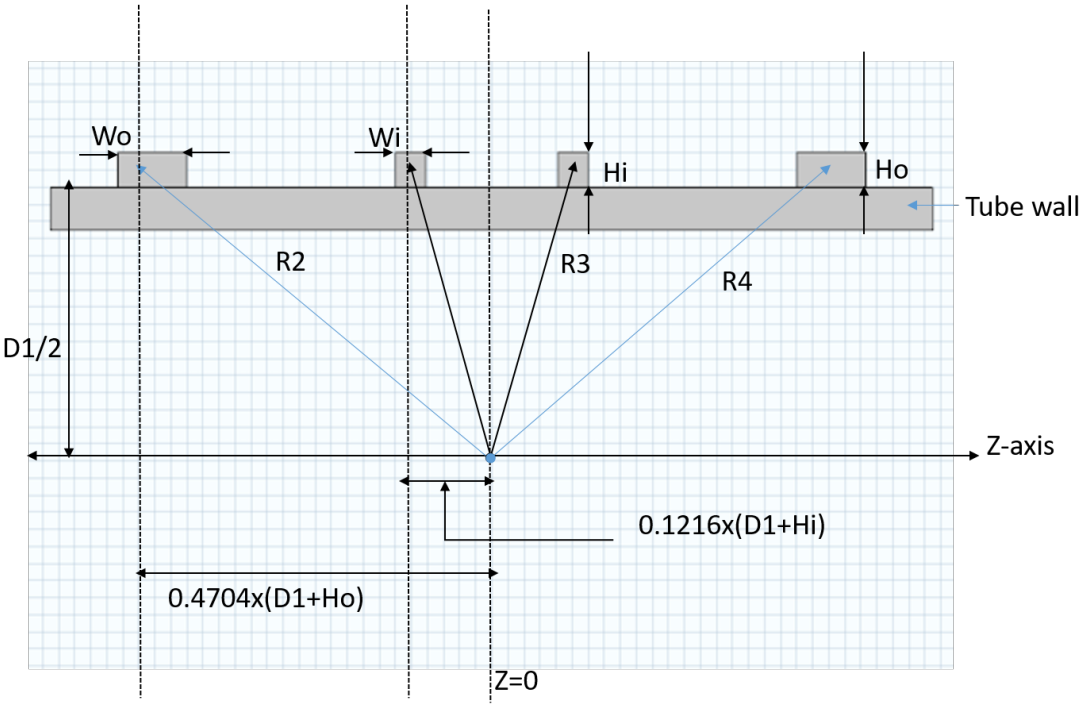


Figure 4.2. 2D view of the Lee-Whiting coil system showing the coil cross sectional areas and coil location

.

From equation 4.3, the magnetic field for one turns ratio can be given by

$$B_z = \frac{9\mu_o nIa^2}{2R_1^3} + \frac{4\mu_o nIa^2}{2R_2^3} + \frac{4\mu_o nIa^2}{2R_3^3} + \frac{9\mu_o nIa^2}{2R_4^3} \tag{4.4}$$

Due to symmetry of the system, $R_1 = R_3$ and $R_2 = R_4$, equation 4.4 becomes

$$B_z = \mu_o Ia^2(\frac{9}{R_1^3} + \frac{4}{R_2^3}) \tag{4.5}$$

where a is the effective radius of the cylindrical core (in this case a=D1/2).

Substituting for values of $R_1^2 = (D1/2)^2 + (0.1216D1)^2$, $R_2^2 = (D1/2)^2 + (0.4704D1)^2$, and $I = 1A$, the magnetic field at the center of the Lee-Whiting coil system can be given as

$$B_z = \frac{17.96}{D1}\mu T. \tag{4.6}$$

The relationship between the magnetic field and coil positioning along the z-axis as given in equation 4.5 and 4.6 do not take into consideration the height/thickness and width of the coils. Setting up the optimal dimensions for the coil cross-sectional area (Width x height) is very critical in construction of large bore ultra-low field MRI systems. Changing the coil height changes the effective diameter and therefore coil locations along the z-axis. This has an influence on the magnitude and uniformity of the magnetic field. To determine the optimal width to height relationship, we modified equation 4.5 to include changes in coil dimensions.

In the design and simulation procedure, the following restrictions and assumptions were made:

1) Power requirement: Power is one of the most important requirements to consider when designing a sustainable system for the low and middle income countries. Due to limited power availability, a number of African countries are adopting the use of stand alone solar systems to operate some critical units in hospitals. Most of these solar systems are capable of running low-energy fridges rated below 500 Watts [72]. Designing a system capable of operating on solar power is therefore very ideal for such settings. As such, we limited the power requirement of the Bm coil to 500 Watts with a maximum current of 10 Amperes.

2) Wire size and length: Given the power requirement, wire selection becomes the next parameter to determine. To supply 500 W at 10 A, 50 V is required. For a 50 V source to be able to drive 10 A through a conductor, the resistance of that conductor should not be more than 5 Ω.

The resistance R of a conductor can be approximated by

$$R = \frac{\rho L}{A} \tag{4.7}$$

where ρ is the conductivity of the wire (6 x $10^7 S/m$ for copper), L is the length of the wire and A is its cross section area. Because of the current requirement, resistance, weight and availability, AWG 12 copper wire was selected as the conductor to be used for winding the coils. AWG 12 has a nominal diameter of 2.07 mm and a resistance of 2.315 x 10^{-3} Ω/m [73].

From equation 4.7, we calculate the length of the wire to be 940 meters.

3) Tube dimensions and number of turns

Having known the wire length, the next step is to determine the number of turns possible with this wire. This is determined in part by the tube dimensions on which the coil is to be wound. The diameter of the tube should be able to accommodate the Bp coil, the radio frequency coils and still leave a bore size capable of accommodating a hydrocephalic infant's head. The tube should also be rigid enough to hold the coils into position without deformation. For our purpose, we selected a tube with inside diameter of 45 cm and outside diameter of 47.5cm. Using the outer circumference and considering the 9:4:4:9 Ampere turns ratio for the Lee-Whiting coil system, we determined the total number of turns to be 630. However, we decided that 598 turns would be appropriate, taking into account that not all the wires will be in contact with the tube and therefore the average diameter will be greater than the outer diameter of the tube. 598 turns would result into 207 turns on each of the outer coils and 92 turns on each of the inner coils.

4) Determination of width-height relationship of the coils

To determine the optimal width-height ratio for the coil windings, the following

design parameters were defined (Table 4.3).

Parameter	Expression	Description
Dw	2.073[mm]	Nominal diameter of the AWG 12
N	23	Total Ampere turns ratio
n	1 to 92	Number of layers of wire on a coil
Hi	n*Dw	Height of the inner coils
Ho	Hi	Height of outer coils
Ni	92	Number of turns on the inner coils
No	207	Number of turns on the outer coils
Wi	Ni*Dw^2/Hi	Width of inner coils
Wo	(9/4)*Wi	Width of outer coils
D1	47.5[cm]	Outer diamter of the tube on which the coils are wound
Icoil	1[A]	Current flowing in the coils

Figure 4.3. Design parameters used for the simulation of the Bm coil system

Using the parameters defined in table 4.3, we write R1 and R2 as defined in figure 4.2 as

$$R1 = \sqrt{0.1216 * (D1 + Hi)^2 + (D1/2 + Hi/2)^2} \tag{4.8}$$

and

$$R2 = \sqrt{0.4704 * (D1 + Hi)^2 + (D1/2 + Hi/2)^2} \tag{4.9}$$

The magnetic field at the center of the coil is therefore given by

$$Bm = \mu_o N Icoil * (D1/2 + Hi/2)^2 * [4/R1^3 + 9/R2^3] \tag{4.10}$$

Heretwo conditions are considered for B: 1) The variation of Bm with Hi and Wi and 2) Variation of Bm with Ho and Wo. Two graphs are plotted for the two conditions (Figure 4.4)

From the graphs, we can choose to set the cross section area of the inner coils to be square (graph a) in which case the outer coils will be rectangular or we can

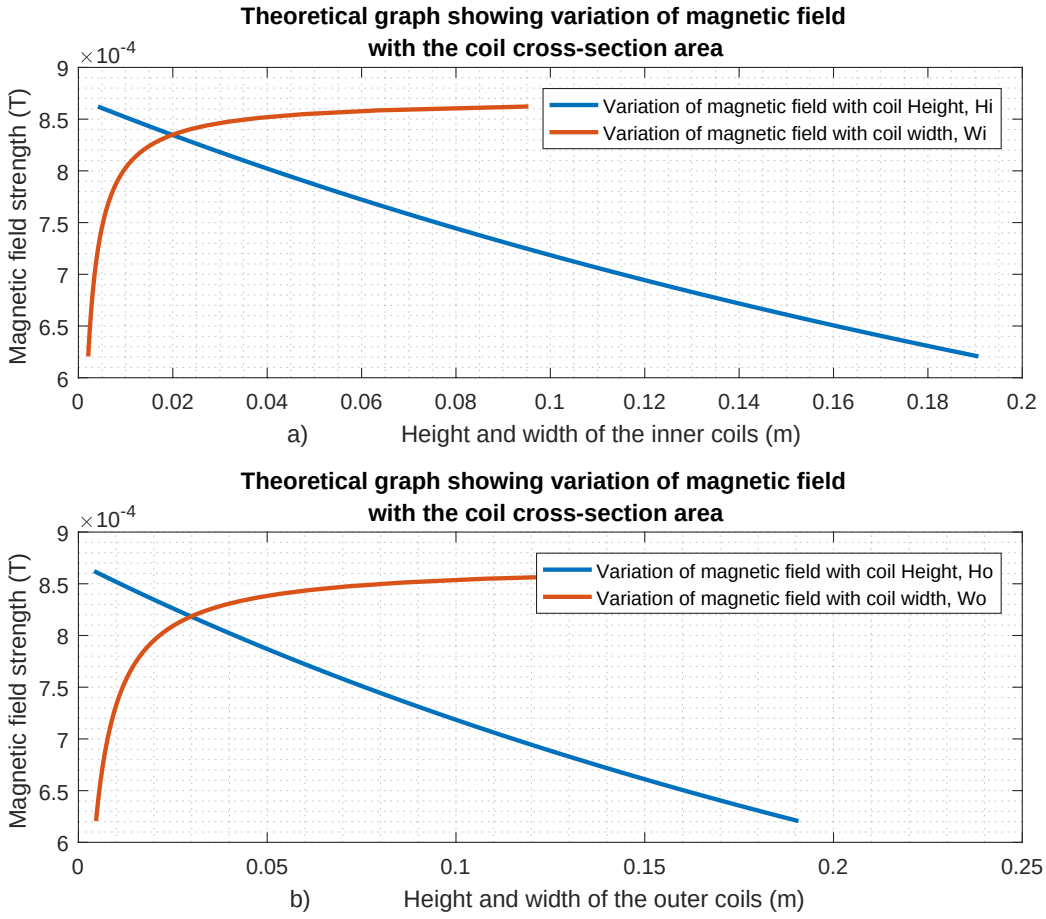


Figure 4.4. (a) shows the variation of the magnetic field at the center of the coil system with the width and height of the inner coils and b) shows the same variation with the width and height of the outer coils. The point of intersection of the graphs indicates a point where the cross section of the given coil is square and this is taken as the optimal dimensions

choose to make the outer coils square keeping the inner coils rectangular. We avoid making all the coils square because they have different number of turns and the system will have non-uniform radius.

Our main aim is to fabricate the Bm coil with a homogeneous magnetic field. To determine which of the two conditions in figure 4.4 above gives the most homogeneous magnetic field, we modeled the conditions using comsol multiphysics V5.2 (www.comsol.com).

4.1.1 COMSOL simulation of the Bm coil system

The COMSOL AC/DC magnetic fields, stationary study 3D model was used to simulate magnetic field strength and homogeneity of the four coil system following the procedure below:

a) Creating the geometry.

The 3D geometry of the system was created first by drawing the 2D section view and revolving it around the radius (Figure 4.5).

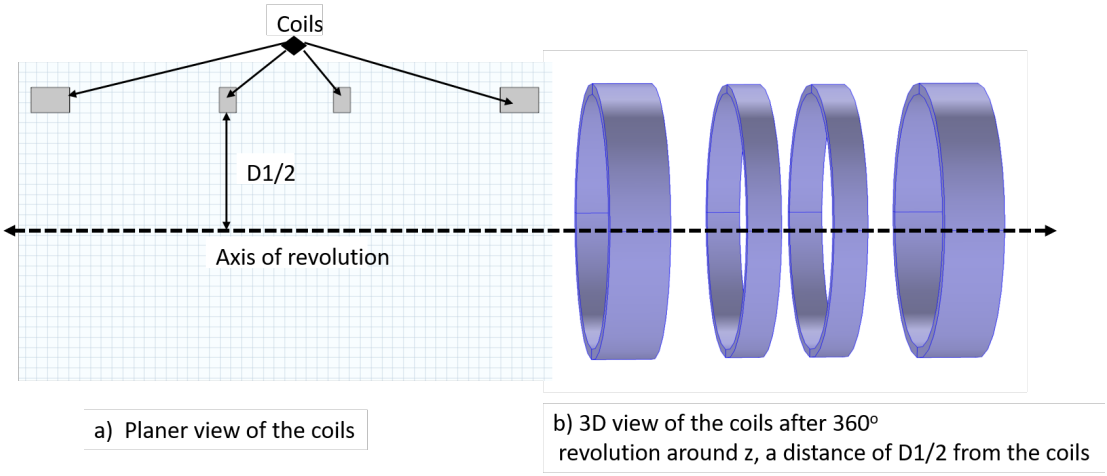


Figure 4.5. Comsol geometry set-up of the Bm coil system

Parameters for coil dimensions are specified in table 4.3. A solid sphere of diameter 65 cm was drawn around the model to define the boundary and computational limits in comsol.

b)Specifying the materials

Copper and air were used as materials for coil conductors and the sphere respectively. Default material properties as defined by comsol were used and these include conductivity for copper σ =6 x 10^7 Siemens (S)/m, and relative magnetic permeability $\mu_r = 1$. Air conductivity and magnetic permeability were defined as σ_{air} =0 S/m and μ_r=1 respectively.

c) Defining the physics.

The coils were defined as mutli-turn coils with 207 turns on the outer coils and 92 turns on the inner coils. The current through the coils was set at 1 A. To define the circular flow of current, the direction was chosen by selecting edges of each coil that form a circle. In our model, we changed the cross section area of the coils but the current density J as described by Apere's law (Equation4.11 in comsol is kept constant.

$$\nabla X H = J \tag{4.11}$$

where ∇ is the differential Hamiltonian operator, and H is the magnetic field intensity [74]. The current density J is also given by $J = \sigma E$, where σ is electrical conductivity of the material and E is the electric field.

In MRI, magnetic field is always defined in terms of the flux density B which is related to the field intensity through permeability as

$$B = \mu_o \mu_r H \tag{4.12}$$

and flux density is defined as the curl of the magnetic vector potential, A. We therefore calculate the magnetic flux density B as

$$B = \nabla X A \tag{4.13}$$

The surface of the sphere used as a boundary to limit the computational area is defined as a magnetic insulator by setting the magnetic vector potential normal to the surface as zero.

d) Running the simulation.

Three simulations were performed. First when the cross section are of the inner coils was square, then when the cross section of the outer coils was square and then assuming an infinitesimal coil. Results are shown in figure 4.6.

4.1.2 Simulation results and discussion

The simulation results seek to guide selection of the optimal coil cross section area for the given parameters of number of coil turns and wire diameter.

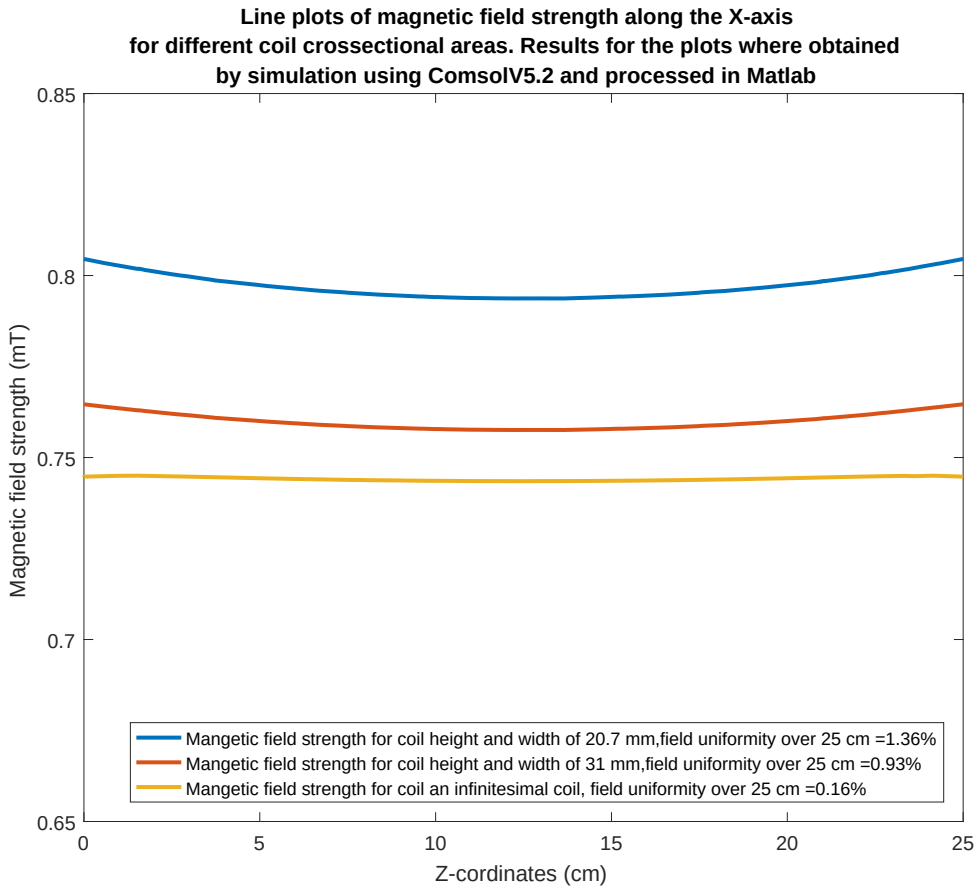


Figure 4.6. Magnetic field uniformity for different coil cross section areas

Analysis of results (Figure 4.6) show that the best magnetic field homogeneity is achieved with infinitesimal coils. However, realistically when the inner coils are

considered to be square, the peak-peak magnetic homogeneity over the region of interest is 1.36% and 0.93% when the outer coils are square.

Given the diameter of AWG 12 which was selected for coil winding and considering the number of turns, having square inner coils means having 9 layers of wire to form the height of the coil and 9 wires side by side to form the width of the coil. On the other hand the outer coils would have 9 layers and 23 wires side by side for the width and gives the highest magnetic field strength across the ROI. However, when the outer coils are made square, the inner coils would be 15 layers high and 6 wires side by side while the outer coils would have outer coils would be 15 layers high and 14 wires side by side for the width. The magnetic field strength is relatively lower. We chose to make the inner coils square partly for ease of winding and to maximize the magnetic field strength.

From these graphs, we see that there are two possibilities we can choose for our coil heights and widths. From (a), we deduce that the optimal height width relationship is when both the height and width are 0.02 m. This implies that the number of layers which make up the height of the coils should be 10. Therefore the width of the inner coils should be 0.02 m and the outer coils should be 0.043 m.

Similarly, graph (b) gives the optimal height width relationship to be 0.03 m for the heights of coils, 0.013 m for the widths of the inner coils and 0.03 m for the widths of the outer coils. However, choosing to make the outer coils square would considerably increase the effective diameter of the whole system. Considering that the gradient coils will have to be wound on top of the Bm coils, gradient coils would then need to have more turns to generate the required gradient strength and this would increase the power and switching requirements of gradient amplifiers.

4.2 Construction of gradient coils

Gradient coils are designed and constructed to generate magnetic fields that linearly vary in the three orthogonal directions x, y, z. The $Z - axis$ is taken to be along the axis of the cylindrical core, and the most efficient and easiest way of generating the Z gradient is by using a Maxwell coil pair (Figure 4.7).

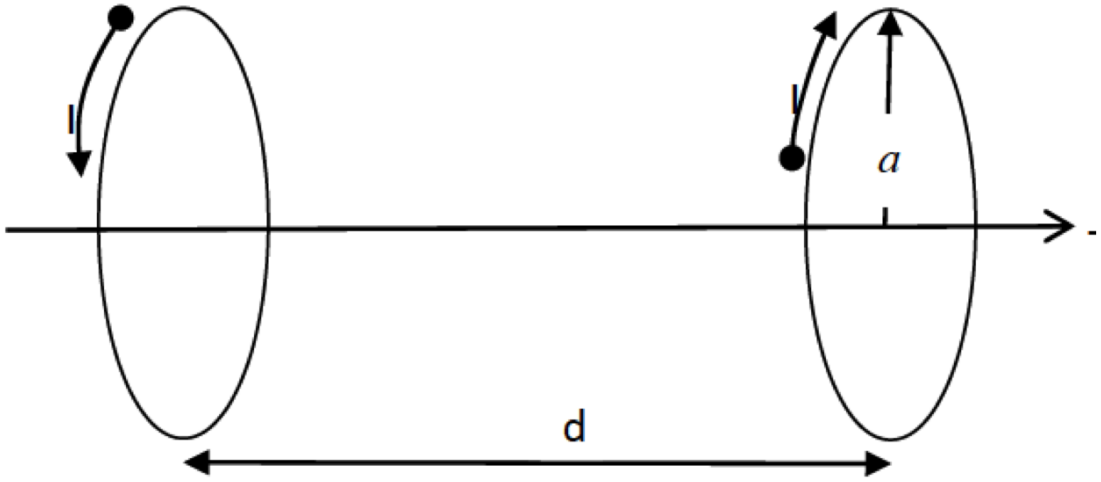


Figure 4.7. Maxwell Pair. The separation between coils is related to the the diameter of the the cylindrical core as $d = \sqrt{3}a$

For the Z gradient, coil separation d was 43.9 cm. The magnetic fields at either ends of the Maxwell coil pair can be calculated using the formula in equation 1.23.

For our case, given the radius of the coils and their separation, the magnetic field gradient was estimated by calculating the magnetic field strength at either side of the coils and dividing by the coil separation. We calculated this to be 19.8 $\mu T/m/A/Turn$. Litz wire of AWG 16 with 100 strands was used in the construction of gradient coil. The number of turns was 10 giving a gradient field of 198 $\mu T/m/A$

4.2.1 Design of the Golay four saddle gradient coils

The Golay type gradient coils [75], [76] were used to provide gradient magnetic fields in the X and Y directions (Figure 4.8).

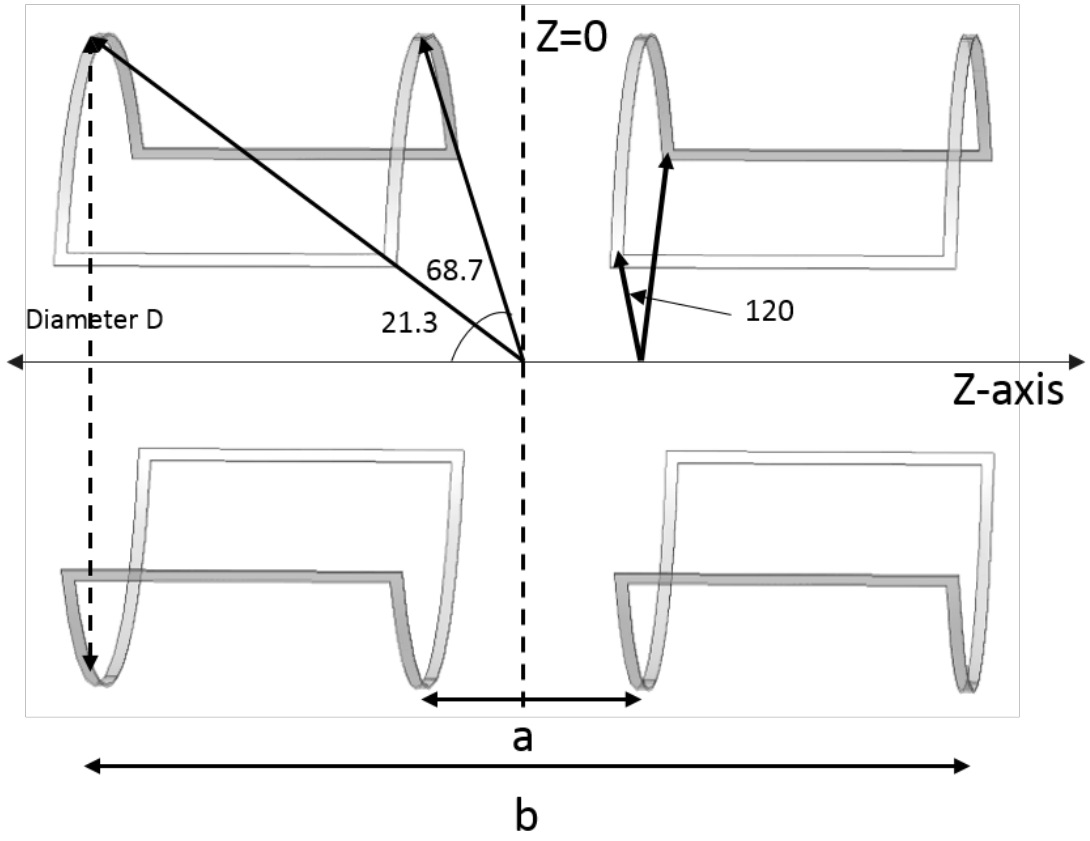


Figure 4.8. Saddle coils showing the x-gradient. The y-gradient is constructed by rotating the saddles by 90^o

Saddle coil positions are defined by the diameter and angles they subtend at the center of the coil system. In designing MRI coils, one has to take into consideration the length of the tube. If the system is too long, it might cause claustrophobic effects. Given the diameter of our system, following this configuration would require that the outer saddles are located at least 67 cm from the center, making the whole tube 134 cm long. Our design proposed to reduce the length of the tube but

still maintaining the linearity of the gradients. Given that our region of interest (ROI) is a sphere with a diameter of 25 cm, we varied the position of the outer saddles to get the shortest position that would give an acceptable linearity of the gradient magnetic field.

To investigate the linearity of the magnetic field, we followed the procedure used by Rashid et al. [77] shown in figure 4.8. In their investigation, they found that the saddle angle of 120^o gave the best results. Therefore with the angle set at 120^o and a set by the dimensions shown in the figure Figure 4.8), we varied b from 134 cm to 44 cm in steps of 10 cm. For each value of b, we plotted the 1D magnetic field linearity across the ROI.

4.2.2 COMSOL set-up and simulation

The geometry was set up in comsol as shown in figure 4.8. The diameter D of the system was 52 cm, the saddles were modeled as multi-turn coils with 10 turns. A current of 2.5 A was injected into the coils. Results of the simulation are shown in figure 4.9.

From the graphs, magnetic field gradients of 300 $\mu T/m$ could be achieved. We realize that there is no significant difference in the magnetic field linearity for different positions of outer saddle location. We therefore went ahead to select 64 cm as our saddle position. This would conveniently locate the saddles just after the outer Bm coils.

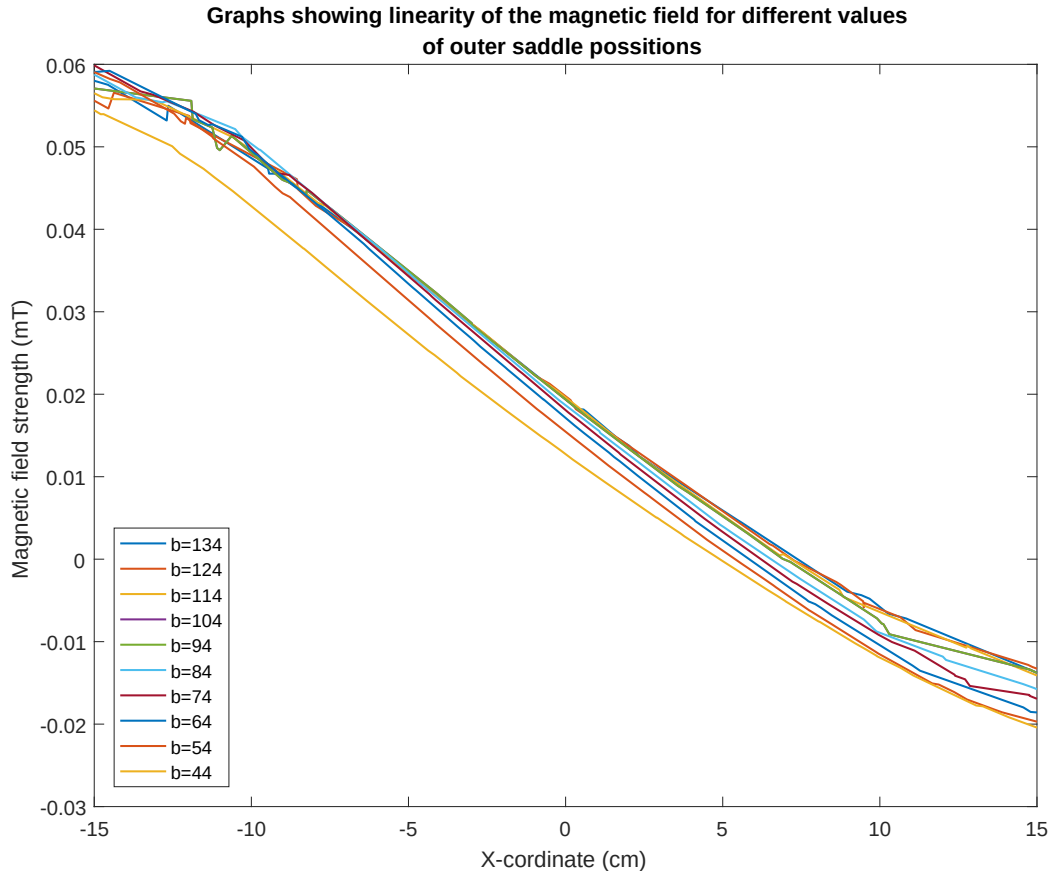


Figure 4.9. Graphs showing linearity of the x gradient magnetic field for different positions of the outer saddles

.

4.3 Construction of the B_p coil

As described earlier in chapter two, the B_p magnetic field is relatively stronger than the B_m field but with less restrictions on field homogeneity. As a result, the B_p can be constructed as a solenoid coil, which is much easier to construct.

From equation 1.5, we can deduce that the magnetic field at the center of a solenoid is given by

$$B = \frac{\mu_o N I a^2}{2(a^2 + L^2)^{\frac{3}{2}}} \tag{4.14}$$

where N is the number of turns and a is the radius of the coil, I is the current flowing through the coil and L is the solenoid length [12]. Correction factors can be included into the formula to compensate for coil thickness and spacing but for simplicity, the design emphasizes a simple calculation of the field at the center.

The solenoid coil was wound on an aluminum core of radius 15 cm and length 30 cm. These dimensions were determined to accommodate the human head. Copper wire of 10 AWG procured from MWS wire industries was used. The 10 AWG copper wire has diameter of 2.5883 mm, resistance of 3.277 mΩ/m and weight of 46.773 g/m.

Given the specifications of the coil used, the number of turns per layer was 95 and there were 12 layers giving total number of turns to be 1140 turns and coil thickness of 3.1 cm. The length of the wire used was estimated to be 1300 m. From coil length, the weight of the coil was estimated to be 60 kg with resistance of 4.3 Ω

Using equation 4.14, we calculated the magnetic field strength per unit current at the center of the solenoid to be $\approx$ 5 mT/A

4.3.1 COMSOL simulation of B_p coil

The B_p was modeled as multi-turn coil with 1140 turns as shown in the 3D model (Figure 4.10a). I_{coil} of 10 A was used. Figure 4.10b shows the magnetic flux density of the Bp coil along the z-axis of the coil. The magnetic field reached maximum value of 52.5 mT for a current of 10 A as predicted by the calculations.

We see the the magnetic field homogeneity over the region of interest is about 20%. This is an acceptable inhomogeneity for the Bp field where 10%-30% is considered to be appropriate [39].

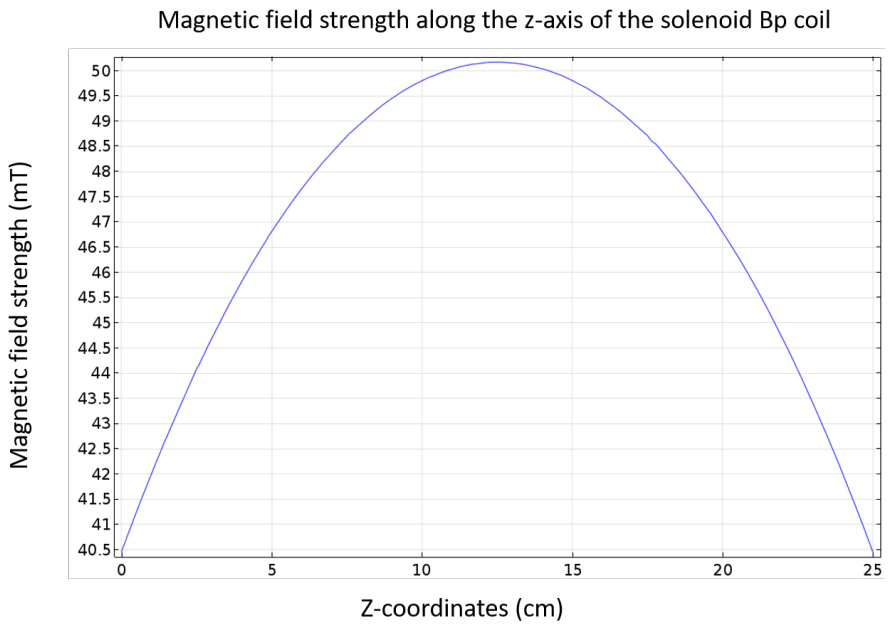


Figure 4.10. Magnetic field along the center of the Bp coil over the region of interest

4.4 Construction of RF coils

Due to the construction and geometry of the B_m and B_p coils, saddle coils are the most preferred RF coils adaptable to this system. Unlike the gradient coils which are constructed from four saddle coils, the RF coils are made from only a single pair of saddle coils. Since we are using two separate RF coils - the transmit coil and receiver coil, it is important to position these coils orthogonally to avoid direct inductive interference between them.

The geometry of a cylindrically shaped saddle coil can be described by three parameters - the length of the coil, the angle subtended by the arcs and the radius of the coil [78].

The saddle coil of this nature will have components of the magnetic field in all three dimensions - x, y and z. Making sure that the magnetic field in the transverse direction becomes dominant needs careful construction and adjustments of the

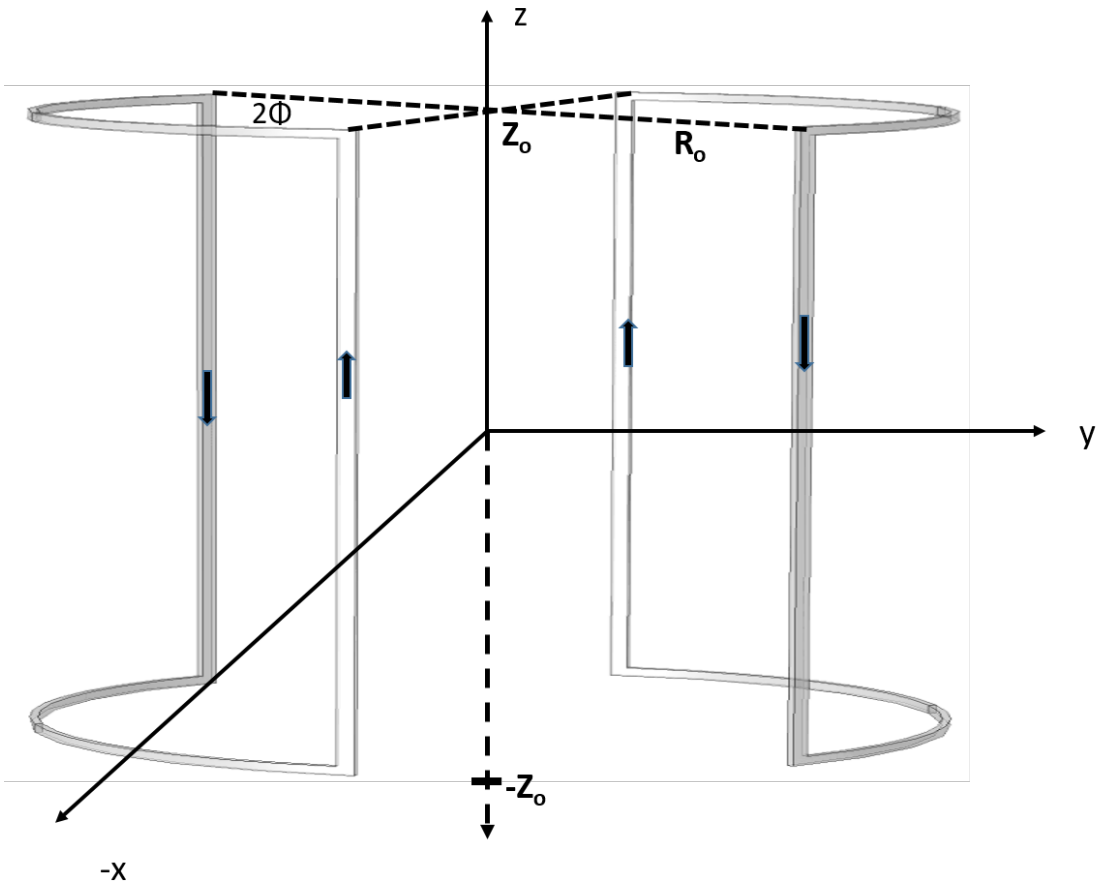


Figure 4.11. RF saddle coil (From [78])

geometry parameters. The magnetic field depends inversely on the radius R_o of the saddle and therefore this parameter is considered insignificant in designing the coil compared to the length Z_o and angle Φ_o [78]. The coil conductors that run parallel to the axis of the coil dominate the x, and y components of the magnetic field.

For the geometry shown in figure 4.11, the magnetic field in the x, and z, directions can be nearly zero. In our PMRI system, we are interested in saddle coils with diameter big enough for adult head. Ginsberg et al. gives a relationship between the arc angle and the length to diameter ratio recommended to generate

uniform magnetic field using saddle coils [75]

Our RF saddle coils were designed with a length to diameter ratio of 1.2 and the arc angle of 121^o. The diameter of the RF coil was 22 cm.

The RF coils were made as resonant circuits with parameters chosen to maximize the quality factor of the coil.

For parallel resonant circuits as used in this case, the quality factor Q is given as [79]. The quality factor of a coil is a parameter that defines the ability of the coil to respond maximally to specific frequencies. The quality factor is defined by the resistance, R of the coil, its inductance, L and the resonant frequency ω as

$$Q = \frac{R}{\omega_o L}. \tag{4.15}$$

And the bandwidth is given by

$$BW = \frac{\omega_o}{RC} \tag{4.16}$$

where C is the capacitance. The values of RC was chosen to be 1/BW $\approx$ 1 x 10^{-4}

Designing for a gradient strength of 0.6 mT/m and field of view (FOV) of 22 cm, a bandwidth of about 6 kHz is needed to cover the whole FOV. This bandwidth can be varied by adjusting the gradient field strength or changing the capacitor attached to the resonant circuit.

4.4.1 COMSOL simulation of the RF coil

The saddle coil was modeled following the general modeling process in COMSOL. Magnetic field generated by a saddle coil is the sum of the fields from the arcs and the linear conductors making up the saddle coil. The saddle coil is made of four

linear conductors and four arcs giving a total field which can be written as

$$B_{saddle} = 4(B_L + B_{arc}). \tag{4.17}$$

The magnetic field of the linear conductors for coordinates extending along the Z-axis for constant x and y coordinates is given by [74]

$$B_L = \frac{\mu_o I}{4\pi r^2}\left(\frac{z_1 - z}{\sqrt{r^2 + (z_1 - z)^2}} - \frac{z_2 - z}{\sqrt{r^2 + (z_2 - z)^2}}\right) \tag{4.18}$$

and the magnetic field of the arc conductors are given by

$$B_{arc} = \frac{\mu_o I}{4\pi}\int_0^{\phi_o} \frac{r_o(z_1 - z)\cos\phi_o}{\left[r^2 + r_o^2 - 2rr_o\cos(\phi_o - \theta) + (z_1 - z)^2\right]^{\frac{3}{2}}} d\theta \tag{4.19}$$

The 3D COMSOL model of saddle coil is given in figure 4.12. The coil was modeled as multi-turn coil with diameter of 22 cm and length of 26.4 cm and 10 turns. For purposes of showing the directionality and magnitude of the magnetic field generated by this type of saddle coil arrangement, a steady current of 2.5 A was injected into the coils. Comsol multi physics generates magnetic field lines by solving the equation 4.11. Results of simulation were processed using comsol tools and graphs showing magnetic flux densities in the x, y and z-directions were plotted. An arrow volume plot showing the direction of the magnetic field was also plotted.

Figure 4.13 shows the directional magnetic field lines of a saddle coil. The direction of the magnetic field is in a direction orthogonal to the axis of the core. In our case, this direction is considered as the y-direction (Figure 4.11). This is how the RF coil made of saddle shaped coils is able to tip the magnetic field into the transverse direction.

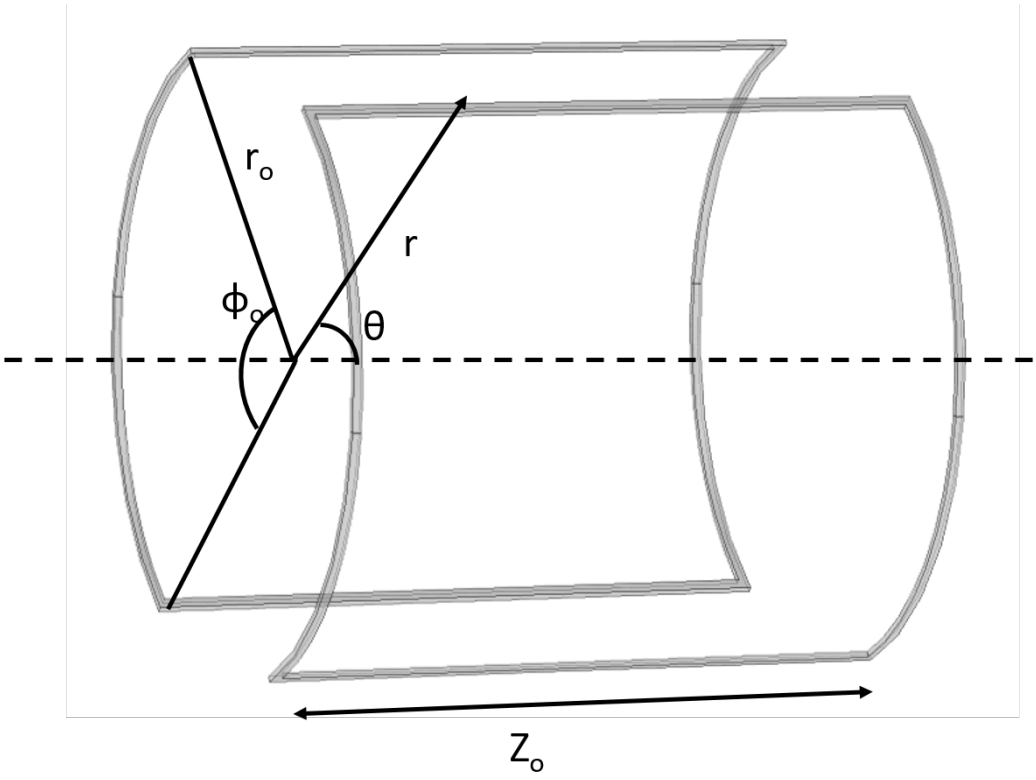


Figure 4.12. 3D COMSOL model of the saddle coil adapted from [78]

Figure 4.14,4.15,4.16 show the x, y and z components of the magnetic flux density of the saddle coil. We see that because of the directionality of the magnetic field produced by the saddle coil, the x and z components are negligible since the magnetic field is in the Y- direction. However, even in the y-direction, the magnetic field is not uniform. The usable volume of the saddle coil is defined as that volume in which the magnetic field uniformity is within 15% [74]. Here we show that the usable volume is 19 cm in Y-direction.

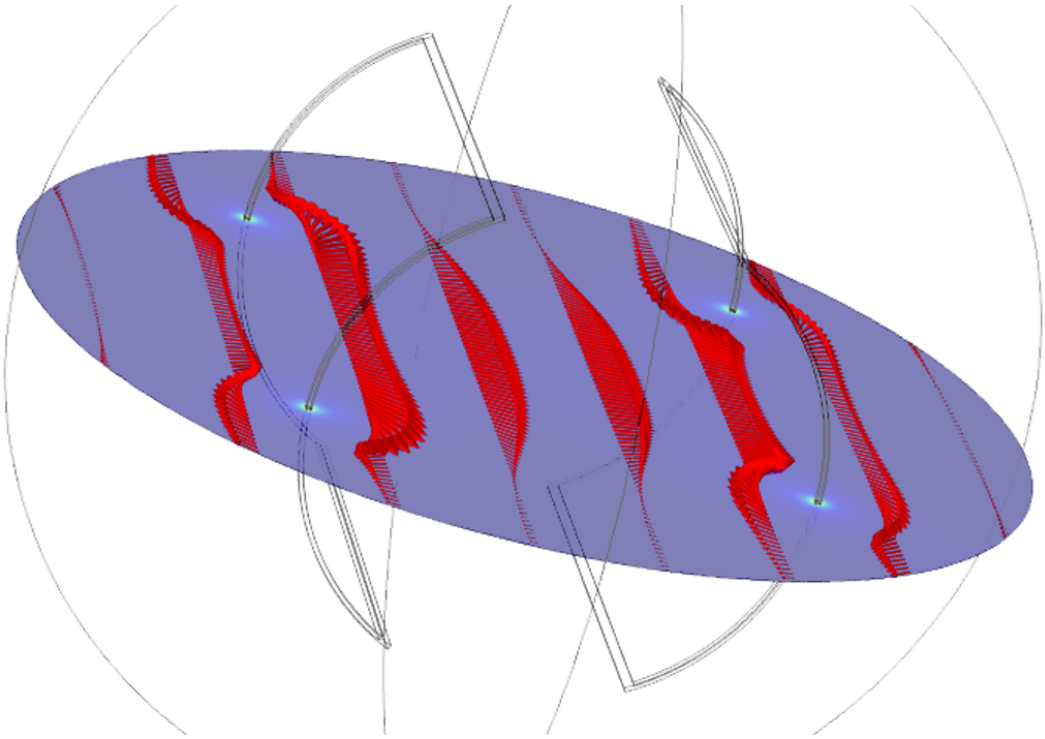


Figure 4.13. Magnetic field direction in saddle coil

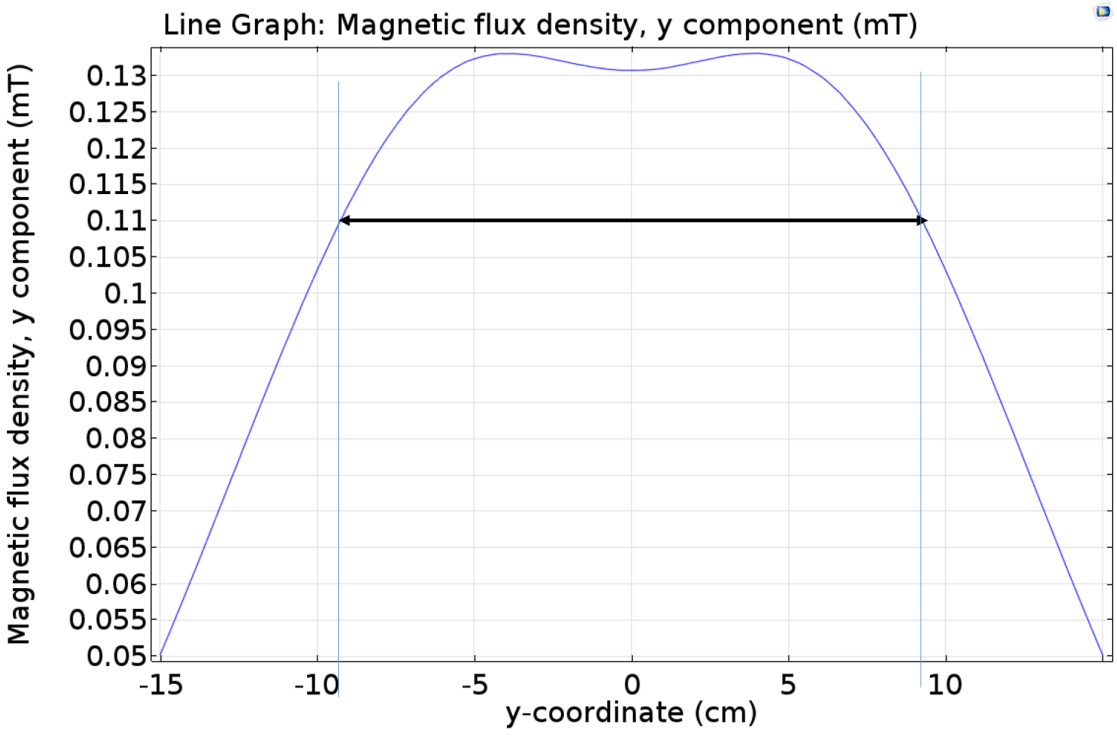


Figure 4.14. Y-component of the magnetic field of a saddle coil

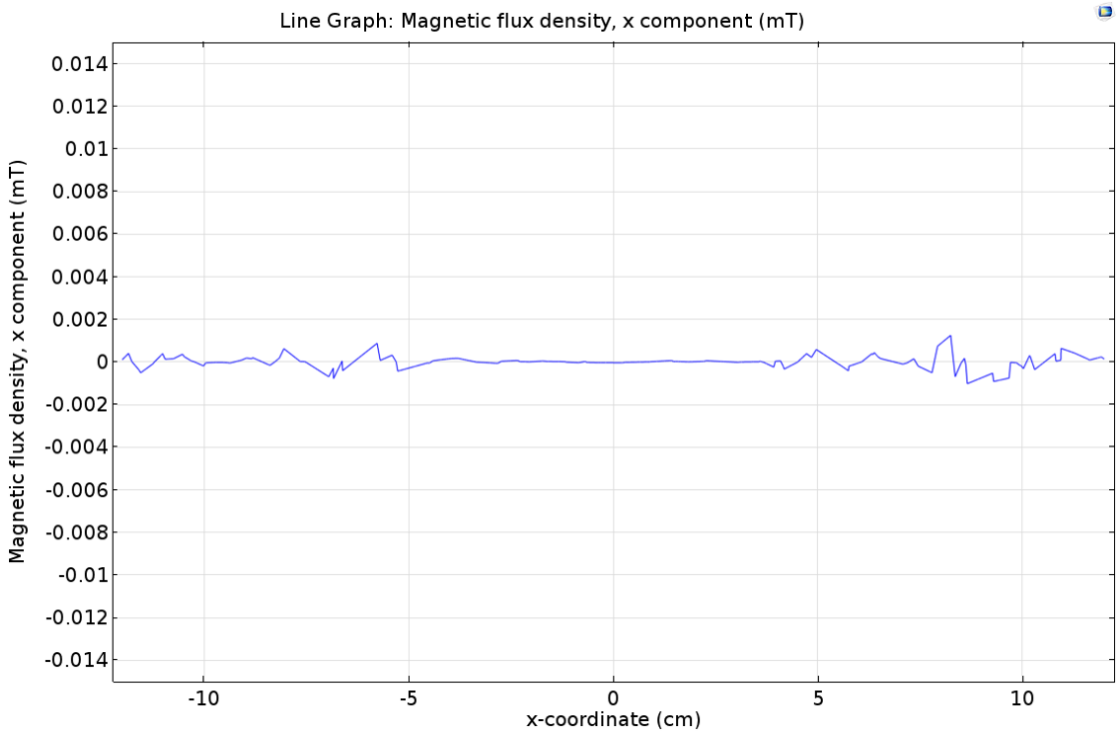


Figure 4.15. X-component of the magnetic field of a saddle coil

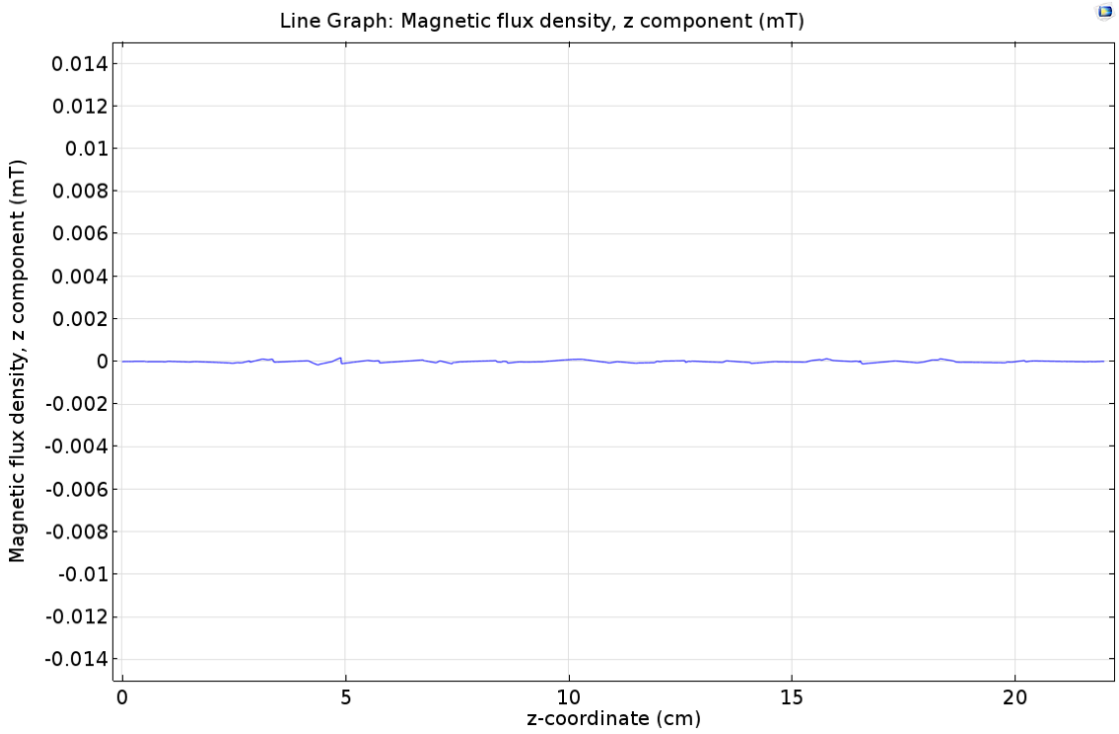


Figure 4.16. Z-component of the magnetic field of a saddle coil

4.5 Cost considerations

As mentioned earlier, the cost of the PMRI system is one very important factor that makes it very attractive and worthwhile to pursue. The costs considered here are hardware costs as procured from vendors. The costs reflected here constitute only those materials that actually were used in constructing the PMRI system. Software development and man-hour costs are not included. The cost of developing soft ware to run the system is estimated at $28,000. It should however be noted that this cost is high for the first unit. Once the software has been customized, its costs for subsequent units will be very low. The total material costs for the PMRI system is approximately $\$20,000$ (Figure 4.17).

Item	Unit	Unit	Unit cost UD	Item cost USD
Single core copper wire	Meters	1000	1.08	1080
power supplies	pcs	3	2255	6765
Labview NI BNC Driver	pcs	1	400	400
Bp switch	pcs	1	600	600
Gradient Amplifiers	PCS	3	1000	3000
BNC connecting cables	PCS	16	15.99	255.84
Shielding materials	PCS	2	200	400
Litz wire	Meters	500	1.34	670
Circuit components	Pcs	assorted	1	2000
Mechanical/carpentry work	-	-	-	3000
Total				18170.84

Figure 4.17. Material costs for the PMRI system

4.6 Other figures of the PMRI system

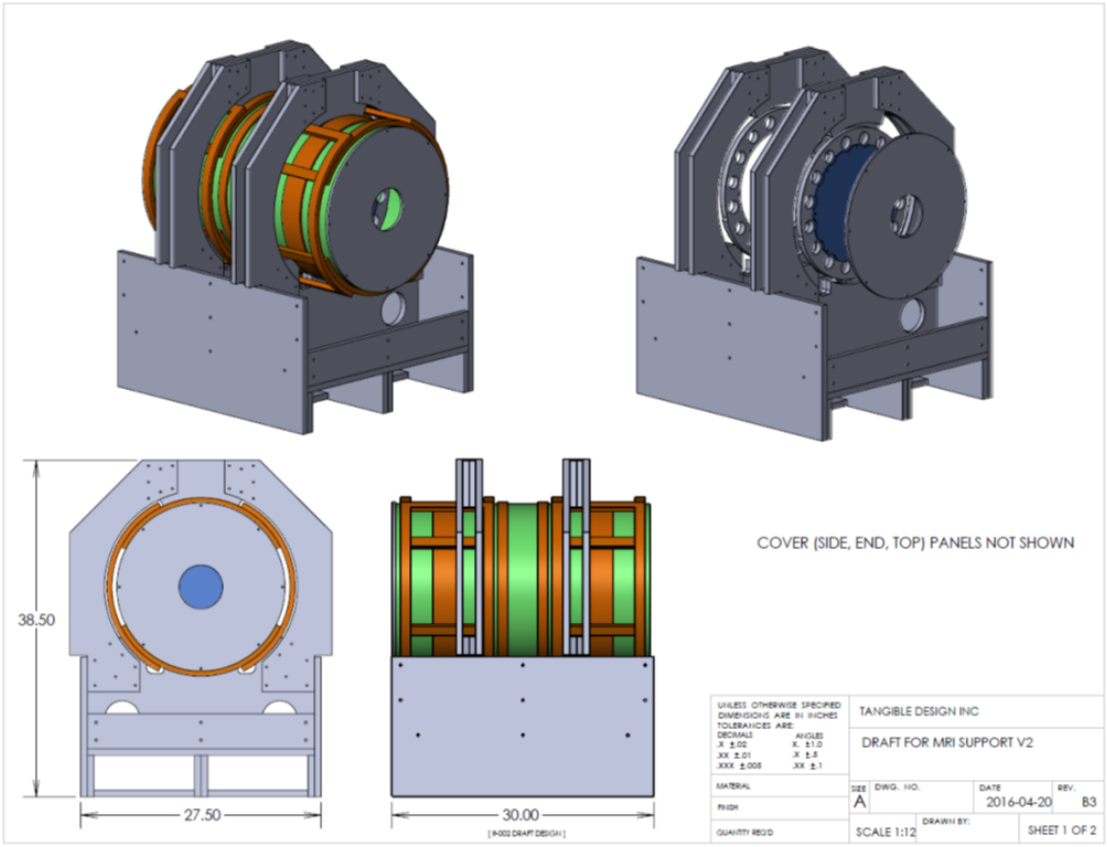
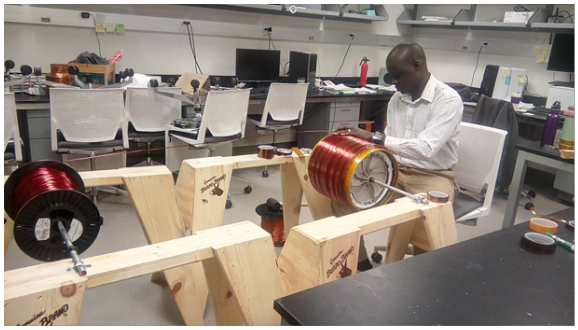
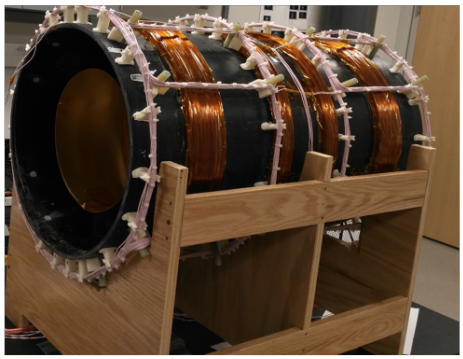


Figure 4.18. 3D drawings of the PMRI system



Coil winding by hand



PMRI system after winding

Figure 4.19. Fabrication of the PMRI system

Chapter 5

CHARACTERIZATION OF THE PMRI SYSTEM

The PMRI system as constructed in chapter 4 is supposed to generate static, pulsating and RF magnetic fields. Understanding the strengths, linearity and homogeneity of these magnetic fields is the purpose of this chapter.

5.1 Mapping the magnetic field homogeneity

Magnetic field homogeneity is one of the most important parameters to consider while constructing MRI magnets. Inhomogeneities in the magnetic field will cause frequency shift artifacts causing inaccuracies in spatial encoding [41]. Inhomogeneities in the B_m field also lead to signal loss as a result of rapid de-phasing of spins within a voxel resulting in low signal to noise ratio (SNR) [80]. More so in MRI imaging, the frequency of the RF magnetic field, normally referred to as B_1 should match the Larmor frequency in order to obtain an effective flip angle. Inhomogeneities in the B_m magnetic field causes differences between the RF frequency

and the Larmor frequency thereby affecting the flip angle. This may result in poor signals due to poor timing of TR and TE which are related to the flip angles [12].

In constructing MRI magnets, the usable volume where the magnetic field inhomogeneity is within permissible range is normally much less than the volume covered by the magnet coils [81]. This range of permissible non-uniformity depends on the strength of the static and gradient magnetic fields [41]. For ultra-low field MRI, images have been acquired with magnetic inhomogeneities of up to 600ppm in magnitude [54]. Magnetic field inhomogeneity u is reported as a deviation from the mean or intended magnetic field B_o normalized by the mean as

$$u = \frac{B - B_o}{B_o}. \tag{5.1}$$

These deviations are normally small and are reported in parts per million (ppm) [71].

5.1.1 Materials and methods

There are several ways of mapping magnetic field inhomogeneities, some of which can be very complex [71], [82], [83]. In our method, we take a more direct approach of measuring the magnetic field across several planes within the volume of interest (VOI) using a gauss meter.

The Gauss meter probe was positioned and manipulated inside the volume using a 3-axis positioner fabricated in-house using aluminum and plastic parts to avoid interfering with the magnetic field. The x, y, and z axes of the 3-axis positioner were designed to be independently adjustable with precision of 2 mm. The axes can be adjusted to cover dimensions of up to 50 cm in each direction (Figure 5.1).

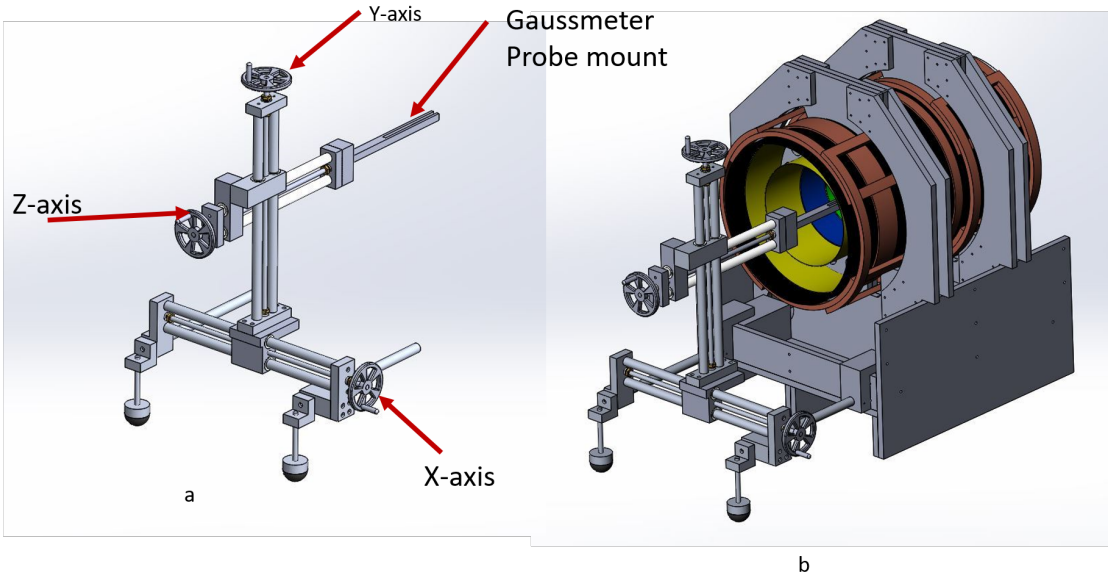


Figure 5.1. a) 3-axis positioner used used for manipulating the Gauss probe. b) The 3-axis positioner mounted on the PMRI system.

The Lake Shore 475 DSP Gaussmeter was used to take the recordings. The Gaussmeter has a sensor probe of 4.6 mm in diameter and 6.35 mm in length with a measurement range of $3.5\mu T$ to 35 T, and can take up to 100 readings per second [84] .

The Lake Shore probe was mounted on the z-axis of the 3-axis positioner, corresponding to the axis of the magnet. The system was arranged in such a way that the (0,0,0) coordinate position on the 3-axis positioner corresponds to the center of the magnet system. A current of 4.721 A was injected into the coils using xantrex XDL 35-5 T DC Power Supply(www.ametek.com). The 4.721 A was chosen so that the magnetic strength at the center of the magnet is 4 mT and also to minimize coil heating. Coil temperatures were also monitored and recorded throughout the duration of measurements. Changes in coil temperature can affect the uniformity of the magnetic field. If temperature changes are not compensated by adequate adjustments in the coil current, the magnetic field strength can change

by as much as 1000 ppm/K [21].

Measurements of magnetic field were taken at spatial intervals of 2 cm within the volume of interest by precisely adjusting the 3-axis positioner. The volume covered was 22 cm x 22 cm x 22 cm. The Gaussmeter used was connected to the computer using a general purpose interface bus (GPIB) and measurements recording using an in-house matlab code.

5.1.2 Results and discussion

Here we present the results of magnetic field measurements covering the region of interest of 22 cm x 22 cm x 22 cm. Figure 5.2 shows the magnetic field map on the XY-planes.

The magnetic field is fairly uniform within the region of interest with average field strength of 4 mT. There is a slight departure from theoretical calculations in terms of the absolute values of magnetic fields measured. Theoretical calculations from equation 4.10 gives magnetic field of 0.8 mT/A and a current of 4.721 A would give and average field strength of 3.78 mT. These could be attributed to the imprecise positioning of coils as a result of hand winding. Kedzia et al. have shown that even slight changes in positioning of coils can cause substantial distortions in the homogeneities of the magnetic field [85]. Additionally, when winding coils by hand, its is not possible to apply enough force and eliminate all kinks within the coils. These kinks create current loops which distort the uniformity and strengths of the magnetic field.

Results show that within the region of interest, the mean magnetic field is 4mT with average inhomogeneities of 5000 ppm. It is recommended that to minimize its effects, magnetic inhomogeneities should be less than the gradient magnetic field

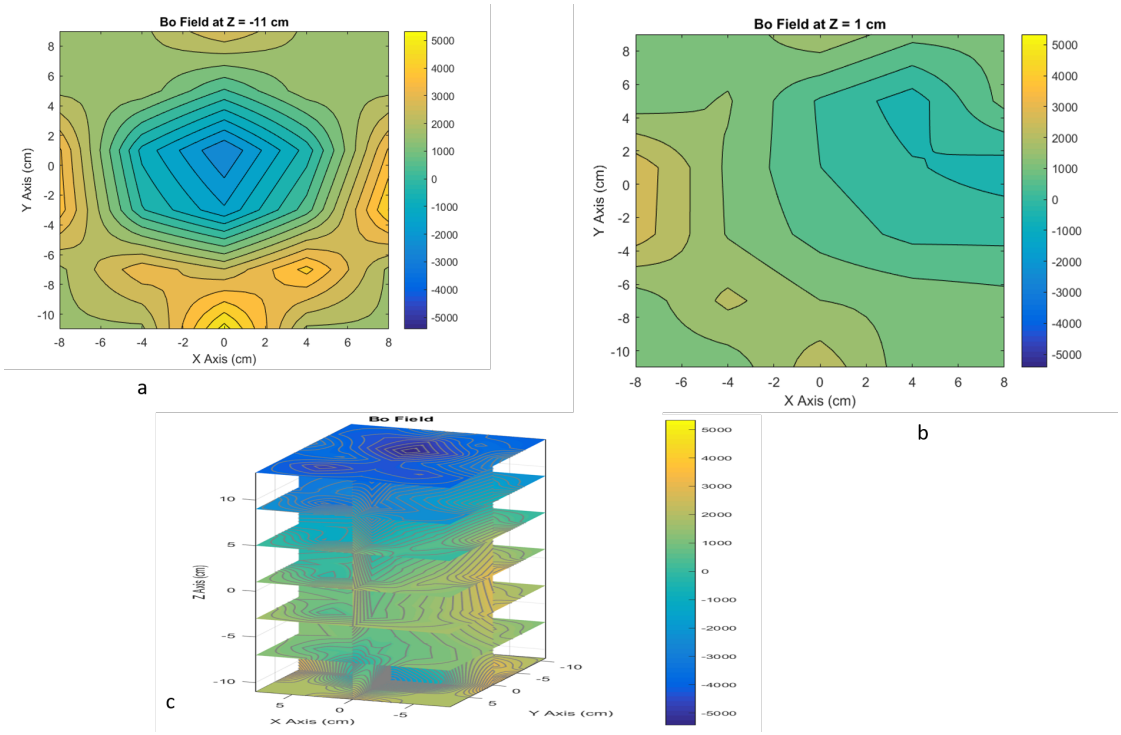


Figure 5.2. Magnetic field map of the Bm magnetic field. The scale is in cm and the color map shows the magnetic field homogeneities in parts per million (ppm). a) is field map of the xy plane at z=-11cm from the center of the magnet and b) is the magnetic field homogeneity closer to the center of the magnet, at z=1cm and. c) shoes the magnetic field homogeneity at different xy planes along the z axis

strength per voxel or pixel [41]. For ultra low field MRI, image resolution of 2.5 mm x 3.5 mm have been shown to reveal considerable brain structure [55]. For diagnosis of hydrocephalus therefore, a more coarse in-plane resolution of 3 mm x 3 mm is thought to be adequate.

Considering that our average magnetic field deviation from the mean field of 4 mT is 5000 ppm over and area of 22 cm x 22 cm, the frequency shift over a 3 mm x 3 mm pixel will be 12 Hz. Our gradient strengths have therefore to be greater that 12 Hz per pixel. Additionally since we are using resistive saddle coils as sensors, these coils are not sensitive enough to pick up such minute frequency shifts. This is because the signal detected by a resistive coil sensor is a function of its the resonant

frequency [86]. This means that an additional 12 Hz on the resonant frequency may not significantly change the magnitude of the signal detected.

5.2 Linearity of gradient magnetic fields

Gradient magnetic fields are responsible for spatial encoding of the acquired signal. Image quality depends in part, on how accurately the signals are mapped onto k-space. The Fourier Transform of the signal detected is a function of spatial location which is assumed to be linearly varying with the gradient magnetic field [32]. Departure from linearity will result in image distortion.

In this section we characterize the linearity of the x, y, and z-gradients and compare the linear variation in magnetic fields to the field inhomogeneities the Bm field.

5.2.1 Materials and methods

Similar to mapping the B_m magnetic field, the magnetic field strength generated by gradient coils were measured using the Lake Shore 475 DSP Gaussmeter guided by the 3-axis positioner.

Each gradient magnetic field was separately measured by connecting a particular coil to the power supply and disconnecting all other coils. A current of 2.5 A was used for each gradient and measurements were taken at spatial intervals of 2 cm. Here we are more interested in the linearity of the gradient field rather than the uniformity of the field.

5.2.2 Results and discussion

Figure 5.3 shows the color map of the the y-gradient magnetic field on the xy plane at Z=0. The contour lines are spaced $15\mu T$ apart. We can see that the contour lines are almost parallel to each other, an indication of the uniformity of the gradient magnetic field. For the current of 2.5 A injected into the Y-gradient coil, the gradient strength is found to be approximately 600 μT/m. To put this into perspective, this means that for a pixel size of 3 mm in the y-direction, this corresponds to a frequency shift of approximately 77 Hz. This is much greater than the frequency shift caused by the inhomogeneity in the Bm magnetic field. This implies that changes is the magnitude of the signal detected will result from the gradients rather than from inhomogeneities in the magnetic field. Therefore the images acquired are less likely to be affected by these inhomogeneities. The strength of the magnetic field gradient can be increased by increasing the amount of current injected into the coils, further minimizing the effects of Bm inhomogeneities. However, signal processing algorithms can also be used to correct for such frequency shifts since their values are known.

Similarly, the z-gradient magnetic field z-gradient field is 600 $\mu T/m$ giving a frequency shift of 77 Hz per pixel and the X-gradient is 700 $\mu T/m$ translating into a frequency shift of 89 Hz per pixel, both of which are greater than the 12 Hz frequency shift provided by the inhomogeneities in the Bm magnetic field (Figure 5.4).

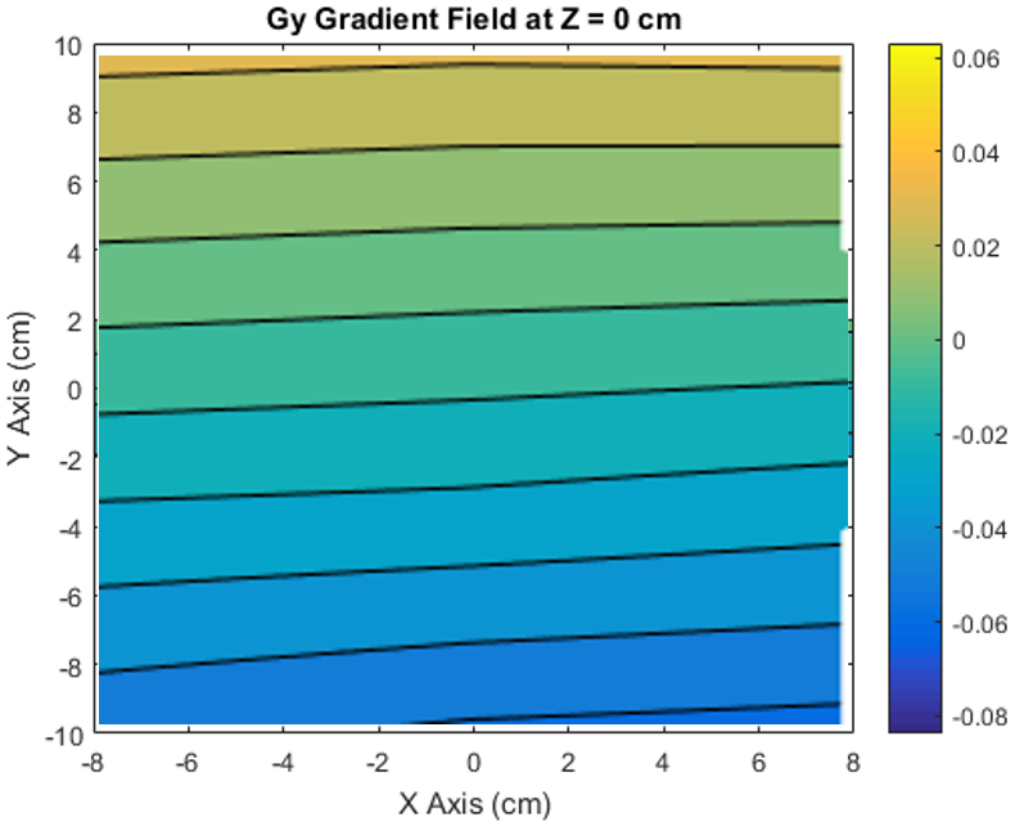


Figure 5.3. Magnetic field color map showing the y-gradient. Contour lines are spaced 15 μT apart

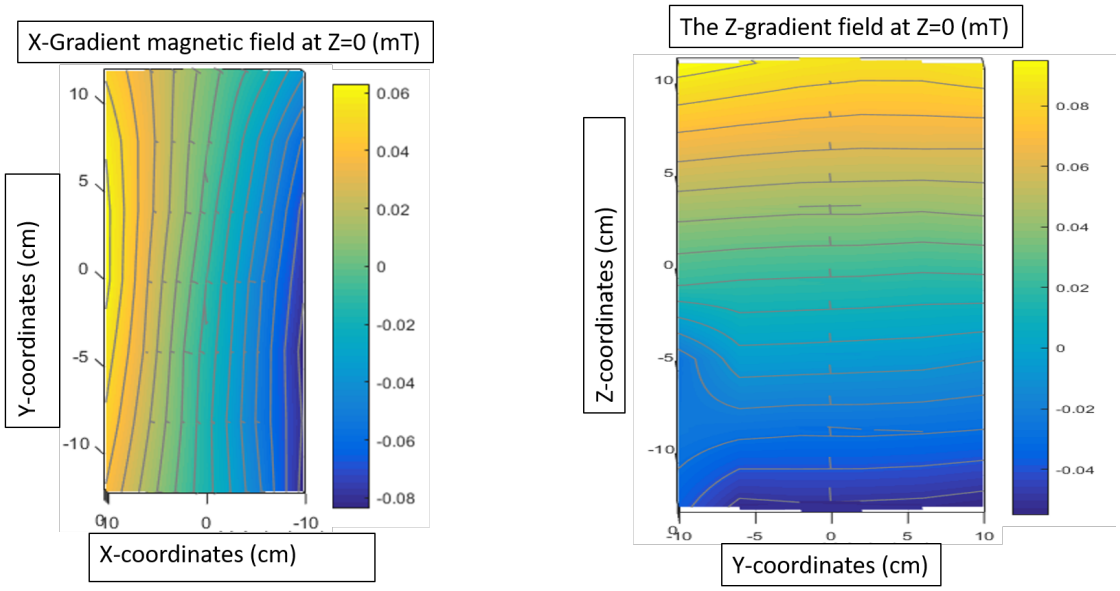


Figure 5.4. Magnetic field linearity in the x and z directions

5.3 Power requirement and coil heating of the Bp coil

The specific absorption rate (SAR) is defined as the RF power deposited into the sample being imaged over a period of time. This RF power translates into increased temperatures in the sample or tissues and is quantified in watts per kilogram (W/kg). The IEC 601-2-33 [87] specifies the safety SAR limits for MRI as 4 W/kg for whole body average and up to to 10 W/kg for extremities over the imaging period, usually six minutes. The SAR increases with frequency because at higher frequencies, the wavelength of the electromagnetic (EM) wave is small enough to interact significantly with tissues resulting into tissue absorption of the wave energy.

Tissue heating also arises from eddy currents generated in the tissue by the radio frequency magnetic field, B_1. These eddy currents generate heat as resistive losses due to tissue resistance. Since SAR is very much a product of electrical heating, it is given as

$$SAR = \int \frac{\sigma(|E_x|^2 + |E_y|^2 + |E_z|^2}{2\rho} dV, \tag{5.2}$$

over the whole volume V, where σ is the object conductivity,ρ is the object density, and E is the RF electrical field [88]

Because of the dependency of SAR on frequency [89], tissue heating as a result of eddy current induced in tissues from low field MRI systems are negligible since these systems use relatively low frequencies compared to the conventional MRI [88]. There is however significant heating by conduction and convection as a result of coil heating. At this level of magnetic fields, the challenge is to keep the imaging volume

at room temperature. Coil temperature measurements are therefore necessary. The rate of change of coil temperature due to power applied to the coils can be estimated as

$$\frac{dT}{dt} = \frac{P}{mC_p} \tag{5.3}$$

Where P the power dissipated by in the coils, m is the coil mass and C_p is the specific heat capacity of the coil, which is 385 $J/(kg/^oC)$ for copper [90].

Mass m of the conductor can be given by

$$m = \rho * V = \rho * A * L \tag{5.4}$$

where ρ is the mass density, V is the volume, A is the cross sectional area of the conductor and L is its length.

We also know that electrical power P can be given by I^2R, and resistance R given by

$$R = \frac{L}{\sigma * A} \tag{5.5}$$

where σ is the conductivity of the material. Substituting equations 5.4, 5.5 and the expressions for mass and power, equation 5.3 becomes,

$$\frac{dT}{dt} = \frac{1}{\rho C_p \sigma_c}(\frac{I}{A})^2 \tag{5.6}$$

where ρ=8920 kg/m^3 and σ =5.8 x $10^7 S/m$ for copper. This equation can predict temperature rise within the coils to a good approximation for short durations of time below 10 minutes [41].

This heat is transfered within the imaging volume and surrounding space by convection. Monitoring temperature in the coil and in the imaging volume is

therefore very important to make sure the temperature doesn't rise beyond physiologically acceptable levels.

5.3.1 Methodology

The Bp winding is the one that runs on high current and generates most of the heat. The Bp coil is made of 10 AWG copper wire with diameter 2.588 mm and cross sectional area 2.196 x 10^{-5} m^2, length 1300 m and total resistance 4.3 Ω

The coil was supplied with 10 A. Coil temperature was measured using a thermocouple meter FLUKE 179 (www.newark.com) in intervals of one minute over a period of 90 minutes. This time period was chosen because in some cases, we have operated the system continuously for three hours in which case the Bp will be in "on" state for up to one and a half hours. At the same time, the temperature at the center of the imaging volume was monitored using a Gaussmeter temperature probe (Lake Shore 475 DSP Gaussmeter).

Room temperature was first measured by setting both temperature probes on a table in the center of the room for 25 minutes. Then both temperature probes were strapped into their measurement positions (in the center of imaging volume and in the center of coil) and left to settle for another 25 minutes before the coils were energized.

5.3.2 Results and discussion

Room temperatures recorded using the Fluke 79 thermocouple was 24.7^oC and 25.7^oC using the Lake Shore 475 DSP Gaussmeter. We think that the difference in the room temperature measurement is because of calibration differences in the temperature meters.

Results of measured temperatures within the imaging volume and coil are shown in figure 5.5 below

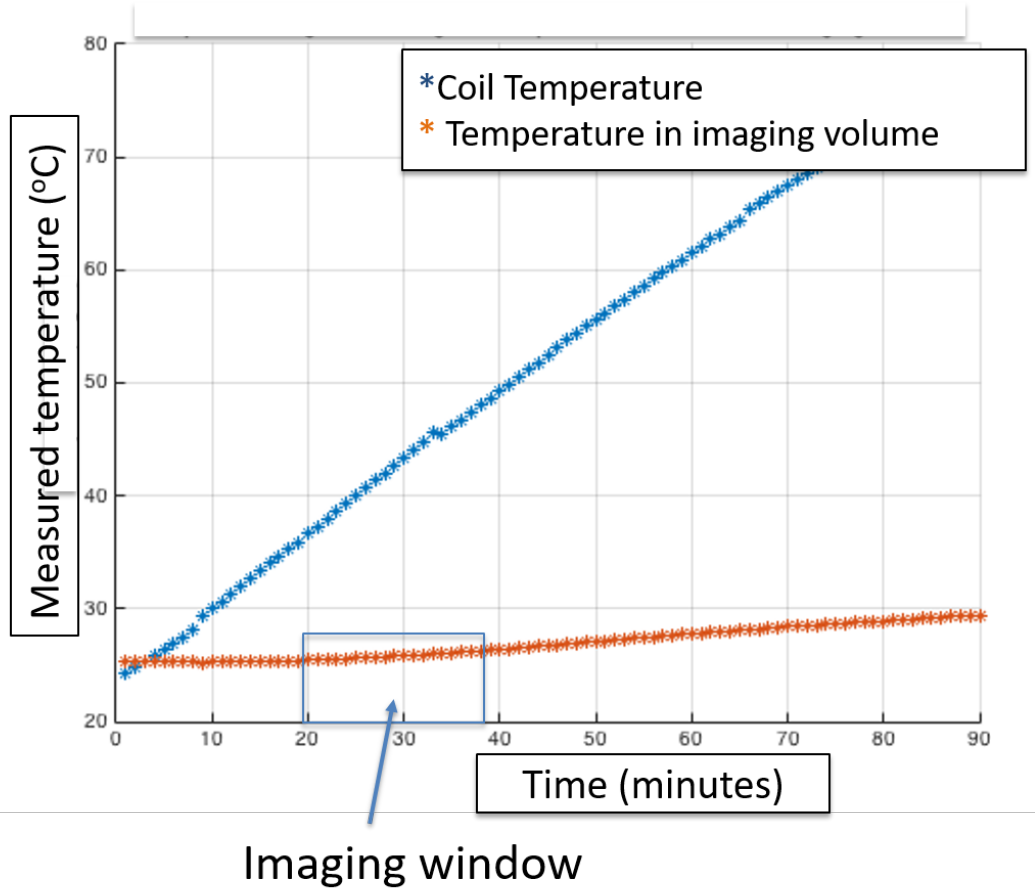


Figure 5.5. The graph shows results of temperature rise within the Bp coil and imaging volume over a period of 90 minutes

.

From the graphs, we can deduce that the temperature in the imaging volume is relatively constant especially over the duration of imaging which is expected to be within 30 minutes for human or animal anatomical imaging. The temperature in the coil are seen to rise up to 80^o. With increase in the magnetic field strength and therefore power requirement of the system, air cooling might be required to maintain the temperatures to physiological levels.

5.4 Construction and testing of electromagnetic radio frequency shield

Magnetic resonance imaging (MRI) is very sensitive to magnetic and electrical interference (noise) which can greatly degrade the MRI signal. Conventional MRI systems require special suites specifically constructed with materials to shield unwanted electromagnetic signals. The cost of constructing these special suites can be as high as $3750 per square foot [91]. To minimize this cost, low field MRI systems are designed to operate in minimally shielded environments. The shielding materials used in low field MRI have therefore to be inexpensive. For this purpose, two types of radio frequency shields were fabricated out of aluminum and brass. To test the shielding effectiveness, a known sinusoidal waveform was transmitted using a radio frequency coil and the transmitted signal was detected using a partially shielded un-tuned coil. The same signal was also detected using an un-shielded coil. A comparison of the two signals showed that the signal amplitude dropped significantly when the coil was partially shielded. Partial shielding was used in order to mimic the real situation where access to the imaging volume has to be allowed.

5.4.1 Theory

In electromagnetic waves, there are electric fields and magnetic fields. In electric fields, it is possible to separate charges into positive and negative charges. For example using Gauss law, it can be shown that the electric field inside an enclosed conductive spherical volume is zero. This is because the charges enclosed within the volume will induce opposite charges on the inside surface of the sphere and these

induced charges will in-turn induce charges of opposite polarity on the outside surface of the sphere. These charges generate electric fields which cancel each other resulting in no net electric field [92]. This shows that it is possible to use conductive materials to separate electric charges and therefore provide shielding. In this case the conductivity of the material is important to provide free movement of electrons making charge separation easier.

Magnetic fields on the other hand are a more difficult to shield. Magnetic charges do not exist. Magnetic field lines run from north pole and will always loop back to the south pole. It is therefore not possible to shield magnetic fields in the way the electric fields are shielded. However, using materials with high permeability, a conductive path can be selectively provided for magnetic fields to essentially direct them away from the volume of interest. on the other hand, Faraday's law explains the relation between magnetic and electric fields. Changing magnetic fields will induce currents on a conductive surface and these currents in turn generate magnetic fields in opposite direction [92]. Therefore thin conductive materials with less permeability μ can also provide shielding for magnetic fields provided the frequency of the magnetic field is high enough to generate eddy currents on the surface of the material. This shielding increases with frequency.

The shielding effectiveness of a material needs therefore to be looked at separately in terms of electric fields and magnetic fields. The distance from the source generating electric or magnetic field is measured in terms of the wavelength λ. If the source of the field is less than $\frac{\lambda}{2\pi}$,the source is considered to be in the near field, and in the far field otherwise. Within the near field, the source of the field determines what field dominates. If the source is a dipole or monopole, the field generated is electric field or high impedance field and if the source is a loop antenna, it generates mainly magnetic field or low impedance field [93].

If the source is however in the far field, electromagnetic waves travel as plane waves and are mainly characterized by their wave impedance. The strengths of the magnetic and electric fields both decrease with increase in distance at the far field. As a result, plane waves are easily attenuated by any solid conducting metal and material thickness becomes insignificant with increase in frequency [93]. At high frequencies therefore, any enclosed material will be able to significantly shield plane waves.

We can therefore say the shielding effectiveness of a material depends on the type of the field, the energy of the field and conductivity and permeability of the material. Shielding then results from reflection of incident RF energy from the surface of the material and absorption of RF energy as the wave travels through the material.

In our experiments, we make the following assumptions: 1. The shielding material is a good conductor which is grounded. This provides a direct path to the ground for any eddy currents generated on the surface of the material by the magnetic field. This limits the ability of the material to shield magnetic fields as the eddy currents will not be able to generate any opposing magnetic fields that would cancel the fringe fields being shielded against.

2. The frequency of our operation is in the kHz range. The magnetic shielding effectiveness, SE, of the material is highly dependent on frequency. Lower frequencies make it difficult for materials with low permeability to shield magnetic fields.

3. The source of wave is very close to the shield and is considered to be in the near field. The wave therefore is not fully developed into a plane wave.

With these assumptions, the shielding effectiveness SE of the material is then given as [94]

$$SE = 20log\frac{4\eta_o}{4\eta} + 20loge^{x/\delta} \tag{5.7}$$

where η_o is the wave impedance of air and η is the wave impedance of the material, x is the material thickness and δ is the skin depth of the material and can be estimated as $|\eta| = \sqrt{\frac{\omega\mu}{\sigma}}$ where σ and is the conductivity and μ the permeability of the material.

Equation 5.7 can be broken down into two parts as;

$$AbsorptionlossA(dB) = 20loge^{x/\delta} \tag{5.8}$$

and

$$ReflectionlossR(dB) = 20log\frac{\eta_o}{4\eta} \tag{5.9}$$

5.4.2 Theoretical illustration of absorption and reflection losses of aluminum and brass material used for EM shielding

Using equations 5.8 and 5.9, we plot theoretical graphs for the shielding effectiveness of aluminum and brass as a result of absorption and reflection losses. The thickness for the aluminum and brass materials used was 0.8128 mm, the conductivity for aluminum was 3.69 x 10^7 Siemens and for brass was 1.59 x 10^7S Siemens.

Figure 5.6 shows the absorptive and reflective shielding effectiveness of aluminum and brass.

From the graphs we see that as the frequency increases, absorption loss in the material reduces. This is because the wavelength of the becomes smaller and is able

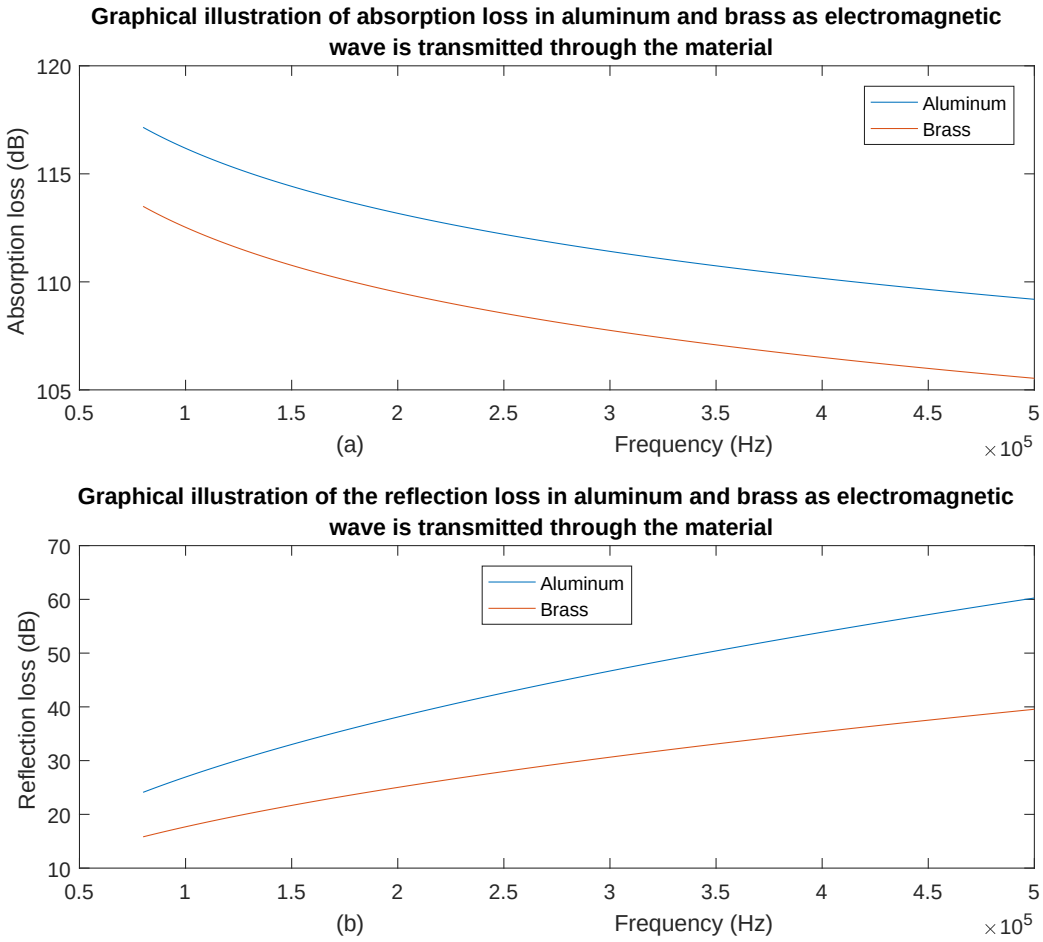


Figure 5.6. Absorption and reflection losses in aluminum and brass

to interact and penetrate the material with little attenuation. On the other hand, the reflection losses increase because of the same reason. The smaller wavelength allows the wave to bounce off the material many times increasing the probability of reflection. The total shielding effectiveness is the sum of the absorption loss and reflection loss.

5.4.3 Fabrication of shields of the RF shields

Two shields where fabricated using aluminum 6061 and brass alloy which were purchased from McMaster Carr (http://www.mcmaster.com/). The thickness of both materials was 0.8128mm, length was 2.44m and width was 0.61m. Each material was cut into two pieces of length 147.32cm and 96.52cm. Each of the pieces was then rolled up end-to-end to form two cylinders of diameters 45.52cm and 30.24cm as shown in figure 5.7

5.4.4 Experimental set-up to test the shielding effectiveness of the shields

In the experimental set-up, a transmit coil was connected to a function generator and located outside the MRI system, 0.5 m from the shield. The receiver coil was connected to a spectrum analyzer and inserted inside the MRI system (Figure 5.8). Sinusoidal waveforms at amplitudes of 2.5 mV peak-peak were generated using a function generator and broadcast using the transmit coil. The receiver coil, acting as receiver antenna detects the amplitude and frequency of the transmitted wave and a spectrum analyzer is used to display these parameters. This was done when the system was shielded using aluminum, brass and when the system was not shielded. The sinusoidal signal was broadcast at different frequencies ranging from 50 kHz to 500 kHz and each time the amplitude of the signal was recorded.

5.4.5 Results and Discussion

Signal attenuation shows on the spectrum analyzer as a reduction in the detected amplitude after shielding (Figure 5.9).

Figure 5.9 is a photo screen of the spectrum analyzer showing amplitude of

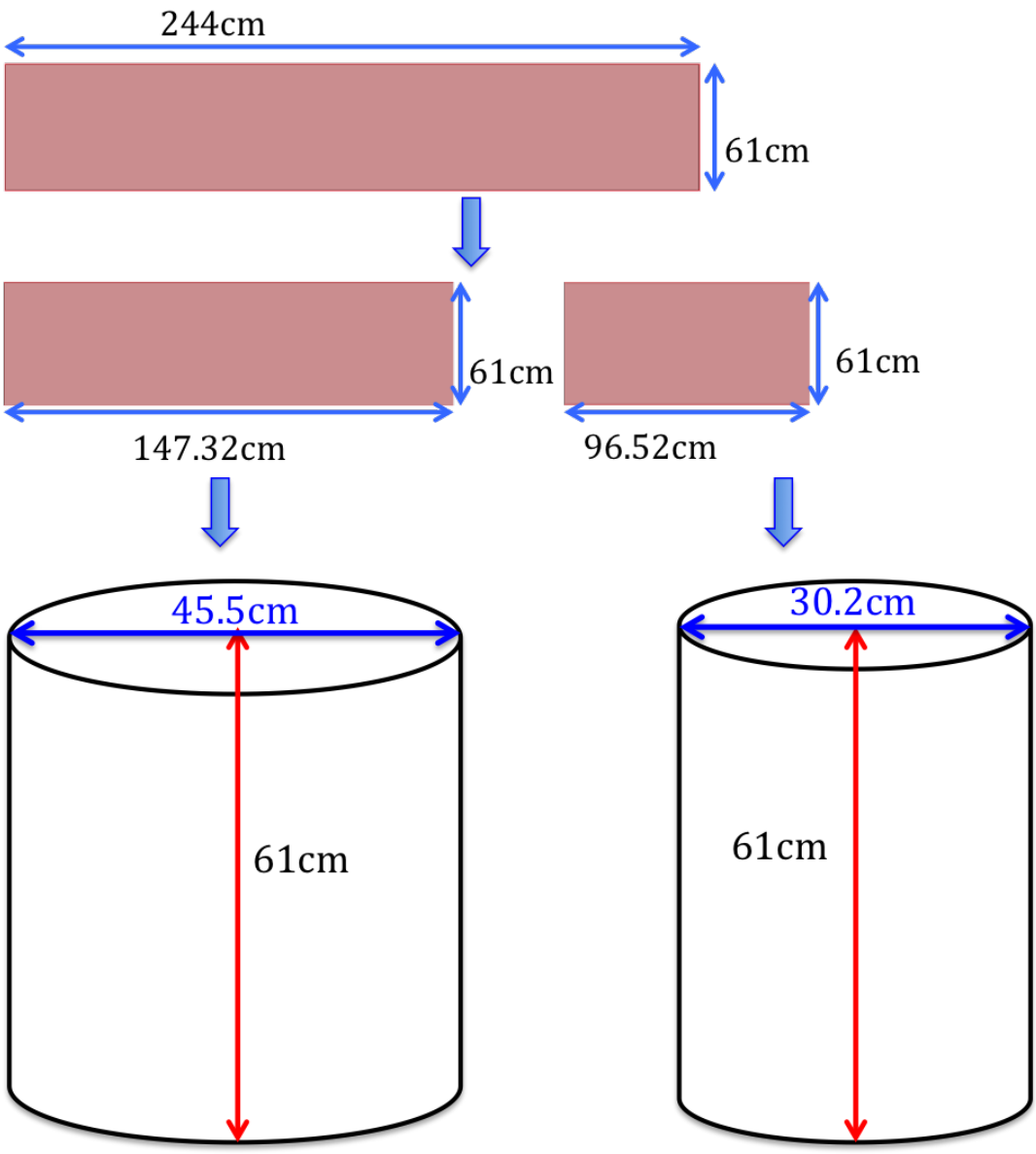


Figure 5.7. Steps in the fabrication of shield

the wave detected before shielding and after shielding. It can be seen that the transmitted wave is significantly attenuated by the shielding material.

Figure 5.10 shows the results measured using the spectrum analyzer for the shield effectiveness of aluminum and brass

As predicted in the theory, we see that at low frequencies, the wavelength is so

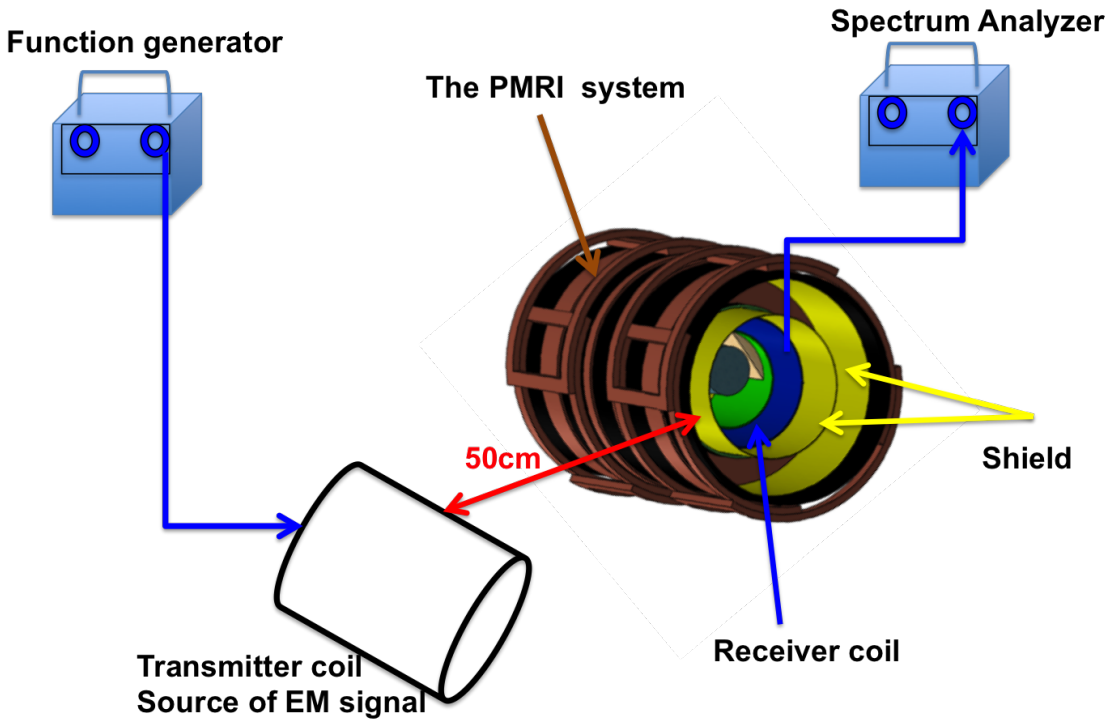


Figure 5.8. Experimental set-up

large that the probability of the wave being incident on the surface of the shield is low. The absorptive and reflective losses are therefore very low. However as frequency increases, the wave can interact with the shielding material and the shielding effectiveness is seen to increase. This is shown in the graphs by the decrease in the amplitude of the signal detected. At higher frequencies, shielding is mostly as a result of reflection rather than both reflection and absorption. The shielding effectiveness os the materials, especially brass in this case is seen to reduce at frequencies beyond 400 kHz.

From the graph, it can be inferred that aluminum is a better shielding material than brass. This could be because of its higher electrical conductivity which contributes to absorption losses. For our frequency of operation which is between 120 kHz and 300 kHz, either material can be used as RF shield.

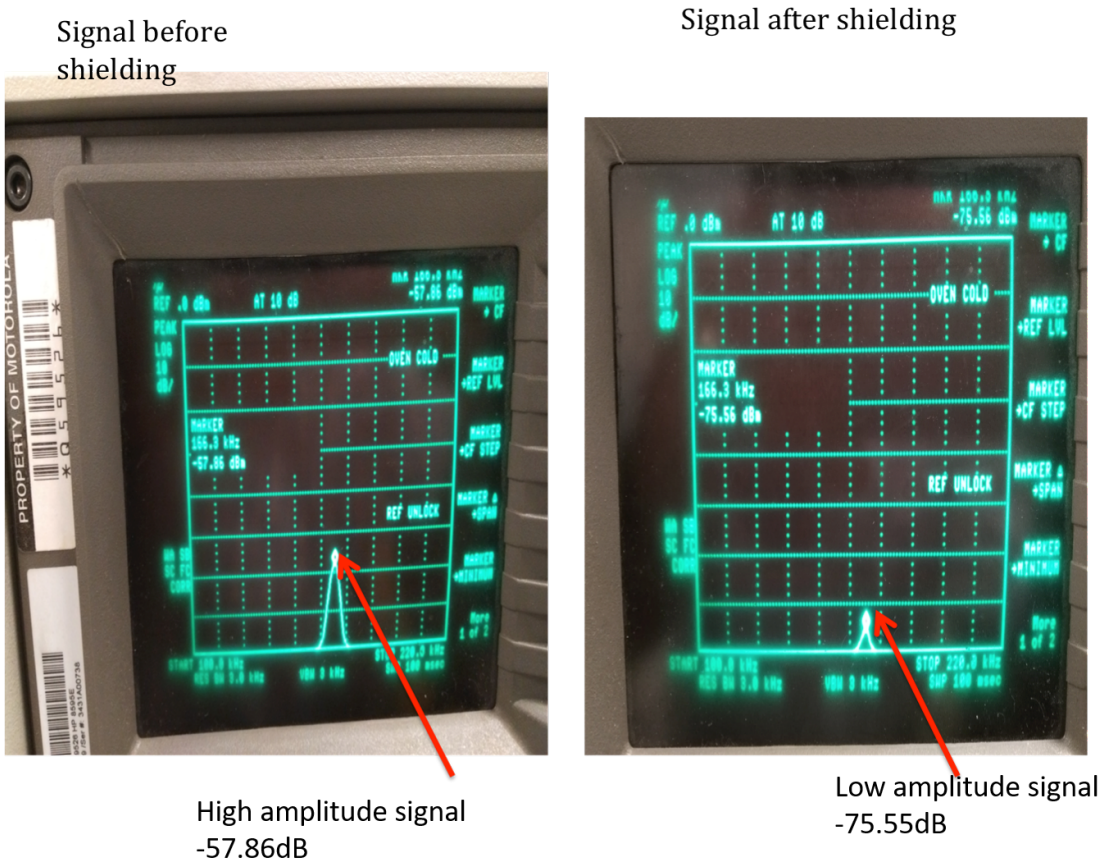


Figure 5.9. Photograph showing attenuated signal

The amplitude of background signal recorded was -80 dB. The Military Standard Handbook 419A suggests that shielding effectiveness of up to 80 dB is adequate enough for most applications [95].

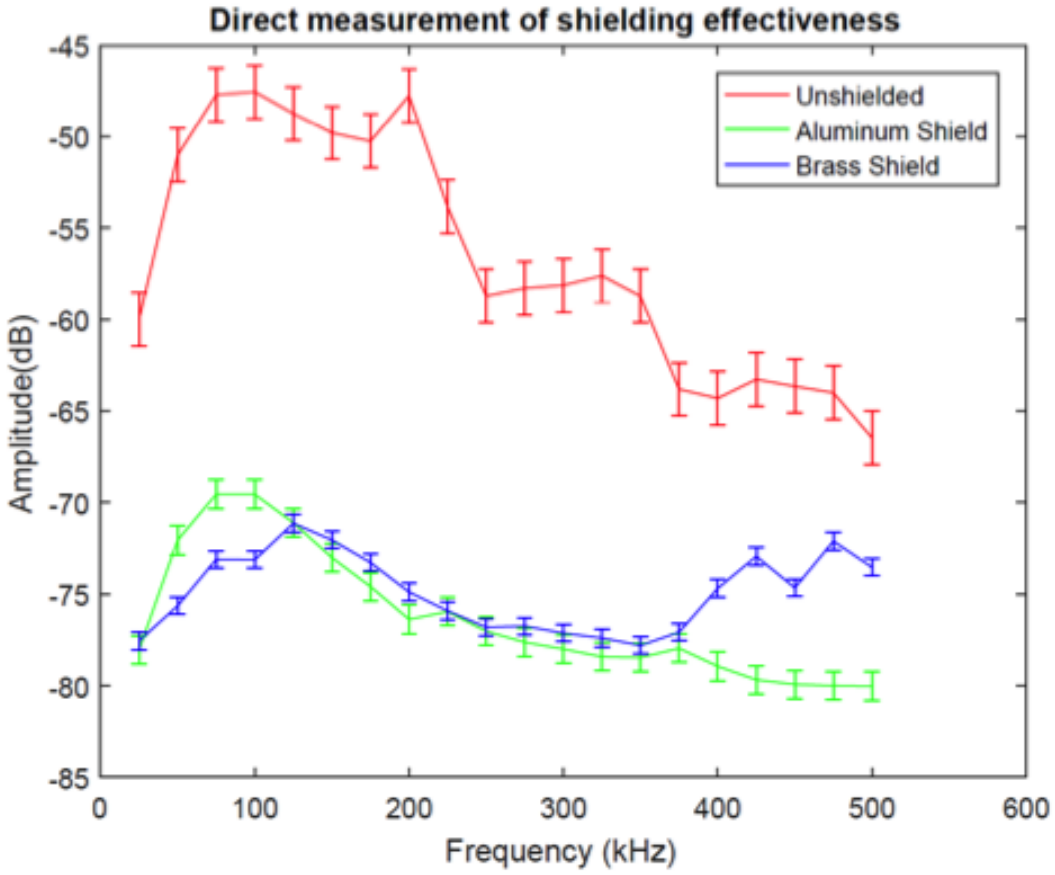


Figure 5.10. Experimental results of shield effectiveness

5.5 Imaging experiments

To image using the PMRI system, the spin echo pulse sequence was used and the following procedure was followed:

a) An appropriate capacitor is connected in parallel with the receiver coil to get a resonant circuit. With the sample in position, the Labview tuning program is then operated to determine the resonant frequency of the receiver circuit. Capacitors are added or removed until the required resonant frequency is achieved.

b) The strength of the Bm field depends on the amount of current that is injected into the Bm coil. This current can easily be manipulated. After tuning

the receiver coil, the current in the Bm coil is therefore adjusted to attain the magnetic field strength that matches the Lamor frequency.

c) The Bp coil is then turned on for a specified period of time, (usually between 1 to 3.5 s) before it is switched off. The Bp and Bo magnetic fields are ensured to be in the same direction.

d) The $\pi/2$ and π pulses are applied. Since $\pi/2$ is applied after Bp has been turned off, some delay time is required between turning off Bp and applying the $\pi/2$ pulse. This delay time should be long enough to minimize the effects of mutual inductance from the Bp coil (Figure 5.11).

e) After application of the π pulse, an echo of the free induction decay signal is formed at a time TE (Figure 5.11).

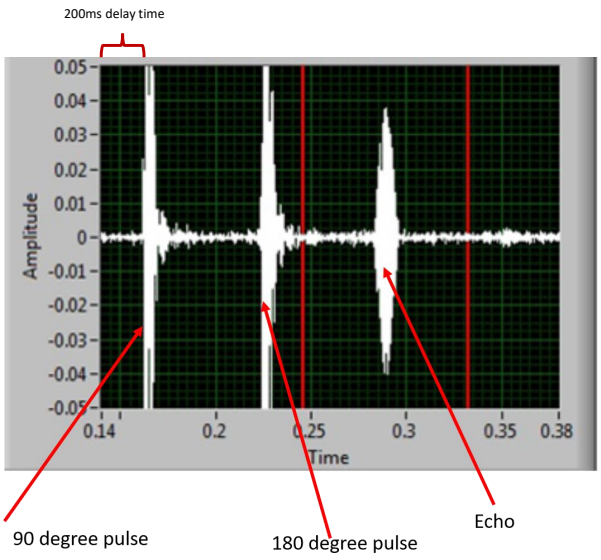


Figure 5.11. Screen shot showing RF pulses and echo. The 90 degree RF pulse is applied after a delay time to reduce the effects of mutual inductance as a result of the Bp field.

In our experiments, images of vegetables and plastic water tubes were acquired at 113 kHz. This frequency was chosen partly because for some reason, other

frequencies were so noisy. Scanning a range of frequencies for the echo signal showed that the frequencies within the range of 112 kHz to 115 kHz produced the highest signal (echo) amplitude.

The first image was that of a bell pepper (Figure 5.12). Imaging parameters used include: Bp field strength 25 mT, repetition time TR 3.35 s, echo time TE 45 ms, number of averages 4, echo delay time 220 ms, and imaging time 8 minutes. The receiver coil used was a saddle coil with diameter of 20 cm. Only one slice of the image was acquired with a slice thickness of 30 mm. This is determined by the strength of the slice selection gradient of 700 $\mu T/m$ and the bandwidth of the RF pulse of 8.9 kHz. Acquiring a large slice allows us to get more signal from the sample.

From the image acquired, the internal structures of the bell pepper are visible. The bell pepper imaged had a diameter of about 8 cm. This covers a small percentage of the usable volume of the receiver coil.

With the same saddle coil of 20 cm in diameter, larger phantoms were used to approximate dimensions of the human head.

One of the phantoms consisted of small water tubes each 1 cm in diameter and 2.5 cm in length. The tubes were arranged in an array to form a phantom 13 cm x 16 cm (Figure 5.13).

From the image of water tubes, the tubes at the center are more clear than the ones at the ends. This could be attributed to the non-uniformities in the RF magnetic field and the the linear distortions of the gradient magnetic fields. Looking at the x-gradient magnetic field in figure 5.4, we see that the contour lines are straight at the center (about 10 cm) and starte to diverge to wards the end of the scale. This can be see in the image of the water tube phantom (Figure 5.13) as the images of the center tubes are more clearer and the signal fades off at the

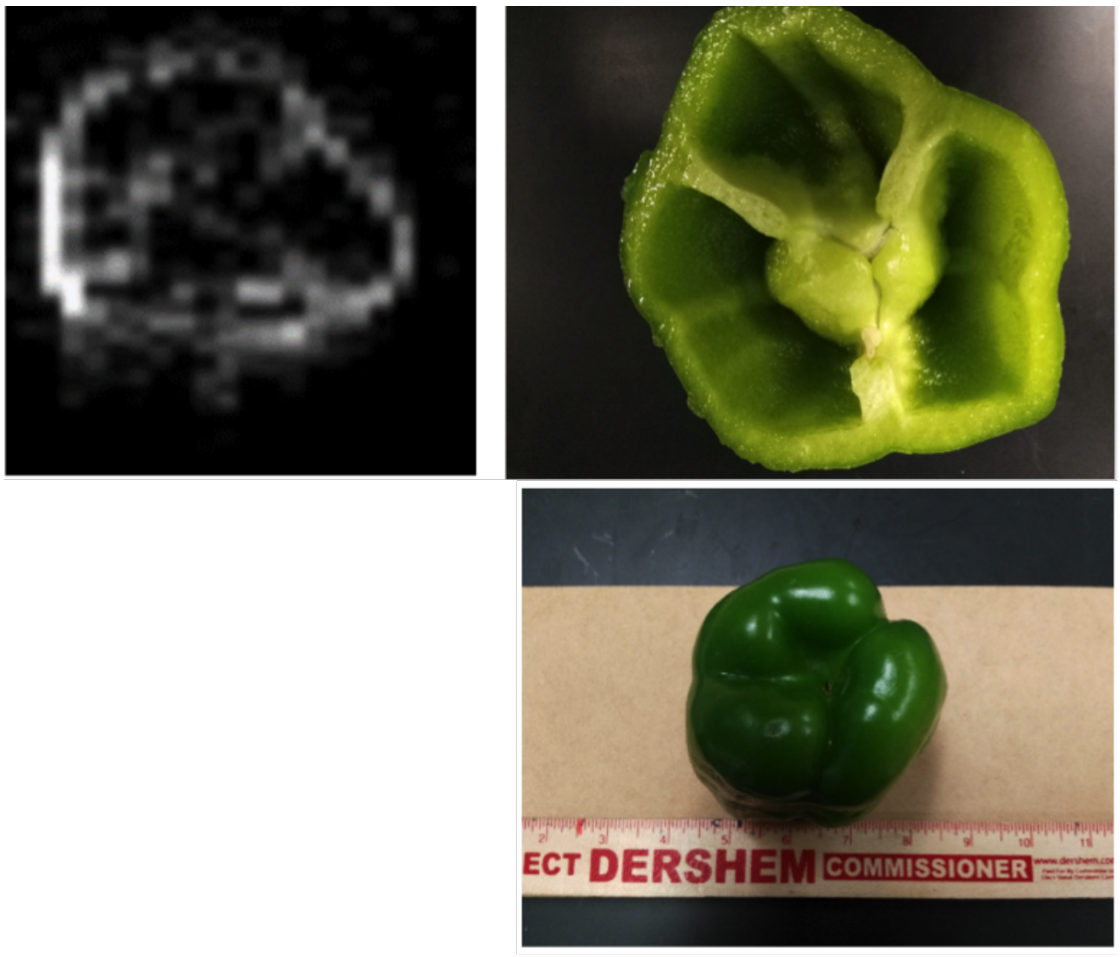


Figure 5.12. Image of green pepper acquired when the system was shielded using aluminum. Imaging parameters are: repetition time 3.35 s, number of averages 4, frequency 113 kHz, pre-pulse field 25 mT, imaging time 8 minutes, slice thickness 20 cm, in-plane resolution 3 mm x 3 mm

outer tubes. Non-uniformities in the RF magnetic fields can also show in an image in which case the stronger field at the center will be able to tip the spins by 90 degrees yet the ones at the ends are tipped less than 90 degrees. This implies that the there is less signal coming from the side tubes compared to the center tubes.

Similarly, an image of water melon was also acquired. The number of averages in this case was 10. To create contrast, we cut the water melon in half, removed a portion of the inside 'flesh" and replaced it with a water filled balloon (Figure

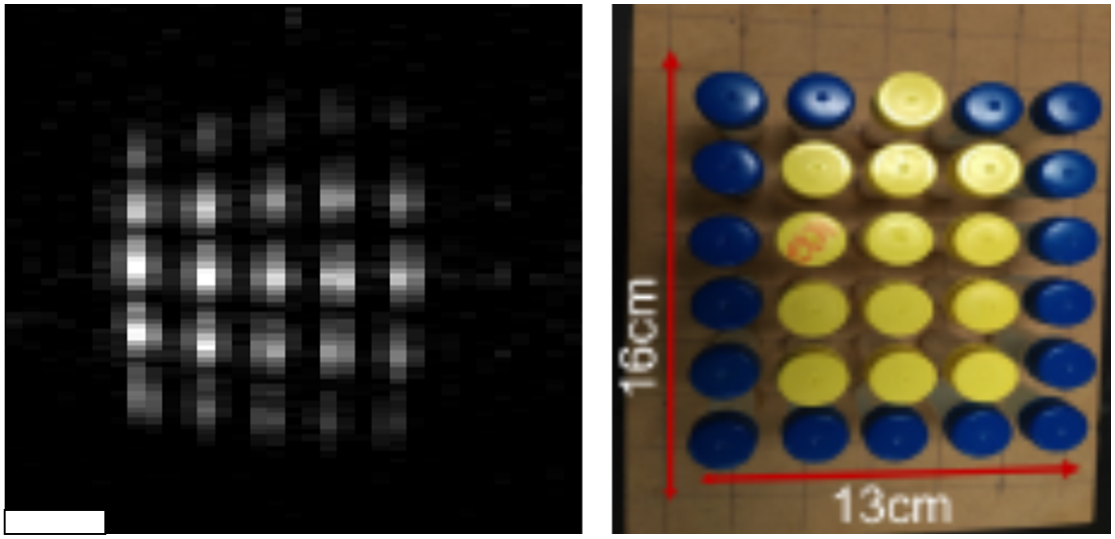


Figure 5.13. Image of water tubes acquired at 113 kHz in 19.5 minutes

5.13). The water melon was 17 cm in diameter. In-plane resolution is 5 mm x 3 mm and slice thickness is 20 mm. The images can clearly show the air gap between the water balloon and the edges of the water melon. These images show that this PMRI system could be improved to perform brain imaging of hydrocephalic children.

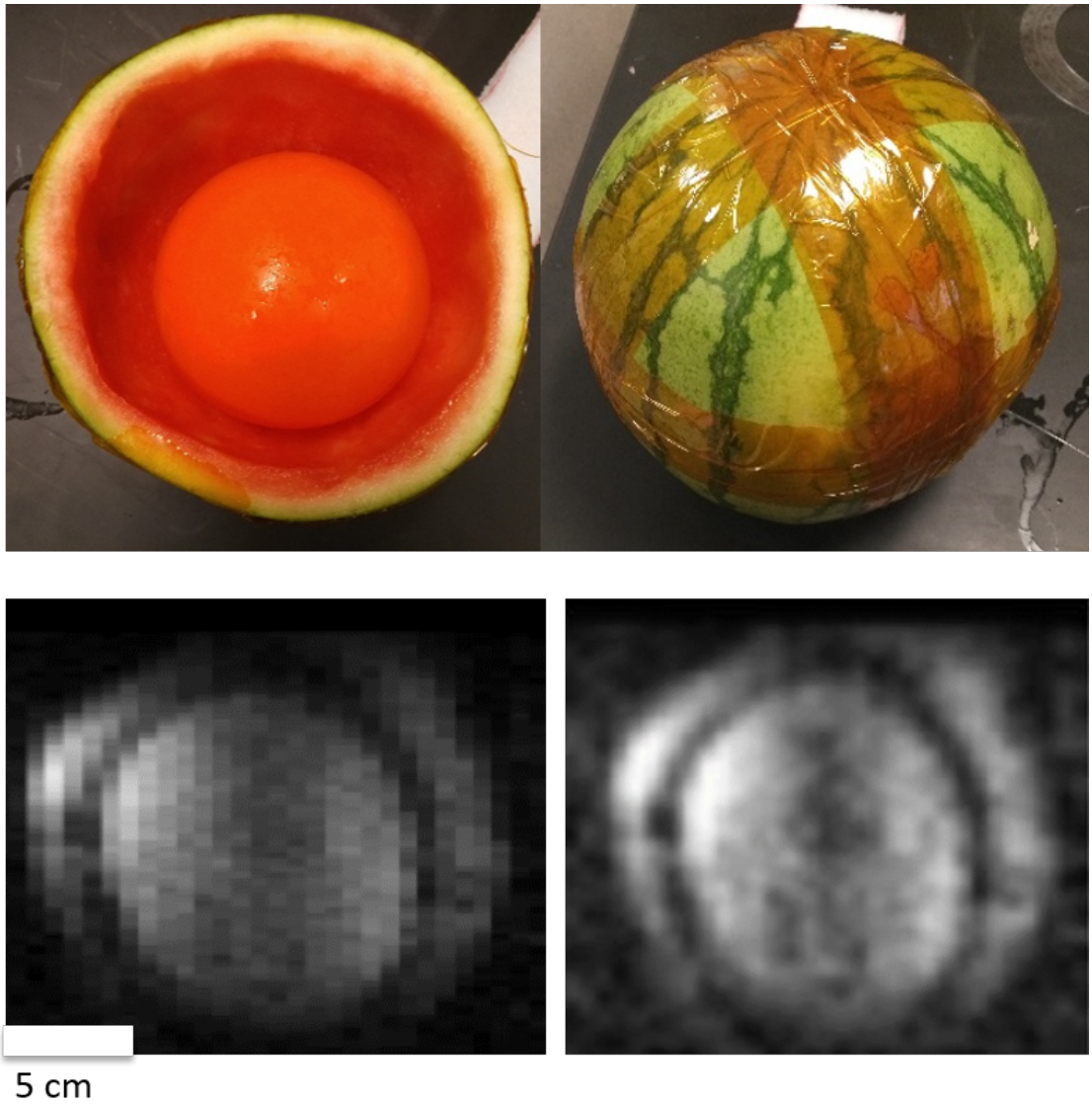


Figure 5.14. Image of water melon acquired at 113 kHz in 19.5 minutes. The original image is shown on the left. The image on the right was processed using a basic matlab Gaussian filter with a standard deviation of 2

Chapter 6

CONCLUSIONS AND RECOMMENDATIONS

The images acquired show functionality of the PMRI system designed here. The fact that the system was assembled by hand using discrete electronic components shows its modular construction which make it easy to replicate and scale in developing countries. The system was operated at a Bm of 2.66 mT and a Bp of 27 mT with a combined power utilization of 550 W. This shows the low power requirement of the system making it suitable for use in developing countries. Furthermore, the flexible and inexpensive aluminum shield used makes this system usable in almost any environment. In-plane resolution 3 mm x 3 mm is adequate for treatment decisions in hydrocephalic cases where interest is to distinguish between cerebrospinal fluid (CSF) and other brain tissue.

The rest of this chapter describes the next phase of this project. The low field MRI is meant for applications in low and middle income countries. This chapter therefore describes in brief, the steps being taken to fulfill that purpose.

6.1 The Biomedical Engineering program at Mbarara University of Science and Technology-Uganda

Mbarara University of Science and Technology (MUST) (www.must.ac.ug) is one of the seven public universities in Uganda (www.unche.or.ug). I have been a staff of MUST since 2007 and one of the programs we looked to develop was a bachelors degree program in biomedical engineering to help minimize the problem of lack of biomedical engineers and technicians in Uganda and Africa as a whole [96]. Collaborations with Dr. Steven J Schiff to develop the curriculum for the biomedical engineering program started in 2010. Coming to Penn State accelerated that collaboration and enabled us to finalize the curriculum by the end of 2015. MUST has had this curriculum approved by the Ugandan National Council for higher education ((www.unche.or.ug)) and in January 2016, the first cohort of biomedical engineering students were admitted into a four year bachelors program.

The curriculum was designed with the idea of medical equipment maintenance in mind and includes hospital practice and equipment repair training right from the first year. The courses that make up the curriculum are given in appendix A. Implementation of this curriculum is currently underway and I will be joining MUST as faculty in May 2017 to help with the implementation of the biomedical engineering program. Research on the ultra-low field MRI technology will therefore find a home at MUST.

6.2 Continuation of the project in Uganda

The local site for the PMRI technology will be Mbarara University of Science and Technology. MUST will be developed into a technical site for this PMRI technology. Laboratory space measuring 27 square meters has already been secured in the basement of one of the buildings.

To further the development of this technology, a number of collaborations are being sought. One of the major aspects is the development of the control system and pulse sequence that is not based on Labview, which we currently use. As such, we have collaborated with pure devices GmbH (www.pure-devices.com) in Germany to develop a control system based on MATLab. This program will be easily adaptable in Uganda since MUST already runs a MATLab license. This control system will be tested at Penn State using our current system and there after shipped to Uganda after the rest of the system has been assembled.

Plans are under way to have the coils wound and the accompanying electronic components constructed. Students of Biomedical engineering at MUST will be involved in different aspects of this project. Collaborations are also being sought between MUST, Penn State, University of Delf in the Netherlands, Boston Children's hospital and Cure children's hospital in Uganda to move these project forward.

Among some of the aspects to be tackled in order to move the ultra-low field PMRI technology towards clinical applications are increasing the strength of the Bm and Bp magnetic fields, construction of optimized adult head sized transmitter and receiver coils with help from world renown experts such as Andrew Web from Leidel in the Netherlands, and improvements in the control system as already mentioned above. Super resolution software algorithms will also be used to post-process the images.

6.3 Increasing B_p and B_m magnetic field strengths

The current system operates at frequencies between 100 kHz and 250 kHz. A new system will be built to operate at frequency of up to 1 MHz. The SNR for PMRI system is directly proportional to the product of the Bm and Bp field and can be written as [39]

$$SNR \approx \frac{B_m B_p}{\sqrt{C_1 B_m^{\frac{1}{2}} + C_2 B_m^2}} \tag{6.1}$$

where C_1 and C_2 are constants for the coil noise and sample noise respectively. Given the relation between Bm and Lamor frequency as in equation 1.2, at high frequencies, sample noise $C_2 B_m^2$ dominates coil noise $C_1 B_m^{\frac{1}{2}}$ and SNR becomes proportional and dependent on only Bp. It has been shown that the system adopts this behavior at frequencies greater than 1 MHz [39], that is why the second system to be built will operate at frequency of at least 1 MHz.

Power considerations may limit the Bp field to not more than 200 mT. From our calculations, a 200 mT coil with a bore size of 30 cm using copper wire of gage 10 AWG would weigh about 130 kg, have a resistance of 10 Ohms with power requirement of 2250 Watts at 15 A. This can be achievable and will require air cooling. Fans will be mounted onto the system to blow air through it in order to ensure safe imaging. Water cooling is also being considered in case air cooling is insufficient.

6.4 Radio frequency shielding

MRI systems are very sensitive to electromagnetic interference. We have briefly explored the possibility of shielding low field MRI system using aluminum and brass as described in chapter five. We will however explore the use of aluminum for shielding the whole room where the system will be stationed. Aluminum is ubiquitous in Uganda and this option should be inexpensive. One other inexpensive material that will be explored for shielding is steel.One of the major deterrent in using steel for shielding PMRI systems is because of the pulsating Bp magnetic field. Being a ferromagnetic material, steel retains magnetization long enough that it may become a source of magnetic field inhomogeneity.

However, steel is a good shielding material for low field MRI systems without Bp and it also has the added advantage of boosting the magnetic field within the volume of interest [54]. In the COMSOL simulation in figure 6.1 below, we show that the magnetic field can be boosted by using a steel shield. In this simulation, the magnetic field is generated by the Lee-Whiting four coil system with diameter of 45 cm, 598 total number of turns. The current passing through the coils was 1 A. We see that the magnetic field can be boosted by as much as 25% by the introduction of a steel shield around the the coils. The shield was designed with a diameter of 47 cm and thickness of 1 cm.

We also demonstrate that by enclosing one end of the cylinder by iron shield, a standing gradient can be generated along the z-axis. This could act as the z-gradient. Using the same parameters used in boosting the field, a gradient of 5 mT/m could be achieved by injecting a current of 5 A into the coils (Figure 6.2).

Exploring this method of shielding could have the benefit of reducing power requirement for low field MRI systems and therefore reducing level of cooling re-

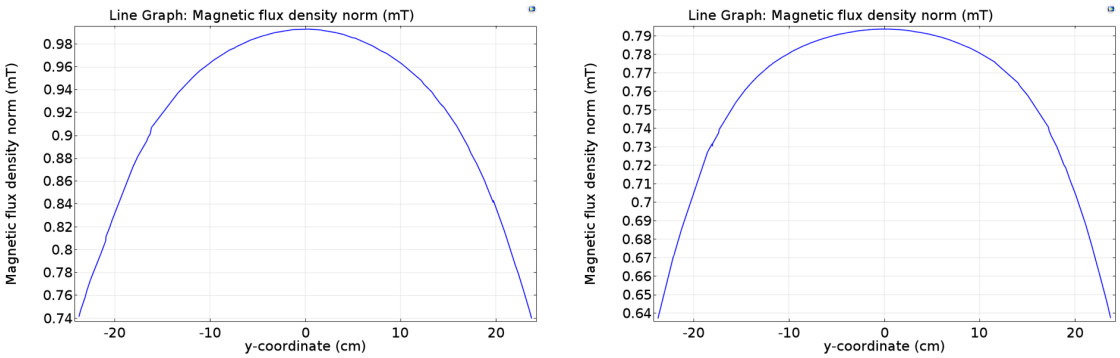


Figure 6.1. The graph on the left shows the magnetic field along the y-axis of a cylinder when the system is shielded using structural steel. On the right is the same magnetic field without the shield

.

quired.

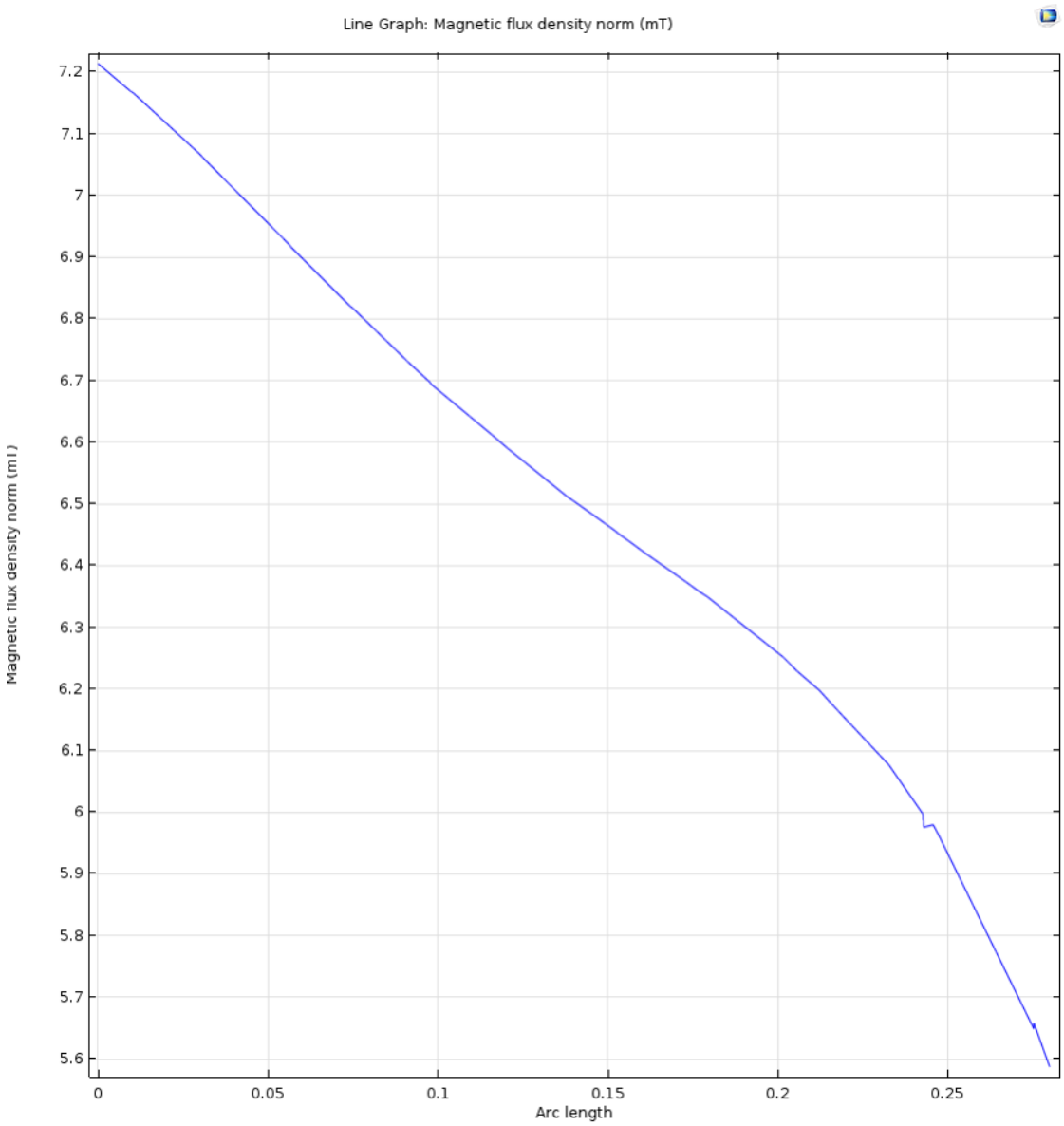


Figure 6.2. A standing gradient a long the z-axis created using structural steel shield

.

6.5 Clinical trial phase

After the system has been constructed, tested and approved, we will go into the clinical trial phase of the project and this will be at Cure Children's hospital in Mbale, Uganda. Cure Hospital specializes in the treatment of hydrocephalus and

Dr Steven J Schiff, who is the advisor in this project already leading a study to investigate the causes of hydrocephalus at this site.

Appendix A

The biomedical engineering curriculum for MUST

A.1 Introduction and Justification

This section us lifted from our curriculum document.

"Statistics about medical equipment usage and maintenance in developing countries is scanty but some estimates indicate that up to 70% of laboratory and other medical related equipment in developing countries are defective [4]. The proportion of this unusable equipment is even higher in countries where biomedical engineering has not been fully integrated into the health sector. There is a major problem of inadequate maintenance capability; lack of appropriate human resource to design, develop, and manage medical equipment in less developed countries. Such scenarios make it impossible to run an effective maintenance services even if other deficiencies were removed. The initiative to develop a curriculum for biomedical engineering is therefore a realistic intervention to provide a lasting solution to these problems experienced in less developed countries, Uganda

inclusive.

Many developing countries are dependent on donor assistance to meet the equipment needs of their health care systems. The donations sometimes do not meet their intended objectives; in most cases the technologies are obsolete and therefore the spare parts are not readily available. In addition, due to inadequate maintenance routines, the donated equipment frequently break down and foreign experts are often sourced at high costs to offer maintenance and simple repair services. Therefore, creation and development of human resource through training will provide the best option to alleviate these problems.

Between 2000 and 2002, the Uganda Health Sector Support Program, Phase I funded by DANIDA targeted the creation of medical equipment maintenance system by establishing regional equipment workshops well positioned to attend to maintenance and repair of medical equipment throughout Uganda [97]. According to [97], the support was not sustainable unless a more dependable method of funding (especially training of technical personnel) the regional equipment workshops is identified. This scenario has clearly underpinned the importance of first addressing the issue of developing appropriate human resource as the regional workshops that were initially created under the program are currently non-operational.

In addition, The Health Sector Strategic Plan (HSSP) III also lays out national plans of training biomedical engineering professionals [98]. However, this initiative can only be operationalized if higher institutions of learning establish training programs in this field. Furthermore, Biomedical Engineering being a fast growing field, has made most medical services become progressively more technology-based. Therefore, the creation of this program at Mbarara University of Science and Technology will offer a rare training opportunity for Uganda to develop the human resources required to meet the ever increasing demand for technology-based services.

Besides, the program will provide a rear opportunity for innovators to design, build, and possibly achieve commercial production of new products in terms of biomedical equipment. A cursory consideration of the current application of biomedical engineering and technologies in the Ugandas health sector show a gloomy picture. A performance survey of 69 major biomedical equipment at Mbarara Regional Referral Hospital was carried out to assess the proportion of functional medical equipment in the hospital. Out of the 69 equipment tested, 37.7% were operational but at reduced efficiencies. Some typical examples include: The oxygen concentrators, which are meant to give an output of between 94% - 100% pure oxygen were found to give oxygen outputs of below 60%. The ventilators located in the intensive care unit (ICU) were found to be using a 40 kg oxygen cylinder in less than three hours yet an efficient ventilator can continuously use a 40 kg oxygen cylinder for up to 24 hours. These situations arise due to lack of the relevant personnel to ensure routine maintenance and servicing of the equipment to maintain the desired performance.

The equipment operation and maintenance can be effectively achieved by referring to the user and service manuals. During this survey, only 3 user manuals were available, representing 4.3%. This implies that most of the equipment are either received without user manuals or due to lack of clear equipment management system in MRRH and the lack relevant personnel, the manuals probably get displaced or are completely lost. This presents an intricate problem in case of equipment failure or malfunction ".

A.2 Course content

The biomedical engineering curriculum details a four year bachelors program offered at MUST. The acronyms mean:

CU = Credit Unites

LH = Lecture Hours

PH = Practical Hours

CH = Contact Hours

First year Semester 1

Code	Name	CU	LH	PH	CH
BME 1101	Engineering Mathematics I	4	45	-	45
BME 1102	Basic Electrical & Electronics Engineering	4	40	20	45
BCE 1104	Introduction to Computing	3	30	20	35
BME 1103	Applied Chemistry	3	30	20	35
BME 1104	Applied Physics I	3	30	20	35
COM 1101	Communication Skills	3	30	-	30
DVS 1101	Development Studies	3	30	-	30
BME 1105	Workshop Practice 1	5	20	100	20
TOTALS		**28**			

First year Semester 2

Code	Name	CU	LH	PH	CH
BME 1201	Engineering Mathematics II	4	45	-	45
BME 1202	Engineering Drawing	4	30	30	45
CSC 1205	Introduction to Computer Programming – C	3	30	-	30
BME 1203	Biochemistry	3	30	20	35
BME 1204	Applied Physics II	3	30	20	35
BBA 1209	Entrepreneur Development & Business Ethics	3	30	-	30
BME 1205	Engineering Mechanics	4	45	-	45
BME 1206	Workshop Practice II/Recess	5	20	100	20
Total		**29**			

Figure A.1. Course content for Year 1

Second year Semester 1

Code	Name	CU	LH	PH	CH
BME 2101	Electronic Circuits	4	45	20	45
BME 2102	Electrical Network Analysis & Synthesis	4	30	30	60
BME 2103	Engineering Mathematics III	4	40	-	40
BME 2104	Human Anatomy & Physiology	4	40	20	60
BME 2105	Biomaterials	4	40	20	60
BME 2106	Database management systems	3	40	20	60
Total		**23**			

Second year Semester 2

Code	Name	CU	LH	PH	CH
BME 2201	Engineering Mathematics IV	3	30	-	30
BME 2202	Circuit Analysis & Design	4	45	20	45
BME 2203	Transducers in Biomedical Instrumentation	4	45	30	60
BME 2204	Electronic Instruments	4	45	30	45
BME 2205	Biomechanics, Prosthetic & Orthotics	4	45	30	45
BME 2206	Logic Circuits	3	30	20	60
BME 2301	Industrial Training	5	20	100	50
Total		**27**			

Figure A.2. Course content for Year 2

Third year Semester 1

Code	Name	CU	LH	PH	CH
BME 3101	Microprocessors	4	30	30	45
BME 3102	Analogue and Digital Communication	4	45	-	45
BME 3103	Biomedical Instrumentation I	4	30	30	30
BME 3104	Design of Analogue Circuits	4	30	30	45
BME 3105	Signals and Systems	3	30	-	30
BME 3106	Computer-aided design	4	30	20	30
Electives					
CSC 3101	Software Engineering	3	30	20	45
BIT 3105	Mobile Networks & Computing	3	30	20	45
Total		**29**			

Third year Semester 2

Code	Name	CU	LH	PH	CH
BME 3201	Embedded Systems Design	3	30	-	30
BME 3202	Medical Imaging I	4	40	20	40
BME 3203	Biomedical Instrumentation II	4	30	20	45
BME 3204	Biostatistics	3	30	-	30
BME 3205	Digital Signal Processing for Biomedical Applications	3	30	-	30
BME 3207	Group Project	4	15	40	30
BME 3301	Industrial Training	5			
Electives					
BME 3204	Biological Modeling and Simulations	3	30	30	30
BIT 3207	Database Programming	3	30	20	45
Total		**32**			

Figure A.3. Course content for Year 3

Fourth year Semester 1

Code	**Name**	**CU**	**LH**	**PH**	**CH**
BME 4101	Medical Imaging II	4	45	20	50
EEE 4102	Research Methods	3	30	-	30
BME 4103	Biomedical Instrumentation III	4	45	20	50
BME 4301	Final year project	5	15	60	30
Electives					
BME 4104	Basics of Very Large Scale Integration (VLSI)	3	45	-	45
BME 4105	Networking and Information Systems in Medicine	4	45	20	50
BME 4106	Biomedical Signal and Image Processing	3	45	20	45
Total		**26**			

Fourth year Semester 2

Code	Name	CU	LH	PH	CH
BME 4201	Nuclear Medicine	4	45	-	45
BME 4202	Hospital Management	4	45	-	45
BME 4203	Installation, Maintenance and Servicing	4	45	20	50
BME 4301	Final Year Project	5	15	60	30
Electives					
BME 4204	Biomedical Microsystems				
BME 4205	Robotics in Medicine	3	45	20	50
BME 4206	Infection Control	3	45	20	50
Total		**23**			

Figure A.4. Course content for Year 4

Bibliography

[1] Brenner, D. J. and E. J. Hall (2007) "Computed tomography–an increasing source of radiation exposure." *The New England journal of medicine*, **357**(22), pp. 2277–2284.

[2] Klein, H.-M. (2016) "Clinical Low Field Strength Magnetic Resonance Imaging," pp. 133–141.

[3] energy Outlook, W. (2017), "Focus on Africa," .
URL http://www.worldenergyoutlook.org/resources/energydevelopment/africafocus/

[4] International, A. (2016), "Biomedical Engineering Technician Training," .
URL http://www.assistinternational.org/biomedical-engineering-technician-training/

[5] Global Health Institute, D. (2014), "New BMET Training Project to Begin in Nigeria," .
URL https://globalhealth.duke.edu/media/news/new-bmet-training-project-begin-nigeria

[6] Nkuma-Udah, K. I. and E. A. Mazi (2006) "Developing Biomedical Engineering in Africa: A case for Nigeria," *IFMBE Proceedings*, **14**, pp. 3828–3831.

[7] Seggie, J. L. (2010) "for Africa," *Africa*, **2**(1), pp. 8–14.

[8] AFSB, "Africa Is Becoming A Hub Of Medical Innovation," .
URL http://www.africastrictlybusiness.com/news-analysis/africa-becoming-hub-medical-innovation

[9] Roguin, A. (2004) "Nikola Tesla: the man behind the magnetic field unit." *Journal of magnetic resonance imaging : JMRI*, **19**(3), pp. 369–74.
URL http://www.ncbi.nlm.nih.gov/pubmed/14994307

[10] Gerlach, W. and O. Stern (1922) "Der experimentelle Nachweis der Richtungsquantelung im Magnetfeld," *Zeitschrift f??r Physik*, **9**(1), pp. 349–352.

[11] Warwick, A. (1991) "On the role of the FitzGerald-Lorentz contraction hypothesis in the development of Joseph Larmor's electronic theory of matter," *Archive for history of exact sciences*, **43**(1), pp. 29–91.

[12] Haacke, E. M., R. W. Brown, M. R. Thompson, and R. Venkatesan (1999) *Magnetic Resonance Imaging: Physical Principles and Sequence Design*, vol. 1st.
URL http://books.google.com/books?id=BnOvQgAACAAJ{&}pgis=1

[13] Bloch, F., W. W. Hansen, and M. Packard (1946) "The nuclear induction experiment," *Physical Review*, **70**(7-8), pp. 474–485, arXiv:1011.1669v3.

[14] Purcell, E., H. Torrey, and R. Pound (1946) "Resonance Absorption by Nuclear Magnetic Moments in a Solid," *Physical Review*, **69**(1-2), pp. 37–38.
URL http://journals.aps.org/pr/abstract/10.1103/PhysRev.69.37{%}5Cnhttp://link.aps.org/doi/10.1103/PhysRev.69.37

[15] T, A. J., D. S.S, and P. M. E. (1951) "Chemical Effects on Nuclear Induction Signals from Organic Compounds," *Journal of Chemical Physics*, **19**(4), p. 507.

[16] Damadian, R. (1969), "Document 30," .
URL http://www.fonar.com/pdf/doc{_}30.pdf

[17] Lauterbur, P. C. (1973) "Image Formation by Induced Local Interactions: Examples Employing Nuclear Magnetic Resonance," *Nature*, **242**(5394), pp. 190–191.
URL http://www.nature.com/physics/looking-back/lauterbur/index.html

[18] Mansfield, P. and A. A. Maudsley (1977) "Medical imaging by NMR," *British Journal of Radiology*, **50**(591), pp. 188–194.

[19] Hinshaw, W. S., P. A. Bottomley, and G. N. Holland (1977) "Radiographic thin-section image of the human wrist by nuclear magnetic resonance," *Nature*, **270**(5639), pp. 722–723.
URL http://adsabs.harvard.edu/abs/1977Natur.270..722H

[20] Damadian, R., M. Goldsmith, and L. Minkoff (1977) "FONAR images of the live human body," *Physiological Chemistry and Physics*, **9**, pp. 97–100.

[21] Klein, H.-M. (2016) *Clinical Low Field Strength Magnetic Resonance Imaging: A Practical Guide to Accessible MRI*, Springer, New York.

[22] Kaufman, L., M. Arakawa, J. Hale, P. Rothschild, J. Carlson, K. Hake, D. Kramer, W. Lu, and H. J. Van (1989) "Accessible magnetic resonance imaging." *Magnetic Resonance Q*, **5**(4), pp. 283–297.

[23] Mashberg, T. (2005) "CT Scan to Go," *MIT Technology Review*.
URL http://www.technologyreview.com/article/404976/ct-scan-to-go/

[24] Park, A. (2012) "Too {Many} {Scans}? {Use} of {CT} {Scans} {Triples}, {Study} {Finds}," *Time*.
URL http://healthland.time.com/2012/06/13/too-many-scans-use-of-ct-scans-triples-study-finds/

[25] Rekate, H. L. (2008) "The definition and classification of hydrocephalus: a personal recommendation to stimulate debate." *Cerebrospinal fluid research*, **5**, p. 2.
URL http://www.ncbi.nlm.nih.gov/pubmed/18211712{%}5Cnhttp://www.pubmedcentral.nih.gov/articlerender.fcgi?artid=PMC2263019

[26] Li, L., A. Padhi, S. L. Ranjeva, S. C. Donaldson, B. C. Warf, J. Mugamba, D. Johnson, Z. Opio, B. Jayarao, V. Kapur, M. Poss, and S. J. Schiff (2011) "Association of bacteria with hydrocephalus in Ugandan infants." *Journal of neurosurgery. Pediatrics*, **7**(1), pp. 73–87.

[27] Warf, B. C., B. C. Alkire, S. Bhai, C. Hughes, S. J. Schiff, J. R. Vincent, and J. G. Meara (2011) "Costs and benefits of neurosurgical intervention for infant hydrocephalus in sub-Saharan Africa." *Journal of neurosurgery. Pediatrics*, **8**(5), pp. 509–21.

[28] Warf, B. C., A. R. Dagi, B. N. Kaaya, and S. J. Schiff (2011) "Five-year survival and outcome of treatment for postinfectious hydrocephalus in Ugandan infants," *Journal of Neurosurgery: Pediatrics*, **8**(November), pp. 502–508.

[29] Oersted, H. C. (1820) "Experiments on the Effect of a Current of Electricity on the Magnetic Needle," *Annals of Philosophy*, (16), pp. 273–277.

[30] Steinle, F. (2002) "Experiments in history and philosophy of science," *Perspectives on Science*, **10**(4), pp. 408–432.

[31] Hanson, L. G. (2008) "Is quantum mechanics necessary for understanding magnetic resonance?" *Concepts in Magnetic Resonance Part A*, **32**(5), pp. 329–340.

[32] Hashemi, R. H., W. G. Bradley, and C. J. Lisanti (2012) *MRI: the basics*, Lippincott Williams & Wilkins.

[33] Moyer, B. (2016), "An Overview Of Medical Imaging Electronics," . URL http://www.mouser.com/applications/medical-imaging-overview/

[34] Elmaoglu, M. and A. Celik (2011) *MRI Handbook: MR Physics, Patient Positioning, and Protocols*, vol. 17, arXiv:1011.1669v3. URL https://books.google.com/books?id=P4G6Ru{_}A9xUC{&}pgis=1

[35] Wilkinson, I. D. and M. J. Graves (1016), "Magnetic resonance imaging," . URL http://radiologykey.com/magnetic-resonance-imaging-6/

[36] Prince, J. L. and J. M. Links (2006) *Medical imaging signals and systems*, Pearson Prentice Hall Upper Saddle River, NJ.

[37] Golay, M. J. E. (1958) "Field homogenizing coils for nuclear spin resonance instrumentation," *Review of Scientific Instruments*, **29**(4), pp. 313–315.

[38] Hornak, J. P. (1996), "The basics of MRI," .

[39] Matter, N. I., G. C. Scott, T. Grafendorfer, A. Macovski, and S. M. Conolly (2006) "Rapid polarizing field cycling in magnetic resonance imaging," *IEEE transactions on medical imaging*, **25**(1), pp. 84–93.

[40] Macovski, A. and S. Conolly (1993) "Novel approaches to lowcost MRI," *Magnetic resonance in medicine*, **30**(2), pp. 221–230.

[41] Morgan, P., S. Conolly, G. Scott, and A. Macovski (1996) "A readout magnet for prepolarized MRI," *Magnetic resonance in medicine*, **36**(4), pp. 527–536.

[42] Scott, G., B. Chronik, N. Matter, H. Xu, P. Morgan, L. Wong, A. Macovski, and S. Conolly (2001) "A prepolarized MRI scanner," *Proc. Int. Soc. Magn. Reson. Med.(Glasgow, Scotland)*, **9**.

[43] Matter, N. I., G. C. Scott, R. D. Venook, S. E. Ungersma, T. Grafendorfer, A. Macovski, and S. M. Conolly (2006) "Threedimensional prepolarized magnetic resonance imaging using rapid acquisition with relaxation enhancement," *Magnetic resonance in medicine*, **56**(5), pp. 1085–1095.

[44] Los Alamos National Laboratory (2015), "Portable MRI could aid wounded soldiers and children in the Third World," .
URL http://www.lanl.gov/discover/news-release-archive/2015/April/04.22-portable-mri.php

[45] Zotev, V. S., A. N. Matlashov, P. L. Volegov, I. M. Savukov, M. A. Espy, J. C. Mosher, J. J. Gomez, and R. H. Kraus (2008) "Microtesla MRI of the human brain combined with MEG," *Journal of Magnetic Resonance*, **194**(1), pp. 115–120.

[46] Savukov, I. M., V. S. Zotev, P. L. Volegov, M. A. Espy, A. N. Matlashov, J. J. Gomez, and R. H. Kraus (2009) "MRI with an atomic magnetometer suitable for practical imaging applications," *Journal of Magnetic Resonance*, **199**(2), pp. 188–191.

[47] Shah, V. K. and R. T. Wakai (2013) "A compact, high performance atomic magnetometer for biomedical applications," *Physics in medicine and biology*, **58**(22), p. 8153.

[48] Xia, H., A. B.-A. Baranga, D. Hoffman, and M. V. Romalis (2006) "Magnetoencephalography with an atomic magnetometer," *Applied Physics Letters*, **89**(21), p. 211104.

[49] Savukov, I. M. and M. V. Romalis (2005) "NMR detection with an atomic magnetometer," *Physical review letters*, **94**(12), p. 123001.

[50] Liu, G., X. Li, X. Sun, J. Feng, C. Ye, and X. Zhou (2013) "Ultralow field NMR spectrometer with an atomic magnetometer near room temperature," *Journal of Magnetic Resonance*, **237**, pp. 158–163.

[51] Li, Y., J. Kim, M. Kim, A. Armutlulu, and M. G. Allen "RETAINING HIGH AREAL IN-PLANE MAGNETIC ENERGY DENSITY OVER LARGE MAGNETIC THICKNESS: A PERMANENT MAGNETIC MICROLAMINATION APPROACH BASED ON SEQUENTIAL MULTILAYER ELECTROPLATING," *University of Pennsylvania, Philadelphia, PA, Georgia Institute of Technology, Atlanta, GA*.

[52] Herrera-May, A. L., J. A. Tapia, S. M. Domínguez-Nicolás, R. Juarez-Aguirre, E. A. Gutierrez-D, A. Flores, E. Figueras, and E. Manjarrez (2014) "Improved detection of magnetic signals by a MEMS sensor using stochastic resonance," *PloS one*, **9**(10), p. e109534.

[53] Damadian, R., M. Goldsmith, and L. Minkoff (1977), "NMR in cancer: XVI. FONAR image of the live human body," arXiv:1011.1669v3.
URL http://buffalo.summon.serialssolutions.com/2.0.0/link/0/eLvHCXMw3V3LSsNAFB2kKHYj2lZ8wqzcSErSyWMiuCjVWqGtUqvoqkzmIYUmKdou-vfOI4-24g-4n

[54] Lother, S., S. J. Schiff, T. Neuberger, P. M. Jakob, and F. Fidler (2016) "Design of a mobile, homogeneous, and efficient electromagnet with a large field of view for neonatal low-field MRI," *Magnetic Resonance Materials in Physics, Biology and Medicine*, pp. 1–8.

[55] Sarracanie, M., C. D. LaPierre, N. Salameh, D. E. J. Waddington, T. Witzel, and M. S. Rosen (2015) "Low-cost high-performance MRI," *Scientific reports*, **5**.

[56] Savukov, I., T. Karaulanov, C. J. V. Wurden, and L. Schultz (2013) "Non-cryogenic ultra-low field MRI of wrist-forearm area," *Journal of Magnetic Resonance*, **233**, pp. 103–106.

[57] Shvartsman, V. A., "High-Power Solid-State Device, p/n EDR84102/x," . URL http://vsholding.com/products/solid-state-relays-switches-12-drivers-and shtml

[58] Hayt, W. (1989) *Engineering electromagnetics*, 5th ed., McGraw-Hill.

[59] Texas Instruments (2011), "Application Note 779 A Basic Introduction to Filters - Active, Passive,and Switched Capacitor," . URL http://www.ti.com/lit/an/snoa224a/snoa224a.pdf

[60] Lexurion, "The history of amateur radio," . URL http://www.astrosurf.com/luxorion/qsl-ham-history-landmarks.htm

[61] Gary Breed (2011), "The Mathematics of Mixers: Basic Principles," . URL http://www.highfrequencyelectronics.com/Jan11/HFE0111{_}Tutorial.pdf

[62] Smith, S. W. (2000) *Digital signal processing*, vol. 17, IEEE, 97-80293. URL http://ieeexplore.ieee.org/lpdocs/epic03/wrapper.htm?arnumber=826412

[63] Organization, W. H. (2016), "Head circumference-for-age GIRLS," . URL http://www.who.int/childgrowth/standards/second{_}set/cht{_}hcfa{_}girls{_}z{_}0{_}5.pdf?ua=1

[64] Bushby, K. M., T. Cole, J. N. Matthews, and J. A. Goodship (1992) "Centiles for adult head circumference," *Archives of Disease in Childhood*, **67**(10), pp. 1286–1287.

[65] Erdogmus, D., E. G. Larsson, R. Yan, J. C. Principe, and J. R. Fitzsimmons (2004) "Measuring the signal-to-noise ratio in magnetic resonance imaging: A caveat," *Signal Processing*, **84**(6), pp. 1035–1040.

[66] Mutia, D., J. Kihiu, and S. Maranga (2012) "Maintenance Management of Medical Equipment in Hospitals," *Industrial Engineering Letters*, **2**(3), pp. 9–19.
URL http://ir.jkuat.ac.ke:8080/bitstream/handle/123456789/706/MaintenanceManagementofMedicalEquipmentinHospitals.pdf?sequence=1{&}isAllowed=y

[67] Mettler, F. A., W. Huda, T. T. Yoshizumi, and M. Mahesh (2008) "Effective doses in radiology and diagnostic nuclear medicine: a catalog," *Radiology*, **248**(1), pp. 254–263.
URL https://com-radiology-cardiac-imaging.sites.medinfo.ufl.edu/files/2013/07/Effective-dose-in-Rad-and-NM.pdf

[68] Merritt, R., C. Purcell, and G. Stroink (1983) "Uniform magnetic field produced by three, four, and five square coils," *Review of Scientific Instruments*, **54**(7), pp. 879–882.

[69] Rubens, Sidney, M. (1945) "Cube-Surface Coil for Producing a Uniform Magnetic Field," *Review of Scientific Instruments*, **16**(9), pp. 243–245.

[70] Lee-Whiting, G. (1957) *Uniform magnetic fields*, *Tech. rep.*, Atomic energy of Canada, Ltd.

[71] Gottardi, G., P. Mesirca, C. Agostini, D. Remondin, and F. Bersani (2003) "A Four Coil Exposure System (Tetracoil) Producing a Highly Uniform Magnetic Field," *Bioelectromagnetics*, **24**(2), pp. 125–133.

[72] Gary, H. (2014), "Harnessing Africa's untapped solar energy potential for health," .
URL http://www.who.int/bulletin/volumes/92/2/14-020214.pdf

[73] wire industries MWS, "World ' s Largest Selection of Specialty Magnet Wire," .
URL http://www.mwswire.com/pdf{_}files/mws{_}tech{_}book/techbook2016.pdf

[74] Samila, A. (2015) "Simulation of Magnetic Field Topology in a Saddle-Shaped Coil of Nuclear Quadrupole Resonance Spectrometer," *Progress In Electromagnetics Research Letters*, **56**, pp. 67–73.

[75] Ginsberg, D. M. and M. J. Melchner (1970) "Optimum geometry of saddle shaped coils for generating a uniform magnetic field," *Review of Scientific Instruments*, **41**(1), pp. 122–123.

[76] Hidalgo, T. S. (2010) "Theory of Gradient CoilDesign Methods forMagnetic ResonanceImaging," *Concepts in Magnetic Resonance Part A*, **Vol. 36A**(4), pp. 223–242.

[77] Rashid, S. A., B. S. Amiruddin, and T. H. Chew (2008) "Magnetic field simulation of Golay coil," *Journal of Fundamental Sciences*, pp. 353–361.
URL www.ibnusina.utm.my/jfs

[78] Hanssum, H. (1985) "The magnetic field of saddle-shaped coils. II. Transverse components," *J. Phys. D: Appl. Phys.*, **18**, pp. 1971–1978.

[79] Cory, D. and C. Manos (2006), "Frequency response: Resonance, Bandwidth, Q factor," .
URL https://ocw.mit.edu/courses/electrical-engineering-and-computer-science/6-071j-introduction-to-electronics-signals-and-measurement-spring-2006/lecture-notes/resonance{_}qfactr.pdf

[80] Truong, T. K., D. W. Chakeres, D. Q. Beversdorf, D. W. Scharre, and P. Schmalbrock (2006) "Effects of static and radiofrequency magnetic field inhomogeneity in ultra-high field magnetic resonance imaging," *Magnetic Resonance Imaging*, **24**(2), pp. 103–112.

[81] Wang, J., S. She, and S. Zhang (2002) "An improved Helmholtz coil and analysis of its magnetic field homogeneity," *Review of Scientific Instruments*, **73**(5), p. 2175.

[82] Frollo, I., P. Andris, and S. I (2001) "MEASURING METHOD AND MAGNETIC FIELD HOMOGENEITY OPTIMISATION FOR MAGNETS USED IN NMR-IMAGING," *MEASUREMENT SCIENCE REVIEW*, **1**(1), pp. 9–12.
URL http://www.measurement.sk/PAPERS/Frollo5.pdf

[83] Restrepo, F. A., E. Franco, H. Cadavid, and P. R. Carlos (2016) "Analysis of the Magnetic Field Homogeneity for an Equilateral Triangular Helmholtz Coil," *Progress In Electromagnetics Research*, **50**, pp. 75–83.

[84] Laske Shore Cryogenics, I. (2014), "Lake Shore Model 475 Gaussmeter User's Manual," .
URL http://www.lakeshore.com/Documents/475{_}Manual.pdf

[85] Kedzia, P., T. Czechowski, M. Baranowski, J. Jurga, and E. Szcześniak (2013) "Analysis of Uniformity of Magnetic Field Generated by the Two-Pair Coil System," *Applied Magnetic Resonance*, **44**(5), pp. 605–618.

[86] Ocegueda, K. and A. O. Rodríguez (2006) "A simple method to calculate the signal-to-noise ratio of a circular-shaped coil for MRI," *Concepts in Magnetic Resonance Part A: Bridging Education and Research*, **28**(6), pp. 422–429.

[87] International Electrochemical Commission (2008), "Medical electrical equipment: part 2-33. Particular requirements for the safety of magnetic resonance equipment for medical diagnosis," .

[88] Collins, C. M. and Z. Wang (2011) "Calculation of radiofrequency electromagnetic fields and their effects in MRI of human subjects," *Magnetic resonance in medicine : official journal of the Society of Magnetic Resonance in Medicine / Society of Magnetic Resonance in Medicine*, **65**(5), pp. 1470–1482.
URL http://www.ncbi.nlm.nih.gov/pubmed/21381106

[89] Hebrank, X. F. (2009), "More on SAR A practical Guidance for MRI users," .
URL http://cds.ismrm.org/protected/09MProceedings/files/TuesA18{_}03Hebrank.pdf

[90] Montgomery, B. D. (1980) *Solenoid Magnet Design*, Robert E. Krieger Publishing Company, Malabar, FL.

[91] Tobias Gilk, M. (2007), "MRI Suite Construction Costs: The Million-Dollar Question." .
URL http://rad-planning.com/RADblog/2012/02/09/mri-suite-construction-costs-the-million-dollar-question/

[92] Glisson, a. and R. Scharstein (2001), "Introduction to electrodynamics, 3rd edition [Book Review]," .
URL http://ieeexplore.ieee.org/lpdocs/epic03/wrapper.htm?arnumber=920021

[93] Joseph, W. (1993), "Properties of materials used for RF shielding," .
URL http://www.ets-lindgren.com/pdf/emctd{_}1293{_}weibler.pdf.

[94] Henry, O. W. (2009) *Electromagnetic Compatibility Engineering.*, John Wiley & Sons, New York.

[95] DEPARTMENT OF DEFENSE and W. D. 20301 (1987) *MILITARY HANDBOOK: GROUNDING, BONDING, AND SHIELDING FOR ELECTRONIC EQUIPMENTS AND FACILITIES*, *Tech. rep.*, Department of Defence, Washington,DC.

[96] De Maria, C., D. Mazzei, and A. Ahluwalia (2015) "Improving African healthcare through open source biomedical engineering," *International Journal on Advances in Life Sciences*, **7**(1-2), pp. 10–19.

[97] Ministry of Helath, U. (2000) *Health Sector Strategic Plan 2000-2005:*, *Tech. rep.*, Ministry of Health, Uganda, Kampla.
URL http://siteresources.worldbank.org/INTPRS1/Resources/383606-1201883571938/Uganda{_}HSSP.pdf

[98] ——— (2010) *The Health Sector Strategic Plan III 2010-1015*, *Tech. rep.*, Ministry of Health, Uganda, Kampala.
URL http://www.health.go.ug/docs/HSSP{_}III{_}2010.pdf

Vita

Johnes Obungoloch

EDUCATION

The Pennsylvania State University, PhD Bioengineering 2013-2017

Keele University United Kingdom, MSc. Biomedical Engineering 2009/2010

Makerere University Uganda, BSc. Electrical Engineering 2001-2005

WORK EXPERIENCE

2010-todate: Lecturer, Mbarara University of Science and Technology (MUST)

2006-2013: Head, medical equipment repair and maintenance workshop, MUST

May 2017: I will take up faculty position as the program head for the department of Biomedical Engineering at MUST

OTHER EXPERIENCE AND PROFESSIONAL MEMBERSHIPS

2012-todate: Member, Uganda National Association of Medical and Hospital Engineers (UNAMHE)

2013-todate: Director, Uganda Biomedical Engineering Technologies (UBETech)

HONORS AND AWARDS

2014: Winner, DOW sustainability innovation student challenge award, Penn State University

August 2014: CAMTech Launch Award winner for development of medical suction pump, Consortium for affordable medical technology

RESEARCH

2014-2015: Development of electronically controlled medical suction device, Sponsored by The consortium for affordable medical technologies.

CONFERENCES ATTENDED

April 2, 2015: College of Engineering Research Symposium, Pennsylvania State University Oral Presentation: Development of ultra-low field magnetic resonance imaging for developing countries.

January 16th to 17th, 2017: Uganda Nationtional Biomedical Engineering Conference Oral presentation: Development of sustainable low-field magnetic resonance imaging for diagnosis of hydrocephalus in developing countries.

PAPERS UNDER PREPARATION Design of a sustainable pre-pulse magnetic resonance imaging system for infant hydrocephalus